Quantum Phases In Quasi-One Dimensional Frustrated Spin Systems

Thesis submitted for the degree of

Doctor of Philosophy (Science)

in

Physics (Theoretical)

by

Sk Saniur Rahaman

Department of Physics

University of Calcutta

2024

Dedicated to my family ...

Acknowledgements

I want to convey my gratitude towards my thesis supervisor Prof. Manoranjan Kumar for his patient guidance and advice throughout my Ph. D. tennure. The fruitful discussion with him was outstandingly rewarding. His intuitive ideas and excellent expertise in numerical algorithms have taught and motivated me a lot.

I would like to acknowledge Prof. M. Sanjay Kumar, who helped me a lot in solving many quantum mechanics problems. I acknowledge one of my collaborators Dr. Shaon Sahoo for his fruitful discussion in the initial days of my Ph.D. I am thankful to S.N.B.N.C.B.S. for allowing me to pursue my Ph.D. I would like to thank University Grants Commission (U.G.C) for the financial support during my Ph.D.

Because of being an individual introvert, I have always been less talkative to the teachers in my school and college days. But their special care, suggestions, and support have inspired and made me come to reach this stage of life. I would proudly want to take the name of the teacher who first believed in me and he is none other than my elder brother Sk Sattakur Rahaman. His intent towards study, critical thinking about science, and motivation about life still motivate me to aspire. My words and acknowledgment would always be less in justifying his contribution to my life. I would also like to thank Gautam Da (Physics), and Samsur Da (English) for their friendly teaching ways in my school days. I would like to thank Sujit Babu, Madhusudan Babu, Shyamaprasad Babu, and Koushik Babu for giving me the best college life experience through their visions and demonstrations of the problems of Physics.

I would like to thank my senior group members: Aslam Da, Sudipta Da, Daya Da, Sudip Da, Monalisa Di, Debasmita Di, colleagues: Koushik, Jyotirmoy, Chatterjee, and junior group members Manodip, Saurabh, Sayan, Anutosh for their valuable times. I can not skip other than thanking the group members of the 'Cockroach Gang': Ananda, Sourav, Sudipta da, and Koushik for their vibrant energies. I will miss Rafiqul, Nur, Osman, and Aziz during 'Ramadan'. I would like to thank

the members of 'foodies': Shubhadeep and Debayan for helping me explore some of the great places for food and beverages. The five years of hostel life inside the campus would have been not comfortable and enjoyable without many of the workers in S.N.B.N.C.B.S. I thank all the cleaners, gardeners, electrical section, security guards, and cooking staff of the mess and canteen who have always been like friends and provided me with a comfortable lifestyle.

Having less but good friends has always been a choice in my life. I am thankful to Asish, Subhajit, Sushil, Manoj, Suman, Diganta, Imraan, and Sandeep for giving their valuable company in my school life. I would also like to thank Debabrata, Mriganka, Srikrishna, and Sanchayeeta for supporting me throughout my college life. I also thank Shuvendu, Israful, and Hapijul for giving their precious time during the Masters course.

Last but the most, I would like to acknowledge my family for their selfless support to fulfill all my requirements and dreams. I thank you, Abba, Maa for parenting me. I always pray to Allah for your eternal lives. I always miss you Bardo Bubu. I still object to Allah why you have been taken from us so early. I owe you Mejo Bubu, Bithu Bubu, and Rinku Bubu for your special care and shelter. I thank you, Bardo Bhaiya, Mejo Bhaiya (Sattakur), and Tinku Bhaiya for always being so protective of me. I am delighted to have so loveable nephews and nieces like Riju, Sahil, Nafisa, Harish, Maanha, Aanas, Rishaan, Saiyyan, Mannat, and Mehreen. I am thankful to Alamgir, Mamun, and Sajjad for being my valuable relatives cum friends. Alamgir's intelligence skill has always been a friendly, competitive reference for me during my school days.

List of publications

Included in the thesis

1. Machine learning approach to study quantum phase transitions of a frustrated one-dimensional spin-1/2 system, Sk Saniur Rahaman, Sumit Haldar, and Manoranjan Kumar, **J. Phys.: Condens. Matter 35 115603 (2023)**

2. Quantum phase transitions in the XXZ model using Principal Component Analysis, Sk Saniur Rahaman, Manoranjan Kumar (Manuscript under preparation)

3. Quantum phases and thermodynamics of a frustrated spin-1/2 ladder with alternate Ising–Heisenberg rung interactions, Sk Saniur Rahaman, Shaon Sahoo, and Manoranjan Kumar, **J. Phys.: Condens. Matter 33 265801 (2021)**

4. Magnetic plateaus and jumps in spin-1/2 ladder with alternate Ising-Heisenberg rungs: a field dependent study, Sk Saniur Rahaman, Manoranjan Kumar, and Shaon Sahoo, **arXiv:2304.12266 (2023)**

5. Symmetry broken phases and quantum spin liquids in a 2-layer ladder-like pyrochlore lattice, Sk Saniur Rahaman, Sayan Ghosh, Manoranjan Kumar (Manuscript under preparation)

Other works

1. Study of the Berezinskii-Kosterlitz-Thouless transition: An unsupervised machine learning approach, Sumit Haldar, Sk Saniur Rahaman, Manoranjan Kumar, **arXiv:2205.15151 (2023)**

Contents

List of Figures

List of Tables

Chapter 1

Introduction

The study of frustrated magnets is one of the most interesting topics in condensed matter physics because of their diverse magnetic properties and their immense application to smart devices in everyday life, such as magnetic storage, memory, switches, smart watches, magnetic resonance imaging (MRI), etc [2]. For the last few decades, the search and synthesis of such magnetic materials have been a frontier in the field of spin systems and magnetic materials. To design more efficient magnetic devices with even more diverse properties, the first and foremost task is to gain more knowledge about the microscopic quantum nature of spin systems. Nevertheless, it is difficult to understand a complicated quantum many-body spin system, but it has also at the same time proved to be an interesting challenge to explore some of its properties, behaviors, and phases. Before going into some specific areas of my research work, let us briefly discuss quantum magnets, spin systems, and their various properties.

1.1 Quantum Magnets

When introducing the magnets, one cannot help but mention the large magnet "Earth", which consists of tons of molten iron [3]. It is known how the big magnet "Earth" protects the planet from cosmic rays and charged particles. The other

application is the navigation system which has been well known since the age of Nelson Alexander and Vasco da Gama to the recent applications in Google Maps, Apple Maps, etc [4]. One of the large magnets in the medical profession in our daily lives, MRI belongs to the category of high-energy magnets. On the other hand, there are many examples of the smallest magnets we know in everyday life, such as magnetic storage devices like compact discs (CD), hard disc drives (HDD), solid-state drives (SSD), memory chips, and smartwatches. Depending on the size and interaction of the atoms, magnets have different energy scales and applications. This is why MRI belongs to the category of high-energy scale magnets, whereas, smartwatches and memory chips are well known because of their efficiency and power consumption on the low-energy scale. However, all of these have different applications because of their different energy scale and properties which are contributed by each of the spins of an atom. The understanding of the intrinsic nature of the spin of an atom is really important which motivates the researchers to design, synthesize, and study some of the new types of spin systems. There are many examples but the current time replacement of HDD by the SSD as the storage device might be one good example to motivate the researchers[5]. These quantum magnets are diverse because of their different magnetism and various kinds of magnetic properties.

Magnetism is a phenomenon in a material that originates from the orbital and angular rotation of the itinerant and localized electrons of atoms. These rotations of the electrons give rise to orbital and spin magnetic moment which helps to interact with each other [6]. The spin alignment is conventionally decided by the axial direction of the spin rotation. The interactions of the electrons can be of various types and lead to exhibiting magnetic properties such as ferromagnetic, antiferromagnetic, paramagnetic, diamagnetic, etc. At an absolute zero temperature, this leads to spontaneous ordering in ferromagnetic and antiferromagnetic properties [7]. The relative spin alignment depends upon the nature of the spin exchange between any two spins. For the ferromagnetic systems, the spins are aligned parallel i.e., the angle between the spin $\theta = 0$, whereas, for the antiferromagnetic systems, the spins are aligned oppositely or $\theta = \pi$. The relative angle between the spins

can even have any other values than these in between $0 < \theta < \pi$. $CdCr_2Se_4$ [8], EuO [9], EuS[10], K_2CuF_4 [11], Rb_2CrCl_4 [12] are the examples of synthesized ferromagnetic materials. There are some examples of experimentally synthesized antiferromagnetic materials such as MnO [13], $RbMnFe_3$ [14], Rb_2MnCl_4 [15]. $EuSe$ [16] is an example of synthesized partially polarized ferrimagnetic material.

Apart from these, there are some other magnetic materials such as Fe, Ni, Co, and their alloys which simultaneously show transport properties like electrical conductivity as well. However, this thesis work more relates to the magnetic properties due to the many-body interactions of the localized electrons only. A brief review is given below.

1.2 Many-Body interactions: Hubbard Model and Heisenberg Model

Although the physics of condensed matter includes solid, liquid, and complex systems, this thesis relates more to the localized electrons in solids where the many-body interaction is strong. A solid is nothing more than a collection of atoms that are close together and periodically arranged on the lattice points. Since the distance between the atoms is small enough, the atomic orbitals and electrons are shared with the nearest atoms through a process called hybridization [17]. It is worth mentioning that the nuclear contribution of atoms can be neglected by the Born-Oppenheimer approximation [18]. Due to the hybridization of atomic orbitals and the sharing of electrons, the entire solid can be understood using the mechanism of many-body interaction. The shared electrons are no longer confined to their parent atomic orbital and can hop to another atomic orbital which is called de-localization [19]. At the same time, since the orbitals of the neighboring atoms are hybridized, the electrons experience Coulomb repulsion. The Hamiltonian for

the many-body system with all these factors can be written as follows

$$H = \sum_{<ij>,\sigma} t_{ij}(a^{\dagger}_{i,\sigma}a_{j,\sigma} + h.c) + \sum_{ijkl}\sum_{\sigma,\sigma'} V_{ijkl}\, a^{\dagger}_{i,\sigma}a^{\dagger}_{j,\sigma'}a_{l,\sigma'}a_{k,\sigma}. \tag{1.1}$$

t_{ij} is a matrix element that represents the hopping between two orbitals i and j. The hopping process is followed by annihilation ($a_{i,\sigma}$) of one electron in the i^{th} orbital and creation ($a^{\dagger}_{j,\sigma}$) of that electron at other orbital j with spin $\sigma(\uparrow)$ or $\sigma'(\downarrow)$. V_{ijkl} is the coulomb repulsion term of an electron. The terms t_{ij} and V_{ijkl} are given by,

$$t_{ij} = \int d^3\vec{r}\,\phi^*_i(\vec{r})(-\frac{\hbar^2}{2m}\nabla^2)\phi_j(\vec{r}), \tag{1.2}$$

$$V_{ijkl} = \frac{1}{2}\int d^3\vec{r}_1 \int d^3\vec{r}_2\, \phi^*_i(\vec{r}_1)\phi_j(\vec{r}_1)V(\vec{r}_1 - \vec{r}_2)\phi^*_k(\vec{r}_2)\phi_l(\vec{r}_2), \tag{1.3}$$

$\vec{r}_1$ and $\vec{r}_2$ are the position co-ordinates of electrons. $\phi_i(\vec{r}_1)$, $\phi_j(\vec{r}_1)$, $\phi_k(\vec{r}_2)$, $\phi_l(\vec{r}_2)$ represent the orbitals. The coulomb repulsion potential between two independent electrons can be written as $V(\vec{r}_1 - \vec{r}_2) = \frac{e^2}{r_{12}}$.

The complicated many-body Hamiltonian can be simplified under a few assumptions, such as (i) only one orbital of the atom at each site of the lattice makes a significant contribution and the rest can be neglected, (ii) the hopping terms are confined to the site and nearest neighbors only, (iii) the Coulomb repulsion between electrons is effectively confined to a single site and these are the same for each site. With these assumptions, the effective Hamiltonian of the many-body system can be simplified as follows

$$H = t\sum_{i=1}^{N}\sum_{\sigma}(a^{\dagger}_{i,\sigma}a_{i+1,\sigma} + h.c) + \sum_{i=1}^{N}\epsilon_i n_i + U\sum_{i=1}^{N} n_{i,\sigma}n_{i,\sigma'}, \tag{1.4}$$

Where $\epsilon_i = t_{ii}$, $t = tij$ are the onsite and nearest neighbor hopping parameters respectively, and $U = V_{iiii}$ is the Coulomb repulsion term for any location between two spins σ and σ'. U is commonly known as the Hubbard parameter. On the one hand, t is the reason for the de-localization of the electrons and on the other hand, U causes the localization of the electrons. The Hubbard parameter U can be attractive ($U < 0$) or repulsive ($U > 0$). The attractive limit of Hubbard U favors

the bonding of two electrons, which is commonly known as Cooper pair formation and can lead to superconductivity [20, 21]. In the repulsive limit of U, on the other hand, the electrons repel each other and exhibit metal-insulator behavior [22**?** , 23]. The mobility of the electrons depends on the competition between the repulsive U and the hopping parameter t and helps to explain the metal-insulator transition. For a sufficiently large t, the electrons are itinerant and behave like the metal (with repulsive U). In the large repulsion limit of U, the electrons are strongly localized at each location and behave as an insulator. The wandering electrons for the single-band Hubbard model were proposed by Kanamori [24], Gutzwiller [25] and Hubbard [26].

The $U/t \to \infty$ limit is the half-filled Hubbard model, where each site contains only one unpaired electron. In this case, the degrees of freedom of the charge are frozen, so the charge gap is very high and the low energy spectrum comes only from the spin interaction mechanism. The best example of a spin system with a high charge gap is the Mott insulator [7]. In these systems, the charge degrees of freedom are frozen and the spin or magnetic properties can be studied independently. As mentioned above, the electrons are strongly localized at the lattice points, and the spin of the unpaired electrons can be either upward or downward, and they interact with each other by exchange coupling $J \approx \frac{4t^2}{U}$ [7].

In a three-dimensional system, the exchange interactions between two electrons can vary in different directions depending on the geometry, and distance between magnetic atoms. Ignoring the weak exchange couplings and in the presence of nonmagnetic atoms in between, the magnetic atoms can be mapped to a single chain. In general, the Hamiltonian for these systems can be written in terms of the exchange couplings as

$$H = \sum_{<ij>} J_{ij}^{\alpha,\beta} S_i^{\alpha} \cdot S_j^{\beta}, \tag{1.5}$$

The single bracket $< ij >$ represents the nearest neighbor interaction through the exchange coupling $J_{ij}^{\alpha,\beta}$ between the spins at the position coordinates i and j. α, β represent the different spin components indices and S is the spin operator. The

product $S_i^\alpha \cdot S_j^\beta$ represents the overlap of different spin components at various sites that arise due to the non-linear geometry such as the formation of the helical chains and anisotropy arise due to the spin-orbit coupling [27, 28]. This Hamiltonian can be modeled in a very simplified way for the different types of exchange coupling. In the presence of bond-directional anisotropy, the Hamiltonian in a general form can be written as

$$H = \sum_{<ij>} J_{ij}^z S_i^z S_j^z + \sum_{<ij>} J_{ij}^x S_i^x S_j^x + \sum_{<ij>} J_{ij}^y S_i^y S_j^y, \tag{1.6}$$

J_{ij}^z, J_{ij}^x, and J_{ij}^y are the exchange interactions along z,x, and y directions respectively between sites i and j. On the other hand, if the exchange coupling between the spins along different directions is the same i.e., J_{ij}^z=J_{ij}^x=J_{ij}^y=J_{ij}, one can model an isotropic system. One of the simplest examples is the isotropic Heisenberg model [29]. The Hamiltonian for this model can be written with the exchange coupling J_{ij} as follows

$$H = \sum_{<ij>} J_{ij} \vec{S}_i \cdot \vec{S}_j, \tag{1.7}$$

where $\vec{S}_i$ and $\vec{S}_j$ are the spin vectors at sites i and j. This model is extensively studied using Bethe Ansatz [30] and numerical techniques [31].

Since, the spin operators S^z, S^x, and S^y do not commute to each other, these can not have simultaneous eigenvectors due to the uncertainty principle and so it leads to quantum fluctuation at 0K [32]. In other words, it means that the alignment of the spins is uncertain. For any anisotropic or isotropic quantum systems having some of the Hamiltonians like Eq.1.10 and Eq.1.7 experience quantum fluctuation. The uncertain spin alignment leads to the exhibit of various kinds of quantum phases. It should be noted that in the low-dimensional spin systems, the confinement effect plays a crucial role, and therefore the quantum fluctuation also dominates in these systems and shows various interesting quantum phases. We review the quantum phases of various kinds of model Hamiltonians for the quasi-one-dimensional spin systems. Before reviewing the quantum phases, let us know about the quasi-one-dimensional spin systems.

1.3 Quasi-One Dimensional Spin Systems

In general, naturally, available magnetic materials form a three-dimensional structure, but in most materials, the exchange interactions vary in strength due to the presence of different atoms and the separation of atoms in different directions. The systems in which the exchange interactions between the spins in one particular direction are much stronger than in the other directions behave like non-interacting spin chains. It is found that in some of the spin systems, the strength of the exchange couplings in the intra-chain or intra-layer is more ($10^2 \approx 10^5$ times) than the inter-chain or intra-layer, and this is why all the magnetic properties come from the chains or layers. In general, these are called low-dimensional spin systems. Depending upon the number of interacting chains say $d = 1, 2$, these are commonly known as one-dimensional or quasi-one-dimensional spin systems respectively. The dominance of the quantum fluctuation over the thermal fluctuation for the antiferromagnetic chains varies exponentially as $e^{-\pi S}$, where S is the total spin magnetic moment [33]. It is quite obvious that the quantum fluctuation is very lafrge for the spin-1/2 chains. This thesis deals with spin-1/2 model Hamiltonians only and therefore we mention some of the spin-1/2 quasi-one-dimensional spin systems. Extensive studies are done on some of these simplest models such as the simple Heisenberg model [30, 34], one-dimensional XXZ model [35–37], Kitaev spin chain [38], J_1-J_2 model [39, 40], zig-zag ladder [41–43], square ladder [44–46], etc. There are also some other complex spin systems such as trellis ladders [47], Kagome strip ladders [48, 49], 3-4 skew ladders [50], 5-7 skew ladders [51], Kitaev ladders [52], etc.

The schematic diagrams for various types of spin chains and ladders are shown in Fig.1.1. In Fig.1.1, one can follow very easily that various kinds of ladders are extensions of other ladders by adding or removing some of the bonds or exchange couplings. $J_1 - J_2$ spin chain and zig-zag spin ladder in Fig.1.1.(b),(c) are the extensions of a normal spin chain in Fig.1.1.(a). Similarly, a normal ladder can be constructed by a normal spin chain by adding the rung exchange couplings. Kagome strip ladder in Fig.1.1.(e) can be formed by adding two decoupled spin

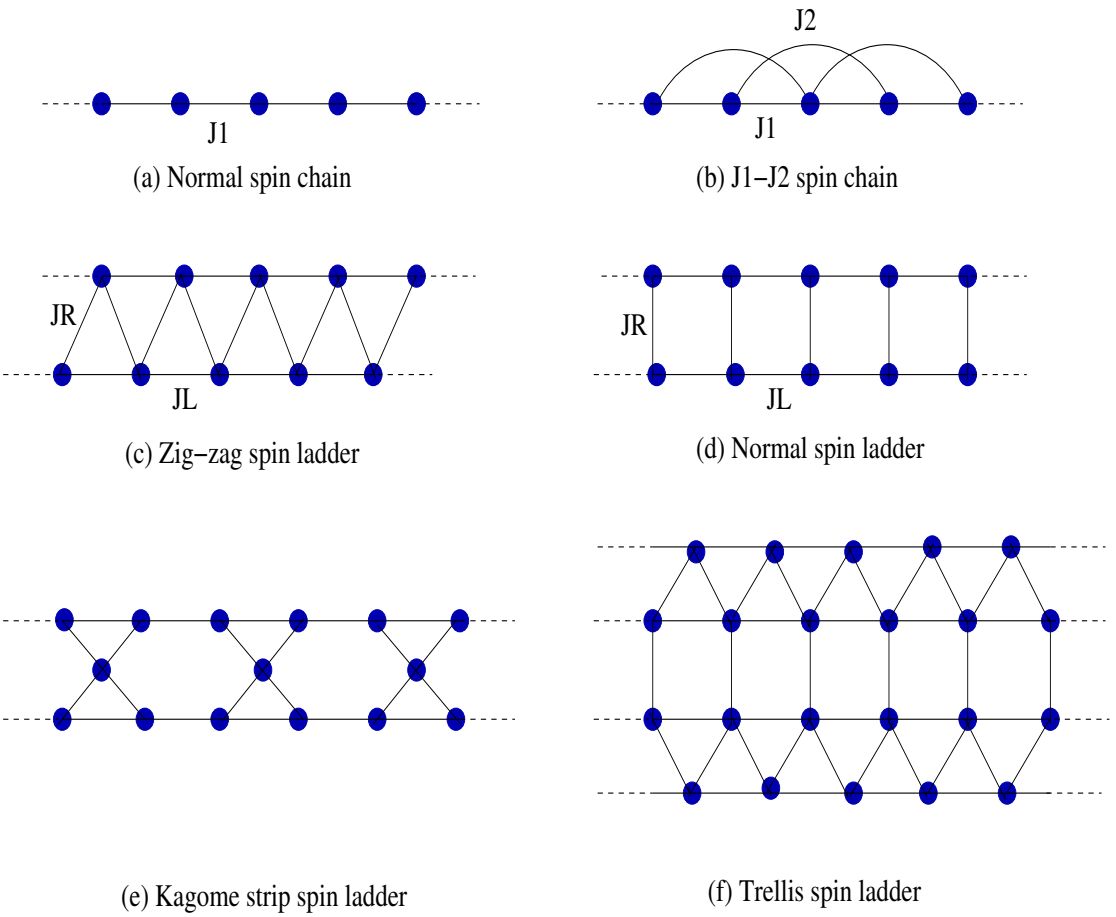

(a) Normal spin chain

(b) J1–J2 spin chain

(c) Zig–zag spin ladder

(d) Normal spin ladder

(e) Kagome strip spin ladder

(f) Trellis spin ladder

FIGURE 1.1: Schematic of various types of spin chains and ladders are shown.

chains via a site in between. The interesting Trellis spin ladder is a combination of normal and zigzag ladders. Similarly, by adding or removing some of the bonds or exchange couplings along rung, diagonal, and third neighbor interaction, one can model any desired spin ladder system [53–55].

There exists plenty of materials that can be mapped to some of the above-mentioned models. For an example, $CuCl_2 \cdot 2N(C_2D_5)$ [56], $KCuGaF_6$ [57], $KCuF_3$ [58] behave as the spin-1/2 antiferromagnetic Heisenberg chains. There are some examples of spin-1/2 chains with the nearest neighbor (NN) ferromagnetic and the next nearest neighbor (NNN) antiferromagnetic interactions also such as $LiCuSbO_4$ [59], $LiCuVO_4$ [60], $LiCu_2O_2$ [61], Li_2ZrCuO_4 [62]. There are many examples of 2-leg, 3-leg, half-twister ladder systems like $SrCu_2O_3$ [63], $Sr_2Cu_3O_5$ [64], $(VO)_2P_2O_7$ [65, 66], $Ba_3Cu_3Sc_4O_{12}$ [67, 68]. The examples of zig-zag ladders are Cs_2CuCl_4 [69], $TlCuCl_3$ [70], NH_4CuCl_3 [71]. There are also many higher

dimensional spin systems such as La_2CuO_4, YBa_2CuO_6 [72] behave as the spin-1/2 square ladder, $LiNiO_2$ [73], Cs_2CuCl_4 [74] and some organic compounds [75] behave as spin-1/2 triangular Heisenberg model. The example of layered honeycomb lattices with antiferromagnetic interactions Na_2IrO_3 [76], Kitaev interactions Li_2IrO_3[77]. The CaV_2O_5 [78], MgV_2O_5 [78] are examples of the spin-1/2 trellis ladders in which the spin-1/2 V_4^+ ions interact along the zig-zag coupling.

However, the complexity of lattice geometry and the number of interacting exchange couplings make these systems many-body in nature and the Hamiltonian of such systems give rise to various kinds of energy spectrum, ground state wavefunction, and excitations. In the next subsection, we discuss the quantum phases of some of the quasi-one-dimensional spin systems.

1.4 Quantum phases in Quasi-One Dimensional Spin Systems

As stated in the Mermin-Wagner theorem [79], there is no possibility of any true long-range ordering for the quasi-one-dimensional spin systems at any finite temperature. On the other hand, at an absolute zero temperature i.e., at $T = 0K$, these spin systems can show long-range ordering (LR0), quasi-long-range ordering (QLRO), short-range ordering (SRO) by staying in the lowest energy level i.e., the ground state [32]. In this state, the wave function describes the true nature of the system. The nature of these conventional ordering can be obtained by calculating the longitudinal and transverse components of the spin-spin correlation in the ground state phases. The various spin-spin correlations are defined in subsection 1.5. However, the effect of the quantum fluctuation, frustration, and competing exchanges are very much dominating and can not be ignored for the quasi-one-dimensional systems [53, 80]. As a consequence, these parameters can give rise to various exotic quantum ground state phases with various kinds of ordered or disordered phases such as ferromagnetic [7], Néel [81], antiferromagnetic [7, 82], spiral [83], dimer [84], Luttinger liquid [85, 86], quantum spin liquid [87, 88], and

magnetization plateau [89] etc. We discuss one by one how quantum fluctuation and frustration play a crucial role in some of the standard quasi-one-dimensional spin model systems.

The effect of quantum fluctuation can be well understood by solving the Hamiltonian of a spin-1/2 isotropic Heisenberg model. The Hamiltonian for the isotropic Heisenberg exchange J which is restricted to only the nearest neighbor atoms can be written as

$$H = J \sum_{<ij>} \vec{S}_i \cdot \vec{S}_j, \tag{1.8}$$

The above model Hamiltonian can be solved by following two approaches (i) classical treatment, and (ii) quantum mechanical treatment. In the classical approach, the Hamiltonian can be written as a function of the angle θ between the spins as $JS^2Cos(\theta)$, where S is the total spin at each site. From this expression, θ in the ground state of the system can be obtained by minimizing the Hamiltonian. From this model Hamiltonian, it is clear that $\theta = 0$ favors the minimization of energy for ferromagnetic exchange, i.e. $J > 0$, and in this case, all spins are oriented parallel to each other $|\uparrow\uparrow\uparrow\uparrow .... \uparrow\uparrow\uparrow\uparrow\rangle$. The energy for the ferromagnetic ground state can be easily obtained as $\epsilon = \frac{NJ}{4}$, where, N is the system size. Whereas $\theta = \pi$ gives the ground state with the antiferromagnetic exchange, i.e. $J < 0$. In this configuration, the neighboring spins are aligned antiferromagnetically $|\uparrow\downarrow\uparrow\downarrow .... \uparrow\downarrow\uparrow\downarrow\rangle$ or $|\downarrow\uparrow\downarrow\uparrow .... \downarrow\uparrow\downarrow\uparrow\rangle$. Either of these configurations is well known as Néel state [81]. The obtained ground state energy of the Néel phase can is $\epsilon = -\frac{NJ}{4}$ for the antiferromagnetic J.

In the quantum mechanical treatment, the ferromagnetic ground state is the same as $|\uparrow\uparrow\uparrow\uparrow .... \uparrow\uparrow\uparrow\uparrow\rangle$. Whereas, the ground state for the antiferromagnetic exchange is different for the quantum mechanical approach. The ground state for the antiferromagnetic exchange coupling can be obtained using the Bethe Ansatz and it gives the energy $\epsilon = \frac{NJ}{4} - NJln2$ [30]. In this case, the ground state phase is a singlet which can be written as $\frac{1}{\sqrt{2}}[|\uparrow\downarrow\uparrow\downarrow .... \uparrow\downarrow\uparrow\downarrow\rangle$ - $|\downarrow\uparrow\downarrow\uparrow .... \downarrow\uparrow\downarrow\uparrow\rangle]$ and this configuration is called the perfect antiferromagnetic state. This is because of the quantum fluctuation and can be understood easily by writing the Hamiltonian in

the second quantized notation as follows

$$H = J\sum_{i=1}^{N}[\frac{1}{2}(S_i^+ S_{i+1}^- + S_i^- S_{i+1}^+) + S_i^z S_{i+1}^z], \tag{1.9}$$

The raising and lowering operators in the above Hamiltonian try to preserve the inversion symmetry and as a consequence, the wavefunction is a superposition of two Néel states. The quantum mechanical treatment makes it clear how much the quantum fluctuation is crucial to deciding the exact quantum ground state. It should be worth mentioning that the Néel phase is a LRO phase, whereas, the perfect antiferromagnetic phase exhibits QLRO due to the quantum fluctuation.

However, with the introduction of bond-dependent exchange couplings in the above Hamiltonian, one can obtain the Hamiltonian for an anisotropic chain. Depending upon the strengths, it can have LRO, QLRO, and SRO in the quantum phases depending upon the competing strengths of the exchange couplings. The Hamiltonian for this kind of spin system with nearest neighbor couplings J^z, J^x, and J^y along z, x, and y directions respectively can be written as

$$H = \sum J^z S_i^z S_j^z + \sum J^x S_i^x S_j^x + \sum J^y S_i^y S_j^y, \tag{1.10}$$

This model Hamiltonian describes the 1-dimensional anisotropic XXZ model. One of the simplest examples of the above Hamiltonian is a spin-1/2 Kitaev ladder [52]. For the various competing limits of these exchange couplings, the Hamiltonian can be reduced to other spin models as well. For $J^x = J^y = 0$, $J^z \neq 0$, the model Hamiltonian represents the Ising model. In this case, it does not have the quantum fluctuation in the model Hamiltonian, and therefore for the antiferromagnetic exchange, the ground state phase is Néel phase which is LRO. $J^x \neq J^y \neq 0$, $J^z = 0$ is the case when the model Hamiltonian describes the anisotropic XY model and it can be solved using Jordan-Wigner transformation [90, 91]. The $J^x = J^y \neq 0$, $J^z = 0$ is the isotropic XY model [92]. The ground state phases for this model Hamiltonian are always co-planar and it exhibits the LRO for the anisotropic XY model i.e., $J^x \neq J^y$, and QLRO for the isotropic XY model i.e., $J^x = J^y$.

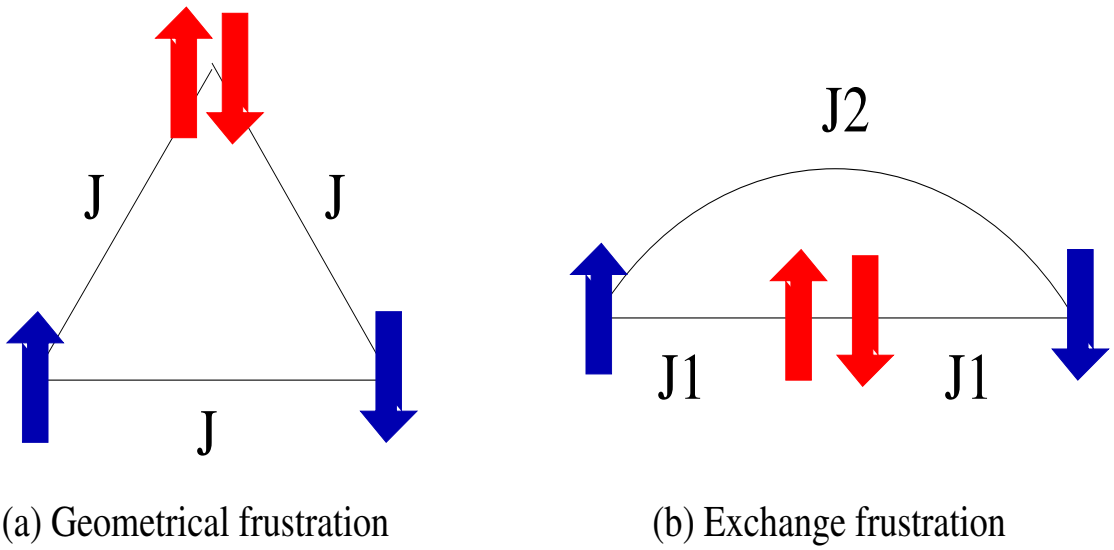

FIGURE 1.2: Various kinds of frustrations are shown in schematics.

$J^x = J^y \neq J^z$ describes the spin-1/2 XXZ model. The model Hamiltonian for the 1-dimensional spin-1/2 XXZ model can be written as

$$H = \sum_{i=1}^{N} [J\frac{1}{2}(S_i^+ S_{i+1}^- + S_i^- S_{i+1}^+) + \Delta S_i^z S_{i+1}^z], \tag{1.11}$$

J is the nearest neighbor exchange coupling along the x and y direction whereas, an axial anisotropy Δ is introduced along the z direction. The quantum ground state phases for this model are always studied as a function of $\frac{\Delta}{J}$, provided J is always antiferromagnetic. Below $\frac{\Delta}{J} = -1$, the system exhibits the LRO ferromagnetic phase [35–37]. Due to the non-vanishing exchange couplings, the system exhibits two kinds of phase transitions below and above $\frac{\Delta}{J} = 1$ [35–37]. The critical regime XY phase is reported below $\frac{\Delta}{J} = 1$ and the antiferromagnetic phase above $\frac{\Delta}{J} = 1$ [35–37].

Frustration is another intrinsic parameter which is significantly contributing to the quantum ground state for the quasi-one-dimensional spin systems. We discuss below the effect of frustration in these kinds of spin systems. Each of the localized spins of these systems may interact with many other spins and hence it can not satisfy all the interactions simultaneously which gives rise to frustration. Frustration might arise due to various geometries and competing strengths of the

exchange interactions. Fig.1.2.(a) represents the geometrical frustration, whereas, Fig.1.2.(b) shows the frustration due to the competing exchange couplings.

In Fig.1.2.(a), all of the spins at three vertices of the triangle are interacting via exchange coupling J. The antiferromagnetic exchange coupling tries to orient each of the spin pairs antiferromagnetically but in this case, the alignment of the spins is not deterministic because of the equal exchange interactions among the three spins. The quantum mechanical treatment of the spin Hamiltonian of the triangle with Heisenberg antiferromagnetic exchange interaction J as shown in Fig.1.2.(a) restricts the total spin to be in $S = 1/2$. The ground state in this spin sector is a linear combination of six possible spin configurations: $|\downarrow\downarrow\uparrow\rangle$, $|\downarrow\uparrow\downarrow\rangle$, $|\downarrow\uparrow\uparrow\rangle$, $|\uparrow\downarrow\downarrow\rangle$, $|\uparrow\downarrow\uparrow\rangle$, and $|\uparrow\uparrow\downarrow\rangle$. With a large collection of many triangles i.e., for a triangular lattice, the spin configurations increase and give highly degenerate disordered ground state phases such as gapless spin liquid which is observed in many triangular lattices such as $YbMgGaO_4$ [93], $PrZnAl_{11}O_{19}$ [94].

Fig.1.2.(b) shows an example of the frustration due to the unequal exchange interaction strengths J_1 and J_2. All of these interactions being antiferromagnetic, try to favor the antiferromagnetic orientation but because of the unequal strengths, all the bonds can not be simultaneously satisfied and give rise to frustration. The simplest example of a frustrated quasi-one-dimensional spin system is the spin chain with competing exchange interactions antiferromagnetic J_1 with the nearest neighbor and antiferromagnetic J_2 with the next nearest neighbor. The ground state phases of this system vary depending upon the strength of J_1 and J_2. It shows many quantum phase transitions by tuning the J_2/J_1 ratio [95, 96]. This system experiences an interesting phase transition at $\frac{J_2}{J_1} = 0.241$ from a gapless QLRO phase to a gaped dimer phase. Interestingly, this model reduces to the well-celebrated Majumder-Ghosh model [39] for $\frac{J_2}{J_1} = 0.5$. At this parameter value, the system exhibits the perfect dimer phase which is doubly degenerate, and the ground state energy at this point is $\epsilon = -\frac{3J_1N}{8}$, where, N is the length of the spin chain. Another model With the nearest neighbor ferromagnetic J_1 and next nearest neighbor J_2 exchange coupling, the system is also found to experience frustration due to the competing exchange coupling. The ground state for this model

is a gapless ferromagnetic state below $\frac{J_2}{J_1} = 0.25$, and an incommensurate spiral phase for the coupling limit $0.25 < \frac{J_2}{J_1} < 0.67$ [96].

There are some isotropic and anisotropic ladder systems as well which exhibit various types of exotic quantum ground state phases due the frustration. A two-leg normal spin-1/2 ladder with its different competing rung and leg exchange limits exhibits various ground state phases. It has already been explored with different ground state phases such as rung-singlet and rung-triplet. All these phases of low-dimensional ladders are very similar to the GS phases of a square lattice of spin-1/2 [97]. There are various kinds of anisotropic spin-1/2 ladder systems where the rung and leg exchange couplings are anisotropic. A ladder system with Heisenberg interaction J_1 along the rung, Ising type interactions J_2 along the leg, and J_3 along the diagonal shows various ground state phases such as Néel, ferromagnetic, stripy leg, stripy rung [98]. There are many fused ladder systems such as $3/5-, 5/7-$ slanted ladders that have magnetic GS and show different interesting GS phases for spin-1/2 and 1 [51].

In the next subsection, we discuss how these quantum phases and boundaries between any two quantum phases can be characterized.

1.5 Level crossing and Spin-Spin Correlation

At the absolute zero temperature, the ground state energy and wavefunction can give an idea about the spin alignment in the system. It is mentioned above that for different limits of the exchange couplings, the same system exhibits various kinds of quantum phases. The exhibition of these quantum phases is spontaneous and it is possible through level crossing of the energy levels, breaking the lattice symmetry, or by breaking any hidden ordering in the system. With the change of the exchange coupling, the low-lying states cross each other at some point in the parameter space and it can indicate a phase transition. At the quantum phase transition point $\frac{J_2}{J_1} = 0.241$ for the $J_1 - J_2$ model with AFM J_1 and AFM J_2, the singlet-triplet crosses each other [99]. The gap between the singlet and

triplet is important to study because this gap vanishes in the thermodynamic limit below $\frac{J_2}{J_1} = 0.241$ [99]. Similarly, the spin gap between the non-magnetic and ferromagnetic phase vanishes at the critical point $\frac{\Delta}{J} = -1$ for the spin-1/2 XXZ model with anisotropic exchange couplings J and Δ as described above. These are examples of the critical points where the level crossing can characterize the phase boundaries. Below and above these phase boundaries, the system has different kinds of ordering in the system. These orderings can be understood by calculating the different components of the spin-spin correlation between the spins. At a distance r from the reference site i, the longitudinal component $C^z(r) = \langle S_i^z S_{i+r}^z \rangle$ and transverse components $C^x(r) = \langle S_i^x S_{i+r}^x \rangle$, $C^y(r) = \langle S_i^y S_{i+r}^y \rangle$ give an idea about the relative spin-alignment among all the spins. The ordering of the spins in various quantum phases can be identified by following the behavior. The power-law behavior of the spin-spin correlation is referred to as QLRO, whereas, with an exponential function, the SRO phases can be identified. The systems can have continuous phase transitions as well with various kinds of topological phases i.e., hidden ordering which can not be identified through level crossing. The infinite-order Kosterlitz thoughtless transition at $\frac{\Delta}{J} = 1$ is an example of a topological phase transition because it does not show any level crossing at this critical point [100–104].

1.6 Quantum Fidelity, Entanglement, and Quantum Concurrence

While mentioning these phases, the other quantum measurements should also be discussed which can characterize the quantum phase transitions and give an idea about the quantum correlation among different parts of the system. In this subsection, we discuss in brief various quantum measurements such as quantum fidelity, entanglement, and quantum concurrence [105, 106].

Quantum fidelity is a quantitative measure of the closeness i.e., the overlap of the wave functions for two different parameter values. The quantum fidelity is equal

to one for a single phase and less than one for two different phases. Near a critical value of the tuning parameter, the fidelity shows a sudden jump from unity and signifies the overlap of the wavefunctions of two orthogonal quantum phases.

The quantum wave function is a superposition of many significant configurations of the system in space. Quantum correlation is a process in which spatially separated particles interact with each other even at great distances. For example, an antiferromagnetic spin-1/2 chain with exchange interaction between the nearest neighbors has a quasi-long-range effect on the spin-spin interaction. On the other hand, quantum entanglement is a quantum phenomenon in which two or more particles share the same wave function without having their independent identities. In other words, the wave function for the whole system cannot be written as the product of the wave functions of the individual participants. For example, the singlet is a two-body wave function that can be written as $\frac{|\uparrow\downarrow\rangle - |\downarrow\uparrow\rangle}{\sqrt{2}}$. Here, the independent wave functions of two digits cannot be written, i.e. the singlet is a maximally entangled state [107]. On the other hand, the wave function of the ferromagnetic state for two sites can be written as $|\uparrow\uparrow\rangle$. The FM wave function can be written as the product of the wave functions of two spins as $|\uparrow\rangle \otimes |\uparrow\rangle$ and so the FM is a product state. To quantitatively measure the entanglement of the wave functions in different phases, one can calculate the von Neumann entropy [108], the quantum concurrence [109], etc. These quantities are very important for the calculation and analysis of ladder systems, as they have many interconnected rungs. For different values of the exchange parameters, these rungs behave independently and are separated from the entire ladder. The quantitative measurement of entanglement plays a crucial role in determining the quantum phase transitions for the ladder systems.

1.7 Magnetization plateau: effect of magnetic field

At an absolute temperature, after the application of a magnetic field, these spin systems can exhibit various non-magnetic, magnetic phases that reside in various magnetization plateaus. The application of the magnetic field may excite the systems to high spin sector states by closing the energy gaps between these two states. This is why the energy gaps among various states and the nature of the wave function of the states become more important in studying the effect of the magnetic field. Depending on the system's energy spectrum and the applied magnetic field, the systems can exhibit various high spin ground state phases. For the gapless systems, these energy gaps are adiabatically closed by the application of a magnetic field, and therefore for the thermodynamic limit, the magnetization vs magnetic field curve shows continuous change. On the other hand, for the gapped systems, the magnetization process is not continuous and can persist in the high spin ground state for a larger range of the applied magnetic field which gives rise to magnetic plateau phases. These plateau phases are connected by sudden jumps which are known as magnetic jumps. These magnetic jumps and plateaus can be understood in terms of the spin gap by satisfying the Oshikawa-Yamanaka Affleck (OYA) criterion [110]. In various gapped phases such as in various dimer phases, these magnetic plateaus are significant.

1.8 Machine Learning for the Spin Systems

The recent development of various machine learning (ML) algorithms has attracted attention in condensed matter physics. Pattern recognition has been useful in detecting the classical phase transition efficiently [111]. The principal components in the case of the fermionic systems [112], Ising model and XY model have also been studied to characterize the quantum phase transitions [113, 114]. ML is an advanced tool in recent times in which the proper choice of the input data set to

various kinds of techniques can help in detecting the quantum phase transitions, the nature of the quantum phases and hidden ordering in the system.

1.9 Outline of thesis

The thesis is organized in the following sequence.

In Chapter 2, we describe the standard numerical techniques such as exact diagonalization, density matrix renormalization group method, and an analytical approach: transfer matrix method. We also describe in brief the machine learning technique's Principal Component Analysis.

In Chapter 3, we study and benchmark the quantum phase transitions for the spin-1/2 $J_1 - J_2$ model by using the machine learning method Principal component analysis.

In chapter 4, a spin-1/2 XXZ model is considered to study the quantum phase transitions using the unsupervised machine learning technique Principal component analysis.

In Chapter 5, the quantum phases, quantum phase transitions, and thermodynamics are studied for a two-leg spin-1/2 ladder with alternate Ising-Heisernberg rung interactions using the exact diagonalization method and transfer matrix method.

In Chapter 6, the same two-leg spin-1/2 ladder system with alternate Ising-Heisenberg rung exchange interactions is studied in the presence of the magnetic field. Various kinds of magnetic plateau phases are studied in this model using the exact diagonalization method and transfer matrix method.

In Chapter 7, the quantum phase transition of a spin-1/2 pyrochlore ladder system is studied. The energy crossover and spin-spin correlation in the system shows a symmetry-broken phase transition in the system.

In chapter 8, we summarize with relevant remarks about all the thesis works and conclude.

Chapter 2

Numerical and Analytical Methods

In the first chapter, we have discussed the complicated Hamiltonian of the frustrated spin systems and also the difficulty in finding the solution of the many-body Hamiltonians. The quasi-one-dimensional spin chains and ladders are the best candidates to see the large quantum fluctuations due to confinement in low-dimensional systems. Therefore, these systems are fascinating for both experimentalists and theorists. Another advantage of dealing with low-dimensional many-body systems is the availability of various numerical techniques to solve these models accurately. Even for the quasi-one-dimensional systems, in the presence of competing exchange interactions or frustration, these Hamiltonians can have various energy spectrums.

There are many methods to solve these many-body Hamiltonians by using various approximated analytical methods like series expansion [115], mean field theory [116], spin wave theory [117], renormalization group [118, 119], Bosonization [120], Bethe Ansatz [30], etc. Whereas, numerical techniques are e exact diagonalization (ED) [121–123], density matrix renormalization group method (DMRG) [124, 125], quantum Monte Carlo (QMC) [126], Numerical RG [127], Tensor Network [128], Matrix Product state [129], etc. Unfortunately, each of these approximate methods

has its limitations. For example, the ED method applies to smaller system sizes. Whereas, the QMC method has sign problems for far away from half-filling for the fermionic systems or frustrated spin systems. The biggest problem with the exponential growth of Hilbert's space with the size of the system, therefore, solving the eigenvalue problem for the exponentially growing Hilbert's space is a Herculean task. The development of new efficient numerical techniques to obtain many body GS is still an open problem for researchers

The recent development in the field of machine learning (ML) to tackle the many-body problem has created a new paradigm and promises to solve many challenges shortly. In the case of spin systems or more generally in condensed matter physics, the ML method has recently proven to be a better tool for computing and analyzing large data sets. Some of the regression methods are widely used to extract experimental data, while some of the ML methods such as principal component analysis (PCA), artificial neural networks (ANN), and convolutional neural networks (CNN) are modified by combining with the previously used conventional methods according to the requirements of theorists. [111, 113].

In this chapter, we discuss the two numerical methods (i) exact diagonalization (ED), and density matrix renormalization method (DMRG). We will also use the machine learning approach to find the quantum phase boundary using the quantum principal component analysis (PCA). At the end of this chapter, we discuss an analytical method called the transfer matrix method (TM).

2.1 Exact Diagonalization

The exact diagonalization method is one the most elegant and sophisticated numerical techniques that deal with the complete set of basis states i.e., the full Hilbert's space. The major advantage of this method is to give the exact eigenvalues and eigenvectors of a given Hamiltonian for only small system sizes therefore solving the eigenvalue problem is impossible. The degree of freedom for N number of sites goes with systems as m^N where m is the per-site degree of freedom. For

Fermionic systems, the per-site m is 4 and can have configurations $|\uparrow\downarrow\rangle$, $|\uparrow\rangle, |\downarrow\rangle$, $|0\rangle$. For spin systems, the degree of freedom m is $2S+1$ where S is the total spin. For example, $S = 1/2$ systems can have configurations $|\uparrow\rangle, |\downarrow\rangle$ and so the no. of configurations goes as 2^N. For the Bosonic case, the number Boson is infinite but for the interacting Bosonic system, the maximum number of degrees of freedom can be restricted to a finite value m without affecting the actual nature of the system. The degree of freedom for the Bosonic systems increases as m^N and the m can be in the range of 2 for hard-core Boson and 4 for soft-core Boson.

Before going to the technical aspects of the ED method, let us briefly discuss how the basis set of a system is generated. The basis of a Fermionic, Bosonic, or spin system can be generated as a string of binary bits of the computer and one or two binary bits represent the degree of freedom for each site for example, the degree of freedom on each site of the Fermionic system can be 4 and bit representation of the configurations $|\uparrow\downarrow\rangle$, $|\uparrow\rangle, |\downarrow\rangle$, $|0\rangle$ $|11\rangle$ are $|10\rangle, |01\rangle, |00\rangle$ respectively. In case of the spin $S = 1/2$ system $|\uparrow\rangle, |\downarrow\rangle$ can be represented as $|1\rangle, |0\rangle$ respectively.

The next step is generating the Hamiltonian matrix in the full Hibert space of the system, and the computation cost of this process is in general as m^{xx} where m is a number of the basis set. The dimension of the basis of the reduced using the different symmetries like rotation symmetry of spins like spin parity, and inversion symmetry due to geometrical symmetries in the system of spin systems. These two symmetries can be explained as follows:

1. Spin parity: The spin-flip operation of one coordinate by an angle π for each site of the systems can be thought of as the parity operation P. The mathematical expression of the spin parity operator gives $P|\uparrow\rangle = |\downarrow\rangle$ and $P|\downarrow\rangle = |\uparrow\rangle$. One can notice that successive operation of the parity operator gives back the same state i.e., $P^2|\uparrow\rangle = |\uparrow\rangle$ and $P^2|\downarrow\rangle = |\downarrow\rangle$. This parity operator forms the abelian group of Z_2 symmetry with two irreducible representations. Similarly, the spin-flip operation may take place for all the coordinates, and in that case, it is called the point-reflection. This symmetry operation is useful for an isotropic system to check the chirality.

2. Inversion: The reflection symmetry of a system concerning a plane or axis is called the inversion symmetry. As an example of a linear chain, the two halves of the system are identical to a line passing through the exact midpoint of the chain.

In many cases, the total spin or z-component of the total spin can also be conserved and each of these spin sector matrices of the Hamiltonian can form a block diagonal Hamiltonian. The dimension of the basis states for different spin sectors S^z goes as ${}^{N}C_{(\frac{N}{2}-S^z)}$ which is less as compared to the number of all the basis 2^N. In the Fermionic system, these symmetries can be electron-hole symmetry at half-filling of a bipartite system, spatial symmetry of geometry of the systems, etc. The total spin or its z-component of the Fermionic system can also be conserved.

The third step of the ED method is to find the eigenvalue and eigenvector of the Hamiltonian matrix, and computational cost to find all eigenvalues and eigenvectors of a given matrix using a standard numerical algorithm goes M^3 where M is the matrix dimension. In most cases, researchers are mostly interested in either the few largest or few lowest eigenvalues of the matrix, and hence the computational cost is even reduced. This cost can further be minimized by choosing a proper algorithm.

There are only a few efficient numerical algorithms to find the ground-state (lowest eigenstate) or low-lying excited states (lowest few eigenvalues or eigenvectors) like the Lanczos [122, 130], modified Lanczos [131], and Davidson algorithms [132]. Davidson algorithm is one of the well-known approaches for dealing with a large symmetric and sparse matrix for finding the low-lying eigenstates [132, 133]. We discuss the Davidson's algorithm below

(a) Davidson's Algorithm:

Davidson's algorithm is suitable for the symmetric sparse matrices. In a sparse matrix, the diagonal terms are quite larger as compared to the off-diagonal matrix elements. This method starts with a set of orthonormal vectors which are slowly rotated in the space to minimize all the off-diagonal terms and finally results in

all diagonal terms i.e., the eigenvalues. This algorithm has two parts: (i) the Ritz-Galerkin approach and (ii) Jacobi orthogonal correction.

(i) Ritz-Galerkin approach: In this step, $V = [V_1, V_2, ..., V_m]$ is the set of orthonormal vectors with a dimension m of real space R. One looks for a vector s so that it satisfies the Galerkin condition which tells about the term $(AVs - \nu Vs)$ should be perpendicular to all the basis vectors i.e.,

$$(AVs - \nu Vs) \perp V_1, V_2, ..., V_m, \tag{2.1}$$

This condition comes up with m number of solutions (ν_j, s_j) for the sparse matrix A. ν_j is called the Ritz value and Vs_j is the Ritz vector. The residual vector r_j can be defined once while looking for the smallest eigenvalue (say m) as follows

$$r_j = (AV_m s_j - \nu_j V_m s_j), \tag{2.2}$$

If r_j is very large then it means that the symmetric matrix is not diagonalized yet. In this case, a vector t is chosen in such a way it follows

$$(D_A - \nu_j I)t = r_j, \tag{2.3}$$

D_A is the diagonal matrix of the sparse matrix A. t is orthonormalized to the other basis vectors $V_1, V_2, ..., V_m$ and added to the space R. This immediately means that the new space has a dimension of $(m + 1)$ with the vectors $(V_1, V_2, ..., V_m, V_{m+1})$.

(ii) Jacobi orthogonal correction: The orthonormal vectors u_j and t holds the condition

$$A(u_j + t) = \lambda(u_j + t), where u_j \perp t, \tag{2.4}$$

λ is the eigenvalue of the matrix A corresponding eigenvector u_j and it can be obtained from the correction equation as follows

$$\lambda = \nu_j + u_j A t, \tag{2.5}$$

Once the eigenvalues are converged, the iteration is stopped.

Retrup's algorithm is a modification of Davidson's algorithm and it works well for the non-symmetric matrix as well. This algorithm similarly starts with a smaller space and iteratively goes for the larger vector space for a better convergence of the desired eigenvalue and eigenvector. A detailed description of this method is given in [134]

The computational cost goes as $N_H^{\frac{3}{2}}$ for Davidson's algorithm and as N_H^2 for Retrup's algorithm. N_H is the dimension of the Hilbert's space. Using these methods, one can solve the matrix of dimension $10^7 \times 10^7$ on a normal desktop. With this restriction, one can easily solve the spin-1/2 systems maximum up to $N = 24$ by using the full Hilbert's space and largest size $N = 36$ by applying the symmetry operations.

Each of the systems in nature tries to stay in a stable state with minimum energy. Due to this fact, the systems preserve some of the symmetries which reduces the degrees of freedom of the system and takes it to the stable state. Despite that, the ED can solve only small system sizes like $N = 18$ with symmetries at filling and $N = 36$ for spin-1/2 system in the singlet sector. In many systems where the correlation length is much larger than the correlation length the finite size effect becomes a big problem to relate these results with the thermodynamic results. To get rid of the finite size effect in the observable of the model Hamiltonian we need to solve the Hamiltonian for larger system size. There are a few approximate methods like various types of quantum Monte Carlo (QMC) for non-frustrated systems, renormalization-based methods like density matrix renormalization group method (DMRG), Tensor network, etc. In this thesis, we discuss one of the most efficient and accurate methods for low-dimensional interacting systems: the DMRG method.

2.2 Density Matrix Renormalisation Group Method

We saw that in the strongly correlated many-body systems, the degrees of freedom increase exponentially and a systematic approach to truncate the large degree of freedom is needed to get accurate eigenstates of the model Hamiltonian. For this, we choose the DMRG method which originates from the idea of renormalization group (RG) and numerical renormalization group (RNG). The RG and RNG are successful in solving the interacting impurity problem, but fail to give accurate eigenstates of the many body correlated models like the Hubbard model, Heisenberg model, and other frustrated spin systems, whereas, the DMRG gives accurate gs energy and wavefunction. We can also calculate the spin-spin correlation and low-lying excitation of correlated low-dimensional systems. Recently this method has also been used to solve the low-laying eigenvalue problem of correlated systems on one, quasi-one dimensions, and two-dimensional systems. In this section, we discuss the DMRG.

The DMRG works based on throwing out the irrelevant degrees of freedom and renormalization of coupling or exchange interaction terms in a systematic manner. The renormalization of the operators and Hamiltonian operators is done at every step while growing the system. The renormalization procedure is followed by the truncation of the irrelevant basis states of the density matrix. This method is state-of-the-art for a one-dimensional correlated system, but truncation error grows in the system as we increase the system's dimension. The entanglement entropy of the system follows the area law and it increases with the dimension of the system. The DMRG calculations are done in two parts; first, infinite DMRG where the system geometry is grown systematically and in the second part the wavefunction of the state is optimized. Let us start with the infinite DMRG method.

In the method, we call the full system a superblock which is divided into four parts: left block, left new site, right new site, and right block. In the first step, we start a small system or superblock of size four sites each of these blocks and sites

is of size one site, and the eigenvalue problem of the superblock is solved using the ED method. In the next step, the superblock is divided into two parts; a system (left block and left new site) and an environment (right new and right block). The wavefunction of the superblock $|\psi\rangle$ can be written as a tensor product of the basis states of the system $|i\rangle$ and environment $|j\rangle$ as following

$$|\psi\rangle = \sum_{i,j} C_{ij}|i\rangle|j\rangle \tag{2.6}$$

The density matrix of the entire super-block can be written as $\rho = |\psi\rangle\langle\psi|$. The matrix elements of the density matrix can be written as below

$$\rho_{ij} = \sum_{k} C^*_{ik} C_{kj} \tag{2.7}$$

, We now diagonalize the ρ to get the eigenvalues and eigenvectors and only the largest eigenvalues and corresponding eigenvectors are retained and the rest of the degree of freedom is thrown out. The retained eigenvectors form a reduced density matrix ρ'. If the density matrix has the dimension $M \times M$ (say) and only m number of significant eigenvalues are considered then the dimension of the reduced density matrix becomes $M \times m$.

The re-normalization procedure follows the construction of the reduced density matrix ρ'. Any operator O and Hamiltonian matrix H can be re-normalized respectively to $\tilde{O} = \rho'^{\dagger} O \rho$, $\tilde{H} = \rho'^{\dagger} H \rho$. Here, O is spin raising, lowering, S^z operators, the Hamiltonian matrix, or any correlation function operators we want to compute for a spin model Hamiltonian system.

We now form the superblock made up of left or right block and left new and right new site. The new left and right blocks are of size two sites and new sites are of size one site. We keep repeating the above procedure till it reaches the desired system size. In the finite DMRG algorithm, we keep the system size the same and keep repeating the renormalization procedure by increasing and decreasing the left and right blocks and zipping the blocks back and forth to optimize the wave function.

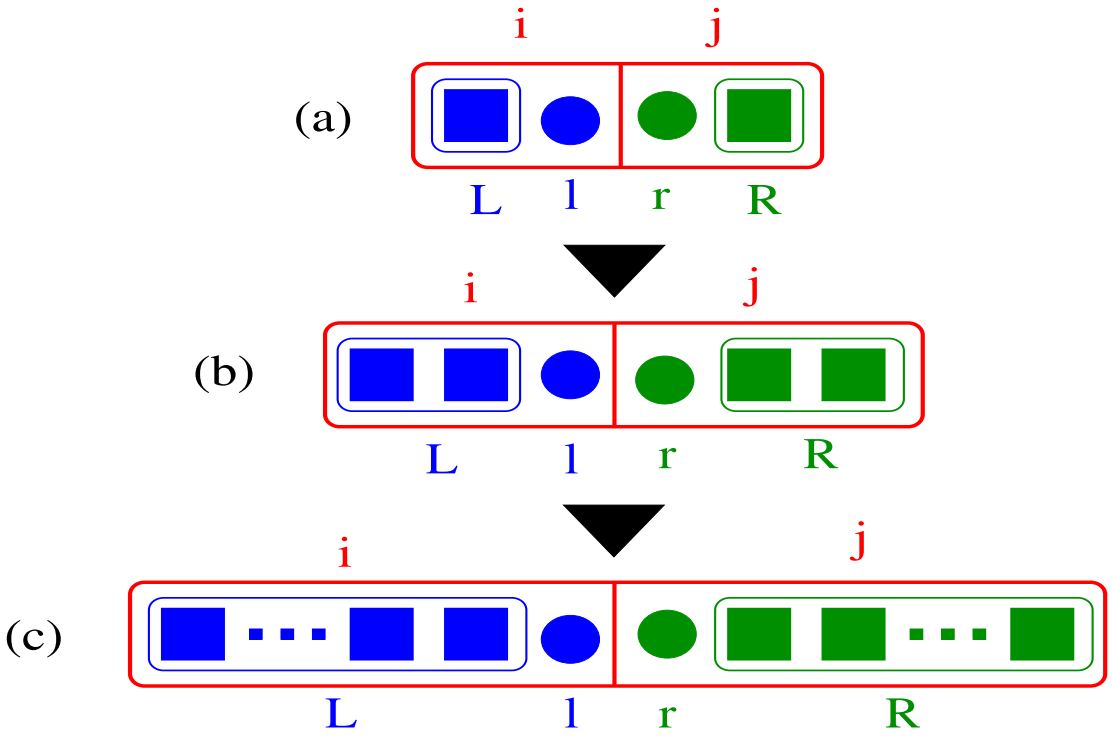

FIGURE 2.1: Schematic for Infinite DMRG step. Each big square box represents each site and each of the rectangles represents a single block. The circles represent the new site. The small square boxes represent the continuation of many sites in the block. The blue color is used for the left block (system) and left new sites. The green color is used for the right block (environment) and the right new site. The red color rectangle represents a superblock divided into two parts: system (i) and environment (j).

The pictorial depiction of infinite and finite of the DMRG algorithm for a spin-1/2 chain geometry is shown below:

(i) Infinite DMRG

(a) Initial superblock formation: An initial superblock is formed with 4 sites as shown in Fig. (a). The left block has one site and left new site. The left block left new, right block, and right now all have one site each initially.

(b) Diagonalization of the Superblock Hamiltonian: The Hamiltonian of the superblock of the 4 site is diagonalized to get the eigenvalues and eigenvectors.

(c) Density matrix: Density matrix ρ is obtained from the eigenvectors.

(d) Decomposition of the blocks: The wavefunction for the superblock is decomposed and written for two individual blocks.

(e) Addition of new sites to the blocks: One new site is added to each of the blocks as shown in Fig. (b). The new sites are kept adding untill the dimension of the density matrix becomes large.

(f) Reduced density matrix: Once the dimension of the density matrix M becomes greater than the cut-off dimension m, the reduced density matrix ρ' is calculated and used in the next steps.

(g) Infinite number of sites addition to the blocks: The reduced density matrix is further used for the renormalization of the operators for the blocks and new sites. This procedure is followed untill the desired system size is achieved.

The above schematic is shown for a 1-dimensional spin chain and it is clear that the blocks are far apart. Although, the connections between the blocks do not affect the wavefunction the addition of the new sites changes the shape of the wavefunction once one keeps increasing the system size. This is why the wavefunction obtained in the infinite process may not be accurate enough and the finite DMRG process is required.
(ii) Finite DMRG

(a) Right sweep initialization: After the completion of the infinite step, the wavefunction of the superblock has two equal blocks of half block length $\frac{N}{2}$. But during the sweep process, the superblock is divided into two unequal blocks as shown in Fig . (b). For the right sweep, the right block is short by one site from the half-block length, whereas the left block has one extra site from the half-block length.

(b) Right sweep untill the last site in the right block: In the next right sweep, the right block is further decreased by one site whereas the left block is added by one more site as shown in Fig. (c). This procedure is followed until it reaches the minimum right block length.

(c) Left sweep: Once the right sweep is done, the process is reversed. In the left sweep, the new sites are now added to the right block and reduced to the

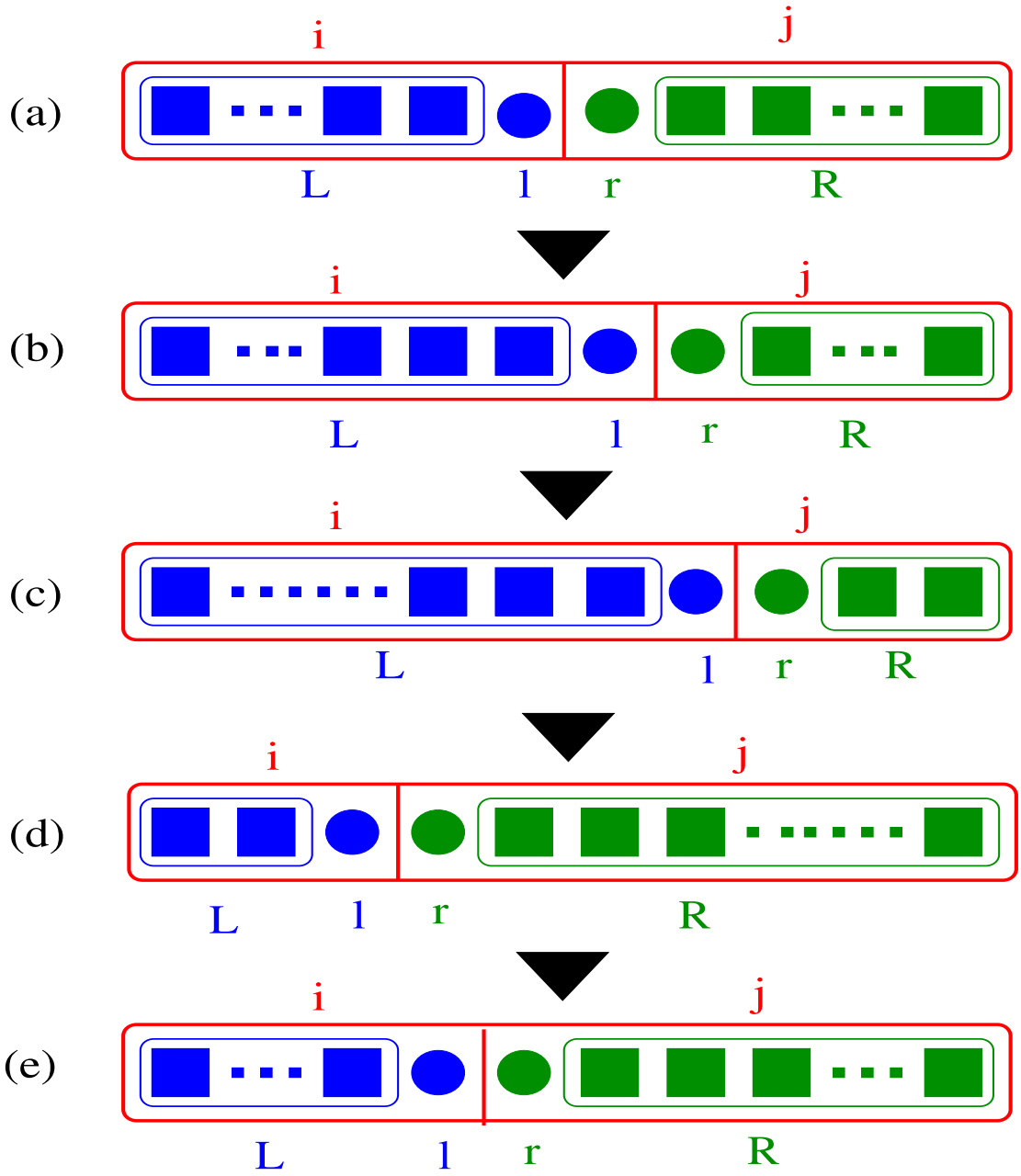

FIGURE 2.2: Schematic for finite DMRG step. Each big square box represents each site and each of the rectangles represents a single block. The circles represent the new site. The small square boxes represent the continuation of many sites in the block. The blue color is used for the left block (system) and left new sites. The green color is used for the right block (environment) and the right new site. The red color rectangle represents a superblock divided into two parts: system (i) and environment (j).

left block. This sweep is followed until the left block reaches a minimum of one site.

(d) Completion of the sweep: The new sites are added to the left block again and the sweep goes on until two blocks become of equal length.

Usually,$5 - 7$ sweeps are more than sufficient to get the accurate wavefunction for the low-lying states for the chains. This method can also be used for various geometries, and the accuracy of the result depends on the number of eigenvectors kept in the renormalization procedure. There are many other specialized DMRG algorithms to get more accurate results in quasi-one-dimensional systems like Y-junction, ladders, Bethe lattice, etc. The thermodynamical properties can also be calculated using the transfer matrix renormalization group (TMRG) approach. Recent developments in the DMRG algorithm like the hybrid ED/DMRG method have made it possible to get very low-temperature properties of these correlated systems.

Unfortunately, the DMRG method gives excellent accuracy only for low-dimensional correlated systems, but for two or three-dimensional correlated systems no numerical or analytical method can give an accurate solution. Therefore, we explore the machine learning approach to solve these many body systems. In the next section, we explain supervised and unsupervised machine approaches and then focus on the principle component analysis method which is generally used in unsupervised machine learning.

2.3 Machine learning and principal component analysis

In recent times, machine learning techniques have nowadays used extensively for weather forecasting, pattern recognition, data analysis, etc. There are various categories of machine learning techniques such as supervised machine learning methods, unsupervised machine learning methods, and reinforcement machine learning

methods, etc. In the supervised machine learning method, a set of data sets is trained first, and then using the trained machine, other sets of new data sets are predicted. For example, the temperature at different places in Delhi, Kolkata, Mumbai, and Chennai are regularly noticed and trained to a system over the year. In the next year, the trained data can be used for weather prediction accurately. The online shopping platforms use supervised machine learning techniques extensively and customers' data are used for initial guess for the algorithm. The trained machine recommends the customers' favorite products. In the reinforcement learning method, the machine is trained every time to improve its accuracy and this method is similar to the supervised machine learning method, but unlike the supervised machine learning method, in this algorithm, the machine is rewarded every time for its prediction. Based on the reward, the training gets even more improvised. In the physical world, this method is still underutilized because of its complicated and time-consuming process. Supervised ML works when data follows the previous trend. Any new pattern can not be detected with the supervised machine learning method and it again requires training. Whereas, the unsupervised machine learning method can recognize the new pattern from its input data set itself. Pattern recognition is very similar in the mathematical world to finding the maxima, and minima of a curve or finding the best data set with minimum or maximum variances.

Unsupervised machine learning methods are of different types. One of the most significant varieties we discuss here is the dimensionality reduction method. The reduction of the large dimension of a data set or the features to only a few without losing the significant data is called the dimensionality reduction method. Principal Component Analysis (PCA) is one of the promising unsupervised machine learning techniques that is based on the dimensionality reduction process. Depending upon the input feature, this method reads the input data set and helps in finding out the most significant dimensions or a few directions which has the maximum variance. These directions are known as principal component vectors or weight vectors. The PCA can be described in the following steps

(a) Data Matrix Y: A large set of data is collected to form a data matrix Y. Each of the features of a data set is put along each column in the data matrix Y. The features might be length, height, weight, temperature, pressure, spin magnetic moment. Whereas each row represents a sample data set. A large set of samples are used for various tuning parameters. Let us assume that the dimension of the feature is L and the number of samples is m for n set of tuning parameters. So, the total length of the row is $N = M \times m$. Usually, m is lesser than N.

(b) Data Centre Matrix X: PCA works well for the input data with linear variations. To linearize the input features, each column of the data matrix is written around the column mean. The column mean can be obtained as $\mu_k = \sum_i Y_{ik}$. Where, Y_{ik} is the matrix element and i,k represents the row, and column indices. Each element of the data-centred matrix X can be written as $X_{ik} = Y_{ik} - \mu_k$.

(c) Co-variance Matrix C: The covariance matrix C can be written as

$$C = X^T X \tag{2.8}$$

The X^T is the transpose of the data-centred matrix X. The dimension of the covariance matrix is $m \times m$. The diagonal terms of the covariance matrix can be written as C_{ii} and these are called the variance, whereas, the off-diagonal matrix elements can be written as C_{ij} which is called co-variance between two axes i and j.

(d) Diagonlization of Co-variance Matrix C: One can understand that the co-variance matrix of dimension L can be easily obtained starting from a large data matrix Y of dimension $N \times m$. The diagonalization of the covariance matrix is quite feasible because it does not depend upon the size of the sample N.

(e) Weight Vectors of Co-variance Matrix C: The covariance matrix C gives the L number of eigenvalues λ and eigenvectors w. The eigenvector with

the largest eigenvalue of C represents the directions which has maximum variance and can be called as first principal component vector or first component weight vector. The eigenvector with the second largest eigenvalue is called as second principal eigenvector or the second principal weight vector. The other eigenvalues and eigenvectors can also be defined similarly. It is noticed that only a few eigenvalues have the largest values and the rest of the eigenvalues can be ignored. In other words, one can think that with the help of only a few principal eigenvectors have the most significant variances and so the complete data set can be understood in terms of these only.

(f) Principal components of Co-variance Matrix C: The eigenvalues $\lambda_1, \lambda_2, \lambda_3, ...$ and eigenvectors $w_1, w_2, w_3, ...$ of the co-variance matrix are in rotated basis (due to the diagonalization) and for complete understanding, the complete data set Y should be projected along these principal eigenvectors or weight vectors. The projections of the data matrix elements along these eigenvectors are called principal components. The principal components can be written as

$$p_n = w_n \times Y^T \tag{2.9}$$

The eigenvector w_n and the transpose of the data matrix i.e., Y^T have the dimension $L \times L$ and $L \times N$ respectively. p_n is a column vector of dimension N which contains N principal components corresponds to the n^{th} weight vector. The principal components for various indices n can be plotted to understand. The scatter plot of any two values of n can be plotted in a 2-dimensional plot which can give an idea about the overlap or correlation among the data points.

(g) Quantification of the principal components of Co-variance Matrix C: Sometimes, it is difficult to understand the overlap among the data and also difficult to follow the change in the data set as a function of the tuning parameters. To simplify, the principal components can be quantified accordingly. If the sign of the principal components does not cancel each other,

can be quantified easily by adding those as following

$$q_n = \sum_i (p_n)_i \tag{2.10}$$

$(p_n)_i$ is each of the principal components of the column vector p_n. q_n is called a 'quantified principal component'.

2.4 Transfer Matrix Method

The transfer matrix method is a mathematical technique that is quite frequently used in statistical mechanics to write the partition function in a simpler form. This method is exact when the interaction term of one unit commutes with that of the neighboring unit in the lattice system. One can calculate the average thermodynamic properties using the compact partition function of a unit cell of the system. In this case, the partition function is nothing but the trace of the transfer matrix for the entire system. In this thesis, we deal with some of the ladder systems where the entire system can be divided into many geometrical units and It is also noticed that their Hamiltonian commute to each other.

As shown in Fig. (a), the entire system consists of two types of sublattice units A and B. It is shown that the geometrical units $i-1$, i, and $i+1$ are connected via a dashed line. This dashed line means that each of these geometrical units is connected in such a way that the Hamiltonians of these units commute to each other. The commutation relations can be written as follows

$$[H_1, H_2] = [H_2, H_3] = ... = [H_{i-1}, H_i] = [H_i, H_{i+1}]... = [H_{n-1}, H_n] \tag{2.11}$$

The Hamiltonian of the entire system can be written as

$$H = \sum_i H_i \tag{2.12}$$

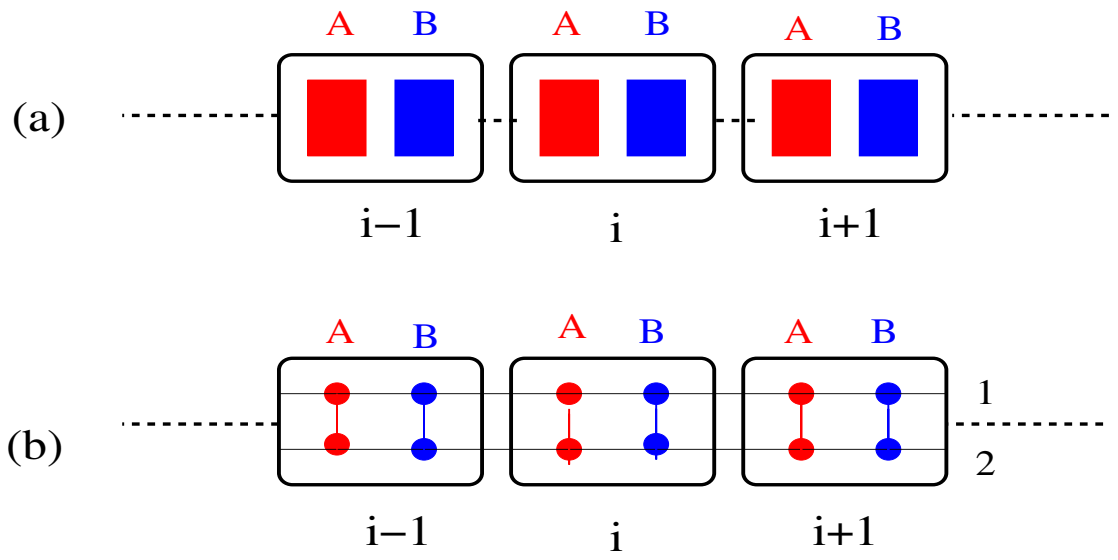

FIGURE 2.3: (a) Schematic for a system with two sublattice units A and B shown in red and blue colors respectively. (b) Schematic shown for a two-leg ladder. the numbers 1, 2 represent the leg indices. A and B represent two types of sublattices A and B. Each sublattice unit has two spins. The spins are shown using red and blue circles.

The partition function for the entire system can be written as

$$Q_N = Tr(e^{-\beta H}) = Tr(e^{-\beta \sum_i H_i}) Q_N = [Tr(e^{-\beta H_i}]^n \tag{2.13}$$

Here, N is the system size and n is the number of geometrical units. β represents the inverse temperature. From the above partition function, one can get the thermodynamic quantities using the standard formula.

A two-leg spin-1/2 ladder system is described in Fig. (b) which is very similar to Fig. (a). In this ladder system, each A and B are consisted of two spins shown in circles. Although, blocks A and B are of two types, each of the geometrical units are identical. For example, we consider a spin-1/2 ladder system with alternate Ising-Heisenberg rung interactions. Let us assume that the red blocks represent the spins connected by Heisenberg-type bonds and the blue blocks represent the spins connected by the Ising-type interactions. The exchange interaction along the leg is considered to be an Ising type so that the Hamiltonian of each of the individual geometrical units commute. The above commutation relation can be

followed for this ladder system as well. A spin-1/2 ladder is studied rigorously in Chapters 5 and 6.

Chapter 3

Machine learning approach to study quantum phase transitions of a frustrated one dimensional spin-1/2 system

3.1 Introduction

The study of quantum fluctuations and phase transitions is one of the most active and frontier areas of condensed matter physics [7, 135–143], especially these studies are relevant and interesting in presence of many-body interactions [144–150]. These correlated model systems are important and relevant for modeling the real materials and have exotic phases in the ground state (GS), but solving even the simplest correlated model Hamiltonian is extremely difficult due to a large number of coupled degrees of freedom [7, 137, 138]. The degrees of freedom of a fermionic model system, like the one-band Hubbard model, increases as 4^N, where N is the number of sites [7, 137, 138]. In large electronic repulsion energy limit, the charge degrees of freedom freeze, and in the half-filling limit, this model reduces to antiferromagnetic Heisenberg spin-1/2 model system where degrees of freedom increase

as 2^N [7, 137, 138]. Unfortunately, there are only a few models like one dimensional (1D) regular Heisenberg spin-1/2 [30, 151] and Hubbard model [152, 153] which can be solved exactly. In most of the cases, these models are solved by approximate analytical methods like mean-field [154, 155], bosonization theory [156], renormalization group theory [157] etc or numerical methods like exact diagonalization (ED) for small systems [158, 159], density matrix renormalization group method (DMRG) [160–163] or quantum Monte Carlo (QMC) [164, 165] etc. Most of these techniques have their limitations like the DMRG can be applied only to low dimensional systems, and the QMC has sign problems [164] for frustrated spin systems or fermionic systems away from half-filled limit. Therefore, it is desirable to find an approach or method to determine the quantum phase boundary by supplying only minimal information like solving a small system by using the ED method or giving some information about a particle or spin configurations even in the presence of sign problems of the QMC method [166]. Machine learning (ML) is one of the most promising approaches to find solutions of complicated many-body model Hamiltonian [167–174].

The ML is an indispensable tool to study various problems of different academic and social domains and has been heavily used in image recognition [175–177], social networking [178–180], advertising [181], finance [182], designing medicine [183] etc. In science, biological physics [184, 185], high energy physics [186, 187] and other disciplines used this tool for various purposes. In the preponderance of information and real data, ML is an excellent tool to explore and quantify patterns. There are two types of approaches in ML; supervised and unsupervised learning, in supervised learning the algorithm is provided with any pre-assigned labels or scores for training the data [167, 168, 171, 188–191], whereas the unsupervised learning algorithm discovers naturally occurring pattern in training data sets [192, 193]. In this manuscript, unsupervised learning will be our main focus to find the naturally occurring pattern.

In a strongly correlated system, data are multivariate, highly correlated, and multidimensional, but to discover the pattern in the data set, unsupervised learning first reduces the dimensionality without losing the information of variance. Principal

component analysis (PCA) is a method to reduce the dimensionality of a data set consisting of a large number of interrelated variables without losing variation in the given data set. The dimensionality reduction is achieved by transforming the original data set to a new set of variables or the principal components (PCs) which are uncorrelated and ordered so that the first few axes of the subspace retain most of the variation present in the original variables [171, 194–196]. The PCA is one of the most efficient tools to predict the thermal phase transitions in two-dimensional (2D) spin systems like- phase transition in the classical Ising model and XY model as a function of temperature T [197–199].

The PCA method works well to determine the thermal phase transitions in classical model systems [197–199] but it is still open for the quantum systems. However, some of the works have been done in recent times using PCA for different Hamiltonians and under different limitations. Costa et. al. [174] show that PCA succeeds in determining fermionic critical points at a finite temperature only when there is no sign problem. PCA is also used in the Qi-Wu-Zhang (QWZ) model but it fails in determining the transition lines due to the non-linear input data set [200]. Whereas, PCA of entanglement spectra successfully shows the cluster formation by separating various phases [201]. The combination of PCA and t-distributed stochastic neighboring ensemble (t-SNE) method is also used to observe the magnetic transition at finite temperature [202]. So, the determination of quantum phase transitions (QPT) for the frustrated spin models using PCA is scant in the literature. In this manuscript, we consider a 1D frustrated antiferromagnetic Heisenberg spin-1/2 $J_1 - J_2$ model to explore the quantum phase transitions [96, 99, 142, 148, 149, 203–205]. This model has nearest neighbor antiferromagnetic spin exchange interaction J_1 and next nearest neighbor anti-ferromagnetic interaction J_2. This is one of the simplest frustrated model systems irrespective of the nature of J_2 and one of the well-studied models [96, 99, 148, 203, 204] and it is perfect to benchmark quantum phase transition with a new method. This model shows a gapless spin liquid (GSL) phase below J_2/J_1=0.2411, where the spin-spin correlation shows the quasi-long range ordering (QLRO) and a dimer phase thereafter. A spiral phase sets in at $J_2/J_1 \approx 0.55$. The quantum phase

transition from the GSL phase to the dimer phase is determined using level crossing between the first excited state (FES) singlet and lowest triplet states in finite systems or by calculating the singlet-triplet gap in the thermodynamic limit [96]. This model is known as the Majumdar-Ghosh (MG) model for $J_2/J_1 = 0.5$ and has a doubly degenerate GS [142]. The GS of the MG model can be written as the direct product of all dimers, and the lowest singlet-triplet gap of this model is large [206, 207]. For $0.55 < J_2/J_1 < 2.27$, this model exhibits a spiral phase and in this phase, the GS is doubly degenerate only at specific values of J_2/J_1 for finite size systems [205].

Interacting model systems are hard to solve due to exponentially increasing degrees of freedom with system size. Therefore, various methods are used with their limitations like ED for small systems, QMC [164, 165] for non-frustrated systems, and DMRG [160–163] for low-dimensional systems. In our work, the main goal is to use the PCA to find the QPT in the spin-1/2 $J_1 - J_2$ model using the most probable spin configurations (MPSC). The MPSCs are used as input to the PCA to find the principal components. We propose an approximate numerical method where we start with an initial guess basis and then generate a new basis by acting the Hamiltonian on the previous basis. We call this method an iterative variational method (IVM). A detail of this method is given in section 3.2. The IVM can be used efficiently to generate MPSC for larger system sizes. We show that MPSC generated from the IVM can be used as input of PCA which is discussed in section 3.3. We explore the quantum phase transition and GS degeneracies in the $J_1 - J_2$ model using PCA. We consider a few MPSCs in the GS and the FES as input of the PCA for various values of J_2/J_1 and these MPSCs are obtained using ED. We show that the MPSCs corresponding to the FES for a given value of J_2/J_1 predict the GSL to dimer phase transition faithfully. It also predicts the degeneracies in the GS. It is amazing to see that only a few MPSCs with uniform weight can predict phase transitions and all the degeneracies. To the best of our knowledge, the combined IVM-PCA approach is used for the first time to predict the quantum phase transition, and degeneracies using the MPSCs and it is shown to work for $J_1 - J_2$ model.

This manuscript is divided into five sections. In section 3.2, the model Hamiltonian and methods are discussed, whereas in section 3.3 the PCA and its implementation in this system are explained. The section 7.3 describes the results and has three subsections. In the last section 6.5, our results are summarised and compared with the results of the literature.

3.2 Model Hamiltonian and Methods

In this work, a frustrated Heisenberg antiferromagnetic spin-1/2 $J_1 - J_2$ model is studied and in this model, spins are interacting with their nearest neighbor and next nearest neighbor spins with exchange interactions J_1 and J_2 respectively. The Hamiltonian of the system can be written as

$$H = J_1 \sum_i \vec{S}_i \cdot \vec{S}_{i+1} + J_2 \sum_i \vec{S}_i \cdot \vec{S}_{i+2} \tag{3.1}$$

where $\vec{S}_i$ is the vector spin at site i, the first and second terms of the Hamiltonian represent the nearest and next nearest neighbor spin exchange interaction terms. Both the exchange interactions J_1 and J_2 are antiferromagnetic. In large J_2 limit, this interaction topology can be mapped to a Heisenberg model on a zigzag geometry or two spin chains coupled with each other through zigzag rung bonds [207].

In IVM, we use truncated Hilbert's space (THS) of the system for each iteration. Initially, we start with few guess configurations ($|\phi_1^0\rangle$, $|\phi_2^0\rangle$, $|\phi_3^0\rangle$, $|\phi_4^0\rangle$). The superscript represents the step-index of iteration and the subscript is the basis index in the THS. In $J_1 - J_2$ model, the GS is singlet in $J_2 = 0$ limit and the most trivial spin configurations will be $|\phi_1^0\rangle = |\uparrow\downarrow\uparrow\downarrow \ldots\ldots \uparrow\downarrow\uparrow\downarrow\rangle$ and $|\phi_2^0\rangle = |\downarrow\uparrow\downarrow\uparrow \ldots\ldots \downarrow\uparrow\downarrow\uparrow\rangle$. Whereas, in strong J_2 limit, the other two configurations can be $|\phi_3^0\rangle = |\uparrow\uparrow\downarrow\downarrow \ldots\ldots \uparrow\uparrow\downarrow\downarrow\rangle$ and $|\phi_4^0\rangle = |\downarrow\downarrow\uparrow\uparrow \ldots\ldots \downarrow\downarrow\uparrow\uparrow\rangle$. Therefore, we use these four initial configurations in $0 < J_2/J_1 < 1$ limit.

TABLE 3.1: $n_l(L)$ is the percentage of basis used for l^{th} iteration with system size L. $\Delta e_l(L)$ is the percentage error in the GS energy for the l^{th} iteration.

l	$n_l(16)$	$\Delta e_l(16)$	$n_l(20)$	$\Delta e_l(20)$	$n_l(24)$	$\Delta e_l(24)$
3	26.88	7.43	4.93	11.02	0.57	12.79
4	63.33	0.51	19.99	5.77	3.21	8.79
5	87.07	0.06	42.23	0.80	12.04	5.43
6	97.02	0.01	77.15	0.05	30.35	0.92
7	99.50	0.01	94.59	0.01	52.58	0.11

Starting from these initial configurations, a few new configurations are generated by acting the Hamiltonian H in Eq.3.1 on the previous basis states as follows-

$$\sum_{k'=1}^{N_{l-1}^{THS}} H|\phi_{k'}^{l-1}\rangle = \sum_{k=1}^{N_l^{THS}} h_k|\phi_k^l\rangle. \tag{3.2}$$

N_{l-1}^{THS}, N_l^{THS} are a total number of basis or the dimension of the THS in the $(l-1)^{th}$, l^{th} iterations respectively. h_k are the coefficients of the new basis $|\phi_k^l\rangle$ for the l^{th} iteration. This procedure is performed up to a few sufficiently finite iterations to reach a sufficiently larger dimension of the THS and then the Hamiltonian matrix is diagonalized to obtain the GS and the FES eigenvalues and eigenvectors. Then we analyze the convergence of the GS energy, and the FES energy as a function of the iteration step l. The percentage of the basis used is defined as $n_l = 100 \times \frac{N_l}{N_{ED}}$ and the percentage error in energy is defined as $\Delta e_l = 100 \times \frac{E_{ED}-E_l}{E_{ED}}$. Where, N_{ED}, N_l are the dimensions in the exact diagonalization method and IVM respectively. Similarly, E_{ED}, and E_l are the energies for the same set of methods respectively. It is to be mentioned that for three system sizes $L = 16, 20, 24$ the dimension of total basis states in $S^z = 0$ sector are $N_{ED} = 12870, 167960, 2704156$ respectively. The exact GS energies are $E_{ED} = -7.7666, -9.7446$ and -11.8035 for these three system sizes respectively for $J_2 = 1.00$.

We employ the method to the model in Eq.3.1 and diagonalize the Hamiltonian matrix for different iterations l. We analyze the GS and the FES energy convergence calculated from the method IVM. n_l and Δe_l for the GS are shown as a function of the iteration step l in Table 6.1 for $J_2 = 1$. We note that with the

percentage of basis $n_l = 63\%, 42\%$ and 30%, the GS energy converges with percentage error Δe_l less than 1% for the system sizes $L = 16, 20$ and 24 respectively. To achieve better convergence, the required number of iterations l increases with system size, however, the required percentage of basis n_l reduces with L. We also notice that for $L = 28$, n_l is wa 20% for the 7^{th} iteration, which implies n_l is almost linear with $\frac{1}{L}$. We show in Fig. 3.1. (a), the GS and in Fig. 3.1. (b), the FES energy as a function of J_2/J_1 for system size $L = 24$ for the iterations $l = 5, 6$ and 7. In the case of $l = 5$, both the GS and the FES energies are poorly converged but these converge well with $l = 7$ for $L = 24$. From the Table6.1 and the Fig.3.1, we notice that in $l = L/4 + 1$ iterations, energy convergence is higher than 99% in the regime $0 < J_2/J_1 < 1$. For the $S^z = 1$ sector calculation, all the basis ($|\phi_1^0\rangle$, $|\phi_2^0\rangle$, $|\phi_3^0\rangle$, $|\phi_4^0\rangle$) with flipped spins at each site are considered as the initial guess basis.

The GS wavefunction $|\psi_0>$ and the FES wavefunction $|\psi_1>$ are calculated. The singlet-triplet (ST) gap can be written as

$$E_{ST} = E_0(S^z = 1) - E_0(S^z = 0) \tag{3.3}$$

where $E_0(S^z = 0)$ and $E_0(S^z = 1)$ are the lowest energy levels in $S^z = 0$ and 1 sector i.e., the lowest energy level in the singlet and triplet sector respectively.

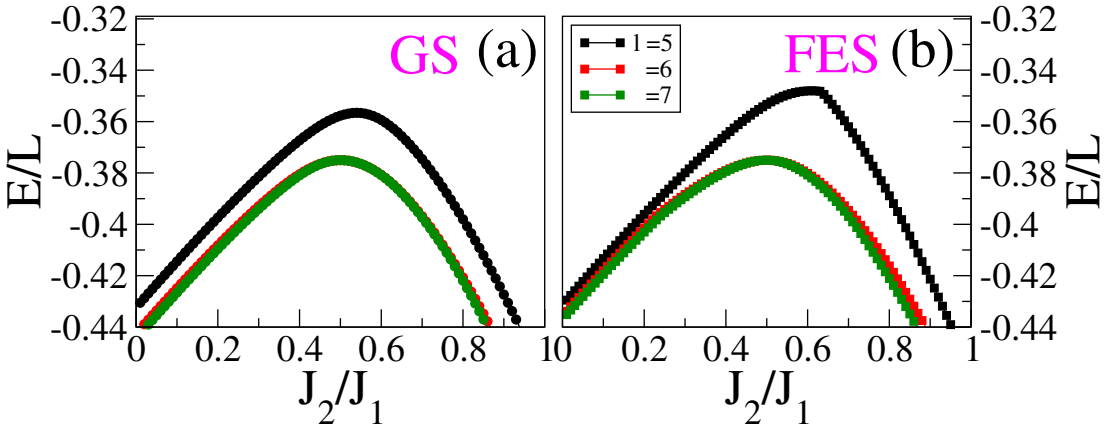

FIGURE 3.1: (color online) (a) GS energy and (b) FES energy per site E/L as a function of J_2/J_1 using IVM. All the figures are shown for the system size $L = 24$. Black, red, and green colors are for the iterations $l = 5, 6$, and 7 respectively.

The lowest singlet excitation E_σ can be written as

$$E_\sigma = E_1(S=0) - E_0(S=0) \tag{3.4}$$

where $E_1(S=0)$ and $E_0(S=0)$ are the lowest and the FES energies in total spin $S=0$ sector respectively. For all the calculations, we impose the periodic boundary condition in the spin chain, and the IVM is performed for three different system sizes $L = 16, 20$, and 24. All the calculations are obtained for the wider regime of J_2/J_1 from 0 to 1 in steps of 0.01.

3.3 Principal Component Analysis

In the PCA method, correlated data or features in a basis are rotated to a new basis which is a linear combination of the original basis while preserving all variation in the data [194, 195]. In the new rotated basis, most of the variations in data are confined to only a few dimensions and other dimensions are irrelevant. For the determination of these important dimensions, we need the co-variance matrix of data sets of measurement. The covariance matrix C_T can be defined as

$$C_T = XX^T \tag{3.5}$$

where X is a set of measurements with zero empirical means and it is a rectangular matrix. X^T is transpose of X. We construct a data matrix Y from which one can get the data-centered matrix X. Each row of Y represents all measurements of a particular type, whereas the column represents a set of measurements from one particular trial. In this case, Y have L dimensional features and $N_{J_2/J_1} = M \times m$ dimensional samples. Where m is the number of configurations for each J_2/J_1 and M is the number of equally spaced sets of J_2/J_1 for $0 < J_2/J_1 < 1$. The data-centered matrix X is formed by calculating the deviation of the components at each site of Y. For each site i its mean μ_i is calculated by taking an average over all samples and it is defined by $\mu_i = \frac{1}{N_{J_2/J_1}} \sum_{k=1}^{N_{J_2/J_1}} Y_{i,k}$. The deviation of the

spin component for the k^{th} sample at i^{th} site can be written as $X_{i,k} = Y_{i,k} - \mu_i$. We write down the matrix elements of the covariance matrix as

$$C_T(i,j) = \sum_{k=1}^{N_{J_2/J_1}} X_{i,k} X_{k,j}^T. \tag{3.6}$$

$X_{k,j}^T$ is the transpose of $X_{j,k}$.

In thermal phase transition calculations, spin configuration at a particular temperature is a snapshot of a Monte-Carlo step [197–199]. To study the quantum phase transition, our first goal is to form the data matrix Y. In quantum phase transition, we deal with the wave function it is defined as

$$|\psi\rangle = \sum_{k'=1}^{m} C_{k'} |\phi_{k'}\rangle \tag{3.7}$$

where $|\phi_{k'}\rangle \equiv |\uparrow\downarrow\uparrow\downarrow\downarrow ...\rangle$ is an arbitrary spin configuration. The configurations $|\phi_{k'}\rangle$ are represented in S^z basis and each configuration has information of S^z component of each site and it can take the values either of ± 0.5. $C_{k'}$ is amplitude and $C_{k'}^2$ is the probability or weight factor of $|\phi_{k'}\rangle$ in the wave function as shown in Eq. 3.7. We consider only a few MPSCs with larger relative weights, which are defined by

$$\gamma_{k'} = \frac{C_{k'}^2}{Max[C_1^2, ..., C_{N_H}^2]} \tag{3.8}$$

N_H is the dimension of the truncated Hilbert's space using IVM with $\Delta e_l \leq 1\%$. The largest value of $\gamma_{k'}$ is unity and subsequent relative weight decreases as probability decreases. In our present study, we consider first m fixed number of most probable spin configuration $|\phi_{k'}\rangle$ for each value of J_2/J_1 and now $L \times N_{J_2/J_1}$ dimensional matrix X is constructed. For a system size L, C_T have dimension of $L \times L$ and there are L eigenvalues $[\lambda_{\mathbf{1}}, ..., \lambda_{\mathbf{L}}]$ and its corresponding eigen vectors or weight vectors $[\mathbf{w_1}, ..., \mathbf{w_L}]$ after diagonalisation. In general, one can write,

$$\mathbf{X X^T w_n} = \lambda_n \mathbf{w_n} \tag{3.9}$$

where, each eigenvector w_n is a column vector with L rows. The variance of the data set for various J_2/J_1 is maximum corresponds to the largest eigenvalue λ_1 and it is second maximum for the second largest eigenvalue λ_2 and so on. Using such dimensionality reduction procedure, we find only a few large eigenvalues and corresponding eigenvectors are important to accommodate most of the variation in the original data sets.

By projecting the original data along n^{th} eigenvector w_n, we get N_{J_2/J_1} number of principal components. The n^{th} principal component $p_n(J_2/J_1, k)$ corresponds to the k^{th} sample can be obtained by

$$p_n(J_2/J_1, k) = w_n^T Y(k) \tag{3.10}$$

here, $Y(k)$ is the k^{th} sample with L entries of the data matrix Y. w_n^T is the transpose of the eigenvector w_n. The n^{th} 'quantified principal component' is calculated by summing the absolute value of the principal components over the samples (m) for a particular value of J_2/J_1 [197].

$$p_n(J_2/J_1) = \sum_{k=1}^{m} |p_n(J_2/J_1, k)| \tag{3.11}$$

In this manuscript, we focus on the PCA of the GS and the FES for different J_2/J_1 and calculate the eigenvalues and the corresponding eigenvectors of the covariance matrix C_T. We calculate principal components corresponding to the largest eigenvalues. We note that in our study, the first eigenvalue is the largest as compared to the others and so the 'quantified principal component' $p_1(J_2/J_1)$ can determine the phase transition, and our calculations also suggest that the principal components of the FES are more important in determining the quantum phase transition.

3.4 Results

In this section, we first discuss the quantum phase transition and phase boundary of the $J_1 - J_2$ model in the literature, and thereafter, we apply an unsupervised machine learning method to evaluate the quantum phase boundary and degeneracies in this model. The quantum phase transitions of the $J_1 - J_2$ model for a spin-1/2 have been extensively studied by using different analytical and numerical techniques [96, 203, 204]. In small J_2/J_1 limit, the GS exhibits the GSL phase which is characterized by algebraic decay of spin correlation function and gapless spectrum [206–208]. This phase extends up to J_2/J_1=0.2411, and thereafter, a gapped phase sets in the GS, and spin correlations are short range or exponentially decaying [206–208]. In this phase, the system shows dimerized GS and finite E_{ST}. E_{ST} and the nature of the spin correlation function can be used to determine the phase boundary in the thermodynamic limit [96, 99, 204]. In a finite system, the crossover point of the FES of the singlet and the lowest state of the triplet is the phase boundary of the GSL and the dimer phase [96].

Now let us apply an unsupervised machine learning technique PCA to determine the phase boundary and signature of degeneracies in the GS. We pointed out in section 3.3 that the eigenvalues and the eigenvectors of C_T are important to decide the rotation of the basis along which the maximum of the variation is preserved. Only a few largest eigenvalues and their eigenvectors are important to determine relevant principal components. In the rotated basis, n^{th} principal component corresponds to the k^{th} sample $p_n(J_2/J_1, k)$ can be obtained from Eq. 3.10 and the 'quantified principal component' $p_n(J_2/J_1)$ from Eq. 3.11. We calculate the 'quantified principal component' $p_1(J_2/J_1)$ of the GS and the FES in $S^z = 0$ sector to characterize the phase boundary of this model. The data centered-matrix X is calculated using the MPSC approach as described in section 3.3.

The eigenvalues of C_T are analyzed and the effect of MPSC m and the effect of finite size L on principal components is studied in detail. The phase boundary and the degeneracies are studied with the help of 'quantified principal component'

$p_1(J_2/J_1)$ corresponding to the largest eigenvalue λ_1. In all our calculations, we have taken $M = 100$ sets of J_2/J_1 in the range $0 < J_2/J_1 < 1$ with step 0.01.

3.4.1 Effect of L and m on λ_n

For the finite-size system study, the finite-size effect is important to see and so is its applicability in the thermodynamic limit. In this section, we first discuss the finite size scaling and its impact on the principal components. The eigenvalues λ_n of the covariance matrix for the GS and the FES are shown in Fig. 3.2 for three different system sizes $L = 16$, 20 and 24 for $m = 25$. For fixed $m = 25$, λ_n of the GS and FES decrease rapidly as shown in Fig. 3.2(a) and 3.2(b) respectively. In both cases, the first eigenvalue is dominating over others and increases with system size for both GS and FES. Therefore, we choose the first eigenvalue and

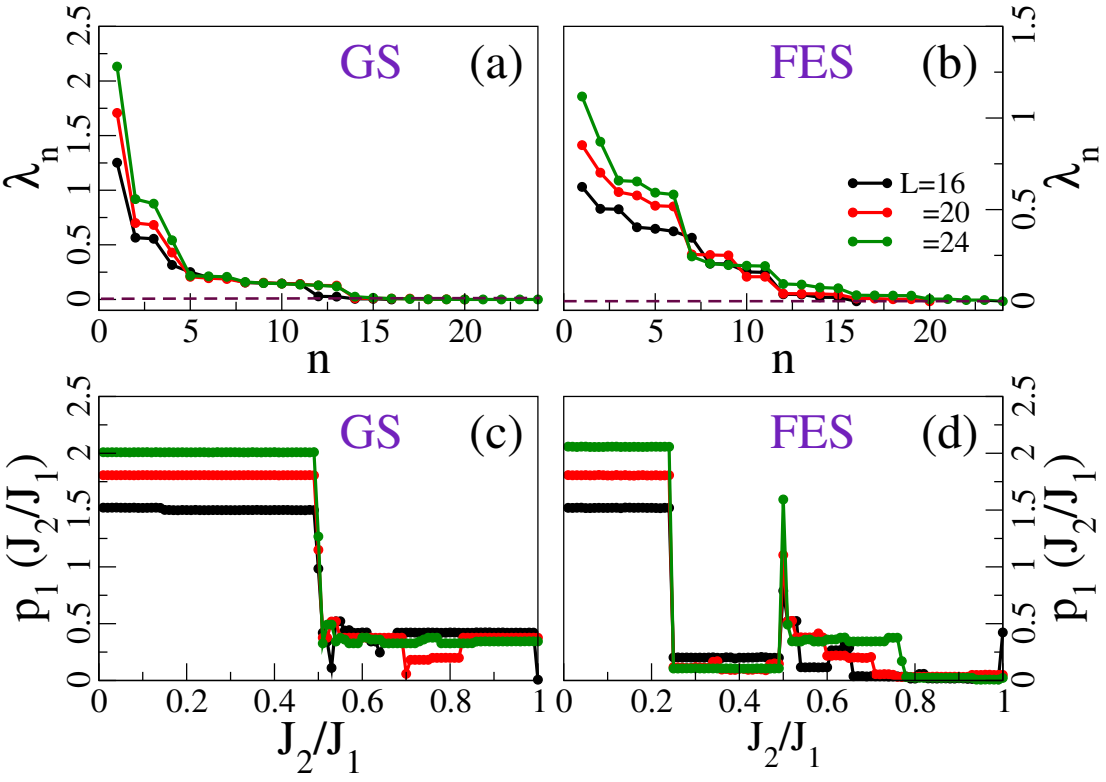

FIGURE 3.2: (color online) Finite size effect on 'quantified principal component' $p_1(J_2/J_1)$ is shown for $m = 25$. Eigenvalues of the co-variance matrix are shown for (a) the GS and (b) the FES. 'quantified principal component' $p_1(J_2/J_1)$ are shown for (c) the GS and (d) the FES. Black, red, and green colors represent different system sizes $L = 16, 20$, and 24 respectively.

its corresponding 'quantified principal component' $p_1(J_2/J_1)$. In Fig. 3.2(c) and 3.2(d), we plot $p_1(J_2/J_1)$ for the GS and the FES respectively as a function of J_2/J_1 for three different system sizes L. We observe $p_1(J_2/J_1)$ is constant and suddenly drops at $J_2/J_1 = 0.5$ (MG point) for GS. However, for the FES, we notice a drop at $J_2/J_1 = 0.241$ and thereafter it is constant up to $J_2/J_1 = 0.5$ for all values of L. The first jump in the $p_1(J_2/J_1)$ of the GS is due to degeneracy in the state at $J_2/J_1 = 0.5$, whereas $p_1(J_2/J_1)$ of FES has first degeneracy at 0.241 due to energy level crossing and second jump may be the consequence of degeneracies. We also notice a few more in between $0.5 \leq J_2/J_1 \leq 1.0$. In GS, the jumps are observed for $0.55 < J_2/J_1 < 1.0$ for the system sizes $L = 16$, and 24 respectively. However, in the case of the FES, we notice two jumps for all the system sizes. The values of $p_1(J_2/J_1)$ below $J_2/J_1 < 0.5$ increases with L, whereas it decreases with L for $J_2/J_1 > 0.5$. The principal component of the GS has the first jump at $J_2/J_1 = 0.5$ due to the GS degeneracy, whereas the principal component of the FES attains the first jump near $J_2/J_1 = 0.241$ due to energy level crossing, and the second jump at $J_2/J_1 = 0.5$ due to the degeneracy. The other jumps above $J_2/J_1 > 0.5$ are due to the incommensurate behavior. These results are compared with energy level crossing in Sec.3.4.2.

The number of MPSC plays a crucial role in giving the accurate wave function and so it is necessary to study the dependence of the number of significant MPSC m on the principal components. Now we analyze the dependence of λ_n and $p_1(J_2/J_1)$ on the number of samples m for both the GS and the FES. Four different values $m = 10$, 25, 50 and 100 are considered as shown in Fig. 3.3 for $L = 24$. λ_n and their variation in both the GS and FES decreases with m as shown in Fig. 3.3(a) and 3.3(b) respectively. MPSCs are governed by the Hamiltonian, and increasing the m increases the chance of inclusion of even less probable configurations which hardly contributes to the phase transition. Only the first 'quantified principal component' $p_1(J_2/J_1)$ is important in both the GS and the FES. In Fig. 3.3(c) and 3.3(d), $p_1(J_2/J_1)$ as a function of J_2/J_1 is plotted for the GS and FES respectively for four values of m. The expected jumps and fluctuations in $p_1(J_2/J_1)$ get suppressed

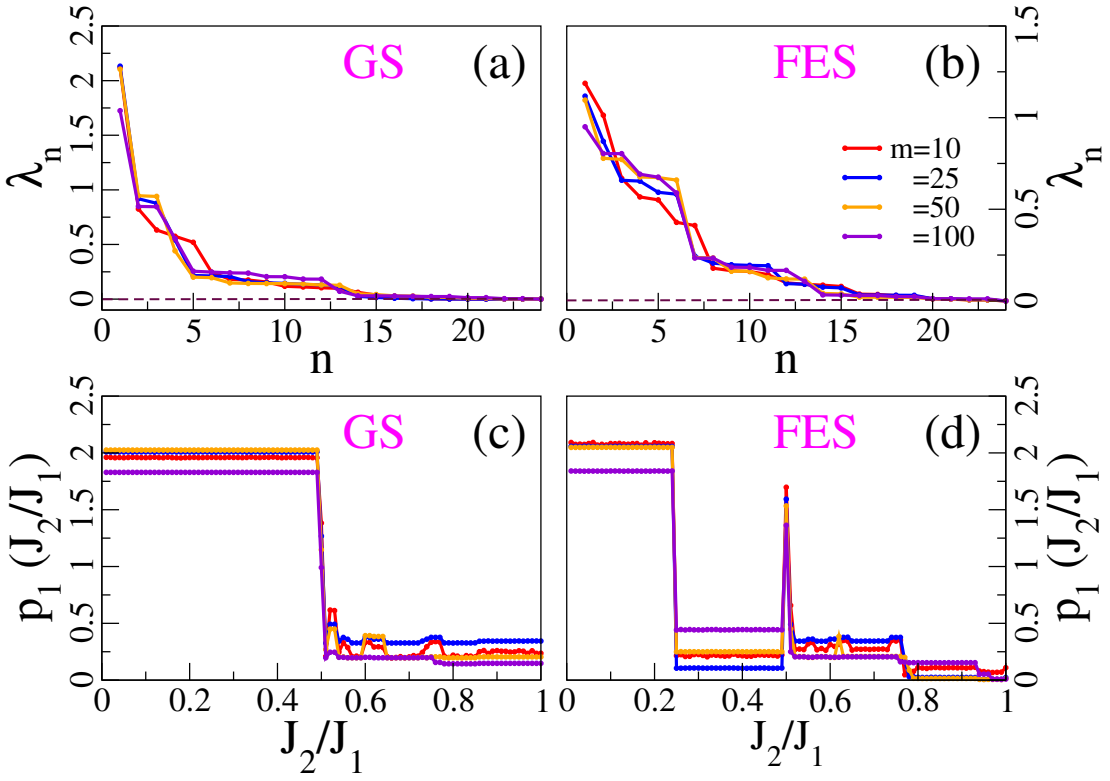

FIGURE 3.3: (color online) PCA dependence on MPSC (m) taken for the data matrix for $L = 24$ is shown. Eigenvalues of the co-variance matrix are shown for (a) the GS and (b) the FES and 'quantified principal component' $p_1(J_2/J_1)$ are shown for (c) the GS and (d) the FES. Red, blue, orange, and indigo colors correspond to $m = 10$, 25, 50, and 100 respectively.

with increasing m, but their nature is quite similar for all values of m. We present all the results for $m = 25$ hereafter.

3.4.2 Principal components and quantum phase transition

In this work, we are dealing with the finite system size $L = 24$, therefore let us try to compare the $p_1(J_2/J_1)$ curve with $E_{ST} - E_\sigma$ curve as a function of J_2/J_1. In Fig. 3.4(a), $E_{ST} - E_\sigma$ curve is plotted as a function of J_2/J_1, there is a crossing of E_{ST} and E_σ curve at $J_2/J_1 \approx 0.241$ and this crossing indicates the GSL-Dimer phase boundary for $L = 24$. At $J_2/J_1 = 0.5$ or MG point and 0.55, 0.62, 0.755, the E_σ is zero i.e., the ground state is doubly degenerate as shown in Fig. 3.4(a). The degeneracies are marked with circles. In Fig. 3.4(b), $p_1(J_2/J_1)$ vs J_2/J_1 for the GS, exhibits a large jump at $J_2/J_1 = 0.5$ and kinks at 0.52, 0.745, however, near

to the MG point, fluctuations in $p_1(J_2/J_1)$ curve indicate degeneracies or nearly degenerate states. The GS $p_1(J_2/J_1)$ does not show any kink near 0.62. The $p_1(J_2/J_1)$ of the FES vs J_2/J_1 exhibits a large jump at $J_2/J_1 \approx 0.241$, jump at MG point and kinks at $J_2/J_1 = 0.52, 0.63, 0.745$. It is well known that degeneracies at 0.55, 0.62, and 0.755 are due to incommensurate phases i.e., two singlet states become degenerate at these points [205]. Therefore, we can conclude that by studying the 'quantified principal component' $p_1(J_2/J_1)$ of the GS and FES, one can extract the degeneracies in the GS, however, analysis of the $p_1(J_2/J_1)$ of the FES can reliably give phase boundary of the GSL-dimer phase transition and these results are consistent with results in the literature [96, 205–207].

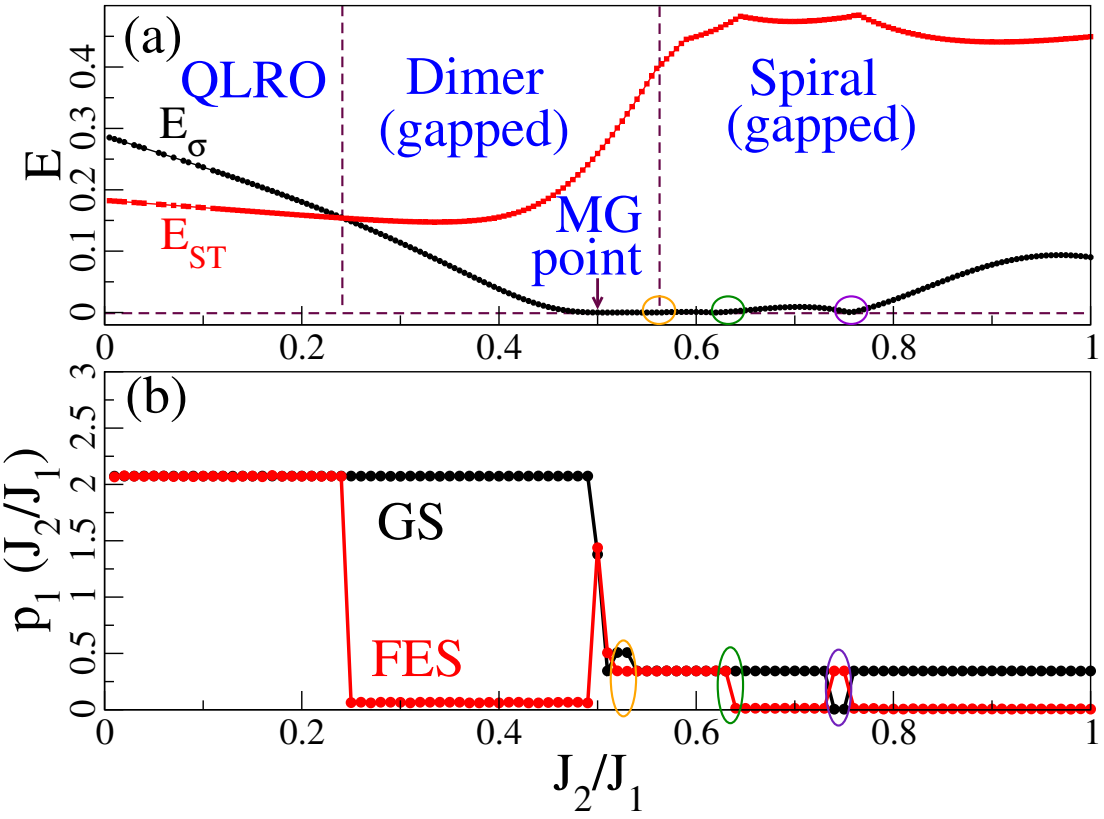

FIGURE 3.4: (color online) For $L = 24$ (a) Energy gaps vs J_2/J_1 is plotted. The black curve is the first excited state energy gap (E_σ) defined in Eq. 3.4 and the red curve is the lowest triplet gap (E_{ST}) defined in Eq. 3.3. (b) 'quantified principal component' $p_1(J_2/J_1)$ is shown as a function of J_2/J_1. Black and red curves represent $p_1(J_2/J_1)$ calculated from the GS and the FES respectively.

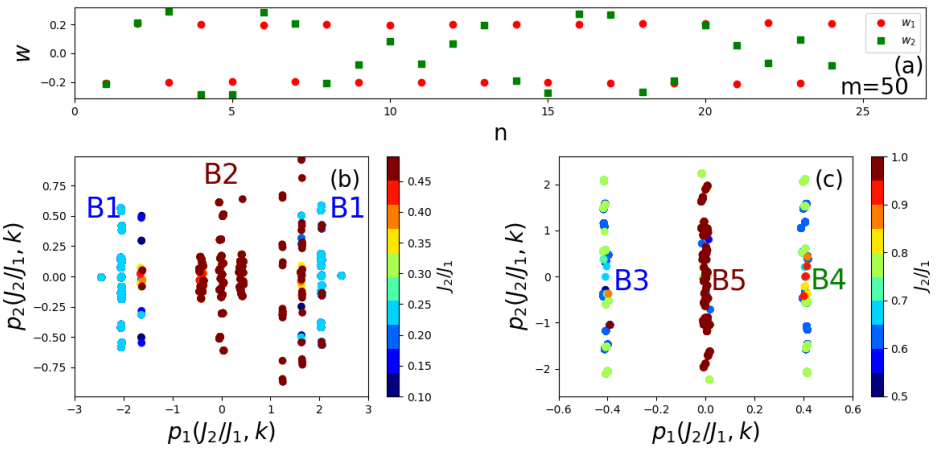

FIGURE 3.5: (color online) For $L = 24$, $m = 50$: (a) eigen vectors $\mathbf{w_1}$ and $\mathbf{w_2}$ corresponding to largest and second largest eigenvalues of C_T are plotted as a function of site n. (b) Scatter plot of $p_1(J_2/J_1)$ vs $p_2(J_2/J_1)$ for the limit $0.1 < J_2/J_1 < 0.5$. The color bands B1 (sky blue) and B2 (maroon) are separated at $J_2/J_1 \approx 0.241$. (c) Scatter plot of $p_1(J_2/J_1)$ vs $p_2(J_2/J_1)$ for the limit $0.5 < J_2/J_1 < 1.0$. The color bands B3 (blue), B4 (green) are separated around $J_2/J_1 = 0.63$ and B4, B5 (maroon) are separated at $J_2/J_1 = 0.745$.

3.4.3 Principal components and eigenvectors of C_T

For a more detailed understanding of the QPTs, we discuss the principal components and eigenvectors of the covariance matrix C_T in this section. The elements of the covariance matrix can be assumed to be the product of the z component of the spin densities at two sites which is averaged over the parameter and configuration space as described in Eq.3.6. Similarly, the n^{th} eigenvector of the matrix can be mapped as $w_n = \sum_{i=1}^{L} w_{n,i}|b_i^z\rangle$. Here, $|b_i^z\rangle$ may be thought as the z component of spin density basis at site i and $w_{n,i}$ may be mapped as the amplitude of average density at site i corresponds to n^{th} eigenvalue λ_n of the covariance matrix. From the previous discussion, it is noticed that the FES is sufficient to give all the phase transitions in the regime $0 < J_2/J_1 < 1$. The covariance matrix C_T is calculated from the FES wave function for $0 < J_2/J_1 < 1$ and first two eigenvalues λ_1 and λ_2 of C_T have significantly larger variances as compared to the other eigenvalues. The eigenvectors w_1 and w_2 corresponding to λ_1 and λ_2 are plotted in Fig. 3.5(a), and we notice that w_1 is a periodic function with pitch angle π where w_2 is a periodic function with pitch angle $\pi/6$. The π phase difference in w_1 corresponds

to the antiferromagnetic arrangement of spin density, whereas, the arrangement is spiral in nature for w_2 which corresponds to spiral spin density behavior. Now, $p_1(J_2/J_1, k)$ and $p_2(J_2/J_1, k)$ can be constructed by rotating the original Y by these two weight vectors w_1 and w_2 by using expression Eq. 3.10. The scatter color plot of $p_1(J_2/J_1, k)$ and $p_2(J_2/J_1, k)$ is shown in Fig. 3.5 (b) and 3.5(c), and the color intensity bar indicates the strength of J_2/J_1. The $p_1(J_2/J_1, k)$ and $p_2(J_2/J_1, k)$ are plotted for $0.1 < J_2/J_1 < 0.5$ in Fig. 3.5(b), which form two kinds of bands B1 and B2. The principal components form band B1 in the range $0.1 \leq J_2/J_1 \leq 0.241$ and this band is located at $p_1(J_2/J_1, k) \approx \pm 2.0$. For $0.241 \leq J_2/J_1 \leq 0.5$, principal components form the B2 band around $p_1(J_2/J_1, k) = 0$, and a clear separation of data can be seen around $J_2/J_1 = 0.241$. Both the bands B1, B2 are more spread along $p_1(J2/J1, k)$ with larger value than $p_2(J2/J1, k)$, which favours the antiferromagnetic spin arrangement. With a larger value, ± 2 of $p_1(J2/J1, k)$ and thin band formation B1 designates the QLRO phase. Whereas, the band B2 shows more distribution of $p_1(J2/J1, k)$ and this process takes into the dimer gapped phase regime.

In Fig. 3.5(c), the scatter plot is shown for $0.5 < J_2/J_1 < 1$, and the principal components form three color bands. These bands B3, B4, B5 correspond to the limits $0.5 \leq J_2/J_1 \leq 0.63$, $0.63 \leq J_2/J_1 \leq 0.745$ and $0.745 \leq J_2/J_1 \leq 1.0$ respectively. These bands correspond to different pitch angles in the system in the spiral phase. The band B3 are located at $p_1(J_2/J_1, k) \approx \pm 0.4$ and represented with blue color, B4 is symmetrically located at $|p_1(J_2/J_1, k)| \approx 0$ and $|p_1(J_2/J_1, k)| \approx 0.4$. The major fraction of the components of B4 reside at $|p_1(J_2/J_1, k)| \approx 0$ rather $|p_1(J_2/J_1, k)| \approx 0.4$ and so the average of it gives finite but near equal to zero value of $|p_1(J_2/J_1, k)|$ as shown in Fig. 3.4(b). The band B5 is located along $|p_1(J_2/J_1, k)| \approx 0$ and it gives the average $|p_1(J_2/J_1, k)| = 0$ as shown in Fig. 3.4(b). The larger value of $p_2(J_2/J_1, k)$ as compared to $p_1(J_2/J_1, k)$ signifies that the second principal component is dominating for the bands B3, B4, and B5. In other words, these bands support the spiral behavior more and represent the spiral regime.

3.5 Summary

The main focus of the manuscript is an application of the unsupervised ML using the PCA method to study the quantum phases of the $J_1 - J_2$ model in Eq.3.1. We also developed an approximate method IVM which requires a very small number of basis states to get the accurate GS energy. For $L = 16, 20, 24$, only $63\%, 42\%$ and 32% of full basis is required to get the accuracy up to 99% of the exact energy. We note that the percentage of basis required decreases with system size. Therefore, the computational cost of eigenvalue and eigenvector calculation increases only with $N^{\frac{3}{2}}$, where N is the number of the required basis for accurate calculation.

We show that the nature of the 'quantified principal component' $p_1(J_2/J_1)$ weakly depends on the variation of m and the sensitivity is shown for $m = 10$, 25, 50, and 100 in Fig. 3.3. The nature of $p_1(J_2/J_1)$ of the FES also does not change with system size and its variation at the boundary gets enhanced with increasing L. The jumps and kinks in $p_1(J_2/J_1)$ can give an accurate determination of phase boundary and degeneracies in the GS. The PCA of the GS can predict some of the degeneracies in the GS. However, $p_1(J_2/J_1)$ of the FES exhibits jumps at $J_2/J_1 = 0.241$ and this jump represents the GSL-dimer phase boundary and this phase boundary is consistent with calculation on E_{ST} in the thermodynamic limit [203] and using level crossing method for finite system size [96]. In this method, we require only a few MPSCs for a given value of $\frac{J_2}{J_1}$ to study the quantum phase transitions of the $J_1 - J_2$ model. The MPSC is calculated for both the GS and the FES of this model and shows that this approach works very well for the frustrated 1D $J_1 - J_2$ spin-1/2 model and it gives accurate phase boundary, whereas other methods like quantum Monte-Carlo fail to determine the quantum phase boundary for frustrated or away from the half-filled fermionic system due to sign problem. This method requires only small numbers of MPSC from the FES to calculate the 'quantified principal component' $p_1(J_2/J_1)$ which shows kink or jump at the phase transition points. The kinks at $J_2/J_1 = 0.52, 0.63, 0.745$ for $L = 24$ represent the degeneracies in the GS and these are consistent with literature [205].

PCA study needs two states- the GS and the FES to calculate but only the FES is sufficient for the small system sizes to analyze the quantum phase transition as compared to the level crossing study where, three states- the GS, fit excited state and lowest triplet state calculations are required. In conclusion, a combined method of IVM and unsupervised machine learning method PCA gives reliable phase boundaries of frustrated spin-1/2 $J_1 - J_2$ models, and this method may be an alternative tool to explore the quantum phase transition in other frustrated systems.

Chapter 4

Quantum phase transition of a spin-1/2 XXZ model using Principal component analysis

4.1 Introduction

In the spin model systems, anisotropy in the exchange interaction is an important parameter that may be tuned to get many exotic phases. The XXZ Heisenberg spin model is one of the simplest spin model systems with two types of exchange interactions: z-component of exchange Δ and J along x or y direction [103, 209]. The Δ/J is a tuning parameter that leads to various exotic quantum phases in the ground state of this model. In the different limit of the exchange Δ parameter, this model turns into XY model for $\Delta < 1$, isotropic Heisenberg model for $\Delta = 1$, and Ising model for $\Delta \to \infty$ [104]. The spin-1/2 isotropic Heisenberg model possesses the SU(2) symmetry, whereas, the spin-1/2 XY model favors the planar ordering which follows O(2) ordering [210, 211]. In the spin-1/2 XXZ model with $\Delta > 1$, the system has U(1) symmetry in the absence of the magnetic field [210, 211]. For $\Delta \to \infty$, it turns out to be the Ising model with protected Z_2 symmetry []. The XXZ model can be tuned from Ising to XY model and the ground state of the

system adiabatically undergoes the symmetry change from 0(2) to U(1) by Δ from 0 to ∞. The quantum phase transition from the XY to the Ising phase is of infinite order and it takes place at $\Delta = 1$ [103, 104, 212]. This type of phase transition is called the Kosterlitz Thouless (KT) transition [213]. The KT transition is well studied in the case of the classical XXZ model for two or higher dimensions i.e., $d \geq 2$ []. The one-dimensional (1D) quantum spin-1/2 XXZ model is equivalent to the two-dimensional classical XXZ model [126, 214]. However, the exact ground state of the quantum 1D model Hamiltonian is quite different from that of the classical two-dimensional model system and the KT transition point is still under debate.

There has been an enormous amount of studies on the spin-1/2 XXZ model with the nearest neighbor exchange interaction and Δ as a tuning parameter. For a one-dimensional lattice, this model exhibits doubly degenerate FM GS with protected reflection symmetry ($S^z \rightarrow -S^z$) $\Delta < -1$ [103, 211]. The critical regime (CR) or the XY phase emerges in the ground state for $-1 < \Delta < 1$ [103, 109], and the spectrum is gapless in this parameter regime. In the thermodynamic limit for $\Delta > 1$, the system exhibits the antiferromagnetic phase with quasi-long range ordering [215]. The transition from the highly degenerate CR phase to the antiferromagnetic phase is reported as an infinite-order KT transition [215]. . [102] et al. report by studying up to the system size $L = 100$ that the finite size effect of the critical value for KT transition parameter Δ_{KT} resides between 1 and 1.4.

The many-body nature of this model makes the exact solution of this model intractable. Many approximate but highly accurate numerical methods are employed to study this model on various geometries, but ground state properties are still under debate [].

In this work, we study the quantum spin-1/2 anisotropic XXZ model Hamiltonian on a chain and determine the phase boundaries. We show that by proper choice of the spin configurations as inputs to the unsupervised machine learning method PCA, the FM-XY and KT transitions can be captured and analyzed successfully in terms of the principal components.

4.2 Model Hamiltonian of the spin-1/2 XXZ model and KT transition

The Hamiltonian for the spin-1/2 XXZ model on the one-dimensional lattice can be written as

$$H = J\sum_i (S_i^x S_{i+1}^x + S_i^y S_{i+1}^y + \Delta S_i^z S_{i+1}^z), \tag{4.1}$$

where J is the exchange coupling strength and Δ is the axial anisotropy parameter. S_i^z, S_i^x, S_i^y are three spin components along x, y, and z directions respectively at site i. This model Hamiltonian can be written alternatively in terms of the spin operators as

$$H = \sum_i \frac{1}{2}(S_i^+ S_{i+1}^- + S_i^- S_{i+1}^+) + \Delta \sum_i S_i^z S_{i+1}^z, \tag{4.2}$$

J sets the energy scale and it is chosen to be 1. The S^+, and S^- are the raising and lowering operators respectively which can be written as $S^+ = S^x + iS^y$ and $S^- = S^x - iS^y$ respectively.

In the thermodynamic limit, the ground-state of this model Hamiltonian undergoes two phase transitions while tuning the axial anisotropy parameter Δ as pointed out earlier. The ferromagnetic (FM) to XY phase transition takes place at $\Delta = -1$ and this quantum critical point is independent of the finite-size effect. The axial component of magnetization is an order parameter for this phase and it can be defined as $m^z = \frac{1}{L}\sum_i S_i^z$. The sharp jump of the order parameter from unity to zero is a clear indication of a first-order phase transition. The next phase transition for this model Hamiltonian takes place for $\Delta > 1$ (for the thermodynamic limit) where the system goes from the XY phase to the antiferromagnetic phase. The most striking key here is that this critical point is sensitive to system size L and the order of the phase transition is infinite and can be described in terms of the theory of KT transition.

The order parameter in the antiferromagnetic phase is staggered magnetization which can be defined as $m_s^z = \frac{1}{L}\sum_i (-1)^i S_i^z$. This order parameter is finite in the AFM phase whereas it decays out and vanishes in the XY phase []. The m_s value for the XY phase varies from 0 to 1 by breaking the continuous symmetry, this phase transition is special due to continuous broken symmetry in the system. The m_s^z changes adiabatically to the maximum which is 1 while tuning the axial anisotropy Δ. This is due to the protected U(1) or circular symmetry in the XY phase which is ruined by the transverse fluctuation J in the above Hamiltonian 4.2. This phase transition description is in good agreement with the KT transition [101]. Although the KT transition was first proposed for the XY phase in a 2-dimensional classical system, one may wonder if it violates the well-established Mermin-Wagner theory. But it should also be noted that the 1-dimensional XXZ model can be mapped to its classical analogous model of 2-dimension. The antiferromagnetic phase for $\Delta > 1$ is a superposition of the antiferromagnetically aligned spin configurations.

We focus on detecting the quantum critical points $\Delta = -1, 1$ using the unsupervised machine learning method principal component analysis (PCA). Before going to the result section, let us discuss the data preparation.

4.3 Data matrix preparation

The Principal Component Analysis (PCA) works on the principle of finding out the distinguishable patterns from a given data set, and this method calculates the variances among the data for a given data matrix. The maximum variance directions are found by forming a covariance matrix C^T as discussed in Chapter 2. The C^T is formed as $C^T = X^T X$, where X is a data-centred matrix of the initial data matrix Y and X^T is the transpose matrix of X. The X can be obtained by subtracting each column of Y from its column mean as discussed in Chapter 2. The eigenvectors corresponding to the first few of the eigenvalues of C^T represent the eigenvectors or the weight vectors of the covariance matrix. The projection

of the initial data set towards these eigenvectors gives the first few principal or major components. The eigenvalues, eigenvectors are usually written as $\lambda_1, \lambda_2, ...$ and $w_1, w_2, ...$ respectively [216]. The principal components are generally written as $p_1, p_2, ...$ etc.

The quantum phase transition between XY and the antiferromagnetic phase in the spin-1/2 XXZ model by tuning Δ is an adiabatic process, therefore, only the spin configurations would not be sufficient information for PCA unlike in $J_1 - J_2$ as done in Chapter 5 [216]. For this model, the spin configurations in the limit of $0 < \Delta < 1$, the coefficients, or the weights of these configurations of the approximate wavefunction in the ground state of the Hamiltonian are also used for data preparation. We know that each of the wavefunctions is a linear combination of all the spin configurations in Hilbert's space whereas the same wavefunction can be approximately written as a linear combination of only a few of the contributing configurations which in this case we call to be MPSC. The other configurations are ignored because it is assumed that corresponding to these, the similar kind of configurations for the thermodynamic limit goes to zero. These MPSCs are obtained using an iterative variational method (IVM). The weight of the coefficients is defined as the square of each of the configurations after diagonalization using IVM. The spin configurations multiplied by the weight are arranged along each row of the data matrix. Each column element of the data matrix is the z-component of spin at each site of the system. The further procedure is followed similarly as it is done in the case of the $J_1 - J_2$ model in [216].

4.4 Results

In this section, we first benchmark the phase boundaries by showing the energy gap ΔE and its finite-size scaling behavior. Thereafter, we show how the principal components can determine these phase boundaries accurately.

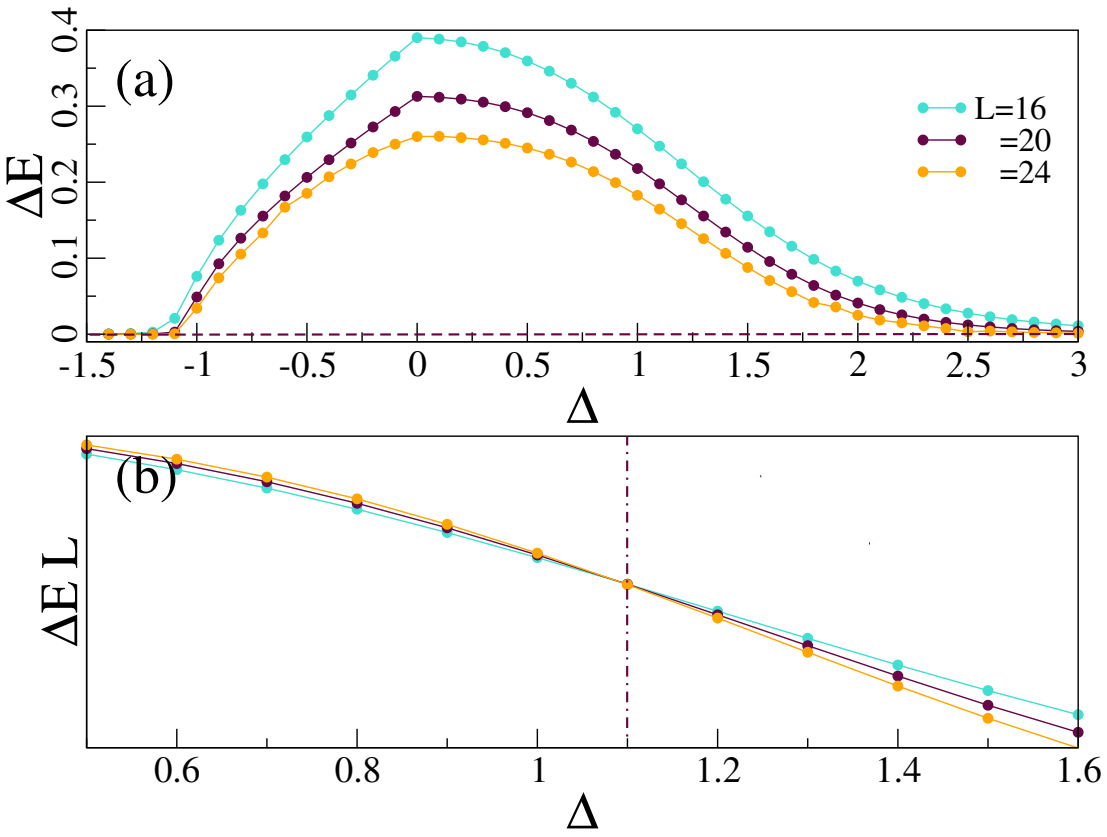

FIGURE 4.1: (color online) (a) Energy ΔE is shown as a function of the axial anisotropy Δ for the system sizes $L = 16, 20, 24$. (b) The rescaled energy gap ΔEL is shown as a function of Δ for the same set of system sizes $L = 16, 20, 24$.

4.4.1 Energy gap as a function of Δ

In Fig.4.1. (a), we show the energy gap E_{gap} between the first excited state and ground state in the $S^z = 0$ sector as a function of the axial anisotropy parameter Δ. The energy gap is calculated using the exact diagonalization method. It is noticed that for three different system sizes $L = 16, 20, 24$. the gap in Fig.4.1.(a) is zero below $\Delta = -1$. The vanishing gap in the $S^z = 0$ sector is a signature of the degeneracy in the system. This is well known because of the ferromagnetic ground state. However, our main focus is to identify the KT transition point around $\Delta = 1$. We show the energy gap to identify the KT point by varying Δ for the limit $0 < \Delta < 3$. Fig.4.1. (a) shows that for all system sizes $L = 16, 20, 24$, the gap ΔE initially increases to reach a maxima at $\Delta = 0$ and then it starts decreasing thereafter. It is also noticed that the gap decreases with system size for this parameter range. The continuous variation in the gap supports the critical

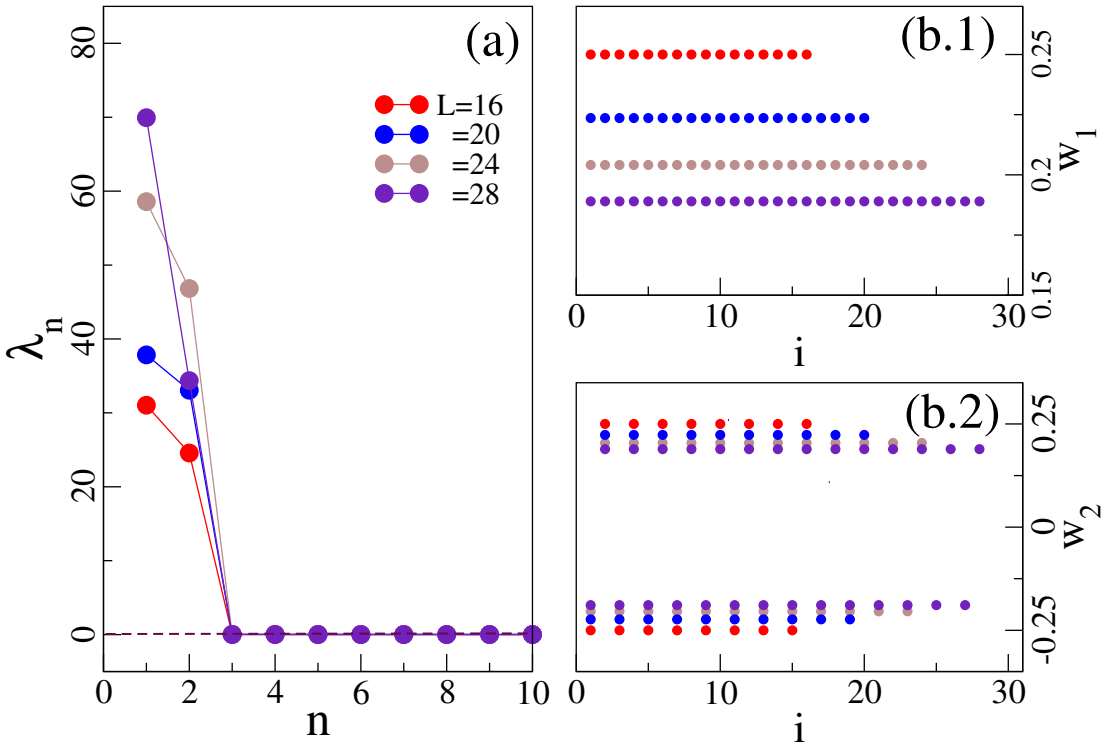

FIGURE 4.2: (color online) (a) Eigenvalues of the covariance matrix are shown as a function of the component index n. Red, blue, brown, and indigo colors are for system sizes $L = 16, 20, 24, and 28$ respectively. Two eigenvectors (b.1) w_1 and (b.2) w_2 of the covariance matrix for the system sizes $L = 16, 20, 24, 28$ are shown.

ordering in the XY phase which adiabatically goes to zero for higher Δ. So, the gap calculation for the finite system sizes is inadequate to characterize the phase boundary. In Fig.4.1. (b), we show the finite size scaling of the energy gap by multiplying the system size L. It is found that ΔEL for different system sizes crosses around a critical point. This critical point is $\Delta = 1.1$ for $L = 16, 20$ and 1.08 for $L = 20, 24$. The trend seems to be converged around $\Delta = 1.0$ for the thermodynamic limit. These crossover points separate all the ΔEL in two regimes with different behavior. All of the ΔEL curves overlap below the critical point and spread out above it. This critical point represents the boundary between the infinite order XY phase and the antiferromagnetic phase.

4.4.2 Eigenvalues and eigenvectors of the covariance matrix

The diagonalization of a $L \times L$ dimensional covariance matrix for the system size L gives the eigenvalues $\lambda_1, \lambda_2, ..., \lambda_L$ and eigenvectors $w_1, w_2, ..., w_L$. The eigenvalues $\lambda_1, \lambda_2, ..., \lambda_L$ in decreasing order are the measurement of the variances, whereas, the corresponding eigenvectors $w_1, w_2, ..., w_L$ are in various directions. It is to be mentioned that each of the elements in the covariance matrix is the z-component of spin at each site for the spin configurations chosen in the data set, each element of $w_1, w_2, ..., w_L$ represents the z-component of spin at each site along these eigenvectors. The constant value of w_1 implies the direction of the eigenvector to be a direct sum of the data elements at each site. The staggered pattern of w_2 corresponds to the staggered sum of the spin configurations.

Fig.4.2. (a) represents the eigenvalues of the covariance matrix for four different system sizes $L = 16, 20, 24, 28$. For all the system sizes, the covariance matrix has only two larger eigenvalues namely λ_1 and λ_2 which are significant. The eigenvectors w_1, w_2 corresponding to the first two eigenvalues λ_1, λ_2 are shown in Fig.4.2.(b).1 and Fig.4.2.(b).2 respectively. The w_1 is always constant for all the system sizes and it represents the ferromagnetic spin arrangement. It is noticed that the amplitude of w_1 can be written as $\frac{1}{\sqrt{L}}$. The w_2 shows a staggered pattern that supports the antiferromagnetic spin arrangement, where the amplitude of the vectors can be written as $\frac{1}{\sqrt{L}}$.

4.4.3 Principal components

The principal components can be obtained by projecting all the data elements of Y along the eigenvectors. All the principal components for the n^{th} eigenvector can be written as

$$pc_n = w_n^T Y, \tag{4.3}$$

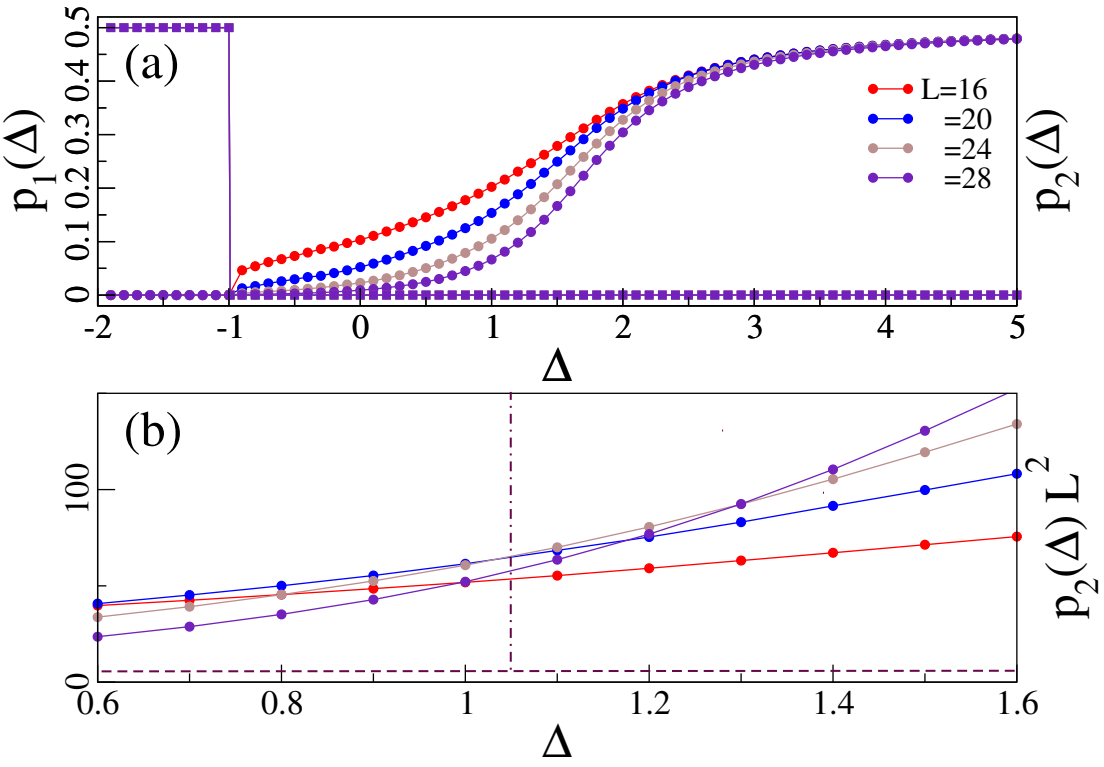

FIGURE 4.3: (color online)

w_n^T is the transpose of the eigenvector w_n.pc_n is a $1 \times M$ dimensional column vector corresponds to the n^{th} eigenvalue λ_n and eigenvector w_n. $M = m \times N$ rows of pc_n represent the projection of each of the configurations in the data set along w_n. These principal components with m configurations for N sets of tuning parameter Δ can be quantified as

$$p_n(\Delta) = \frac{1}{L} \sum_m pc_n, \tag{4.4}$$

$p_n(\Delta)$ is called the n^{th} 'quantified principal component'. $\frac{1}{L}$ gives the per-site measurement.

Since, the first two eigenvalues λ_1, λ_2 are significant in this work, we calculate the first two principal components $p_1(\Delta)$ and $p_2(\Delta)$. In Fig. 4.3.(a), $p_1(\Delta)$ and $p_2(\Delta)$ are shown as a function of the tuning parameter Δ in the range $-2 < \Delta < 5$ with a spacing 0.1 for the system sizes $L = 16, 20, 24, 28$. The spin configurations m for each Δ are taken to be 1000 always. The $p_1(\Delta)$ is a projection along the first eigenvector i.e., the scalar measurement of the ferromagnetic spin arrangement shows a jump at $\Delta = -1$. This jump is consistent with the energy gap ΔE

in Fig.4.1. (a) which is the phase boundary between the ferromagnetic and XY phases. The second 'quantified principal component' $p_2(\Delta)$ shows an adiabatic increase as a function of increasing Δ for all the system sizes. It indicates that the z-component of staggered magnetization prolifers with Δ. The maximum value of $p_2(\Delta)$ is 0.5 which is the value for a perfect antiferromagnetic spin arrangement. On the other hand, it is noticed that the $p_2(\Delta)$ decreases with system size L in the neighborhood of $\Delta = 0$. However, the proliferation of $p_2(\Delta)$ is continuous and it indicates the possibility of spontaneous symmetry breaking.

However, similarly, as done for the energy gap scaling, we further perform the finite size scaling for $p_2(\Delta)$. Because $p2_(\Delta)$ is per site value, we multiply it by L^2. The scaled function $p_2(\Delta)L^2$ is shown as a function of Δ in Fig. 4.3. (b) for the same set of system sizes L. The finite size scaling of $p_2(\Delta)$ shows a crossover of $p_2(\Delta)L^2$ function for all the system sizes at around $\Delta = 1.05$. This crossover point is the same as we found for the scaled energy gap. $\Delta = 1.05$ in this case represents the separation between two regimes for the thermodynamic limit. $p_2(\Delta)$ is vanishingly small for $\Delta < 1.05$, whereas, it is maximum i.e, 0.5 for $\Delta > 1.1$. These two regimes represent the XY and antiferromagnetic phases respectively.

4.5 Summary

In this manuscript, we have done feature engineering in preparing the data set for the spin-1/2 XXZ model. The samples or the row of the data matrix are featured by selecting the most probable spin configurations for any given value of Δ. The MPSCs are chosen systematically using an iterative diagonalization method. The eigenvectors of the covariance matrix show two kinds of spin arrangements. The first eigenvector w_1 associated with ferromagnetic ordering and its corresponding principal component $p_1(\Delta)$ shows a sharp jump at $\Delta = -1$ which indicates the FM-XY transition. The second eigenvector w_2 favors the antiferromagnetic spin arrangement and its corresponding principal component $p_2(\Delta)$ prolifers in between $\Delta = 0$ and $\Delta = 1$. The finite-size scaling helps in detecting the proliferation regime

and it finds that the XY-AFM or the KT transition takes place at $\Delta = 1.05$. In summary, with a proper data selection, we have successfully shown that the combined IVM-PCA method can help in finding both the conventional FM-XY and unconventional KT transition.

Chapter 5

Quantum Phases and Thermodynamics of a Frustrated spin-1/2 ladder with Alternate Ising-Heisenberg Rung Interactions

5.1 Introduction

The study of quantum phase transitions in low-dimensional spin systems has been a frontier area of research due to an abundance of effective low-dimensional magnetic materials [53, 144, 217–224] which exhibits a zoo of phases [95, 96, 99, 142, 145–148, 203, 206, 207, 225, 226]. The confinement and interplay of exchange interactions in low-dimensional systems like spin chains [220, 227, 228], spin ladders [53–55, 217] or two dimensional systems [229, 230] can give rise to various interesting ground state (GS) properties [203, 231–236]. Recently synthesized materials show that many of these spin-1/2 systems are frustrated even in one dimension (1D)

[221–224], whereas the low dimensional systems can be either geometrically frustrated i.e. antiferromagnet Heisenberg spin-1/2 on a triangular lattice [237, 238] or exchange interaction driven frustration such as 1D spin-1/2 system interacting with nearest neighbor interaction J_1 and antiferromagnetic next nearest neighbor exchange interaction J_2 [99, 142, 206–208, 239, 240]. Frustrated model Hamiltonians of one-dimensional systems and zigzag geometry [241, 242] are extensively studied theoretically and GS of these systems have exotic phases like spin liquid [53, 243], dimer [95, 96, 142, 203, 206, 207, 225, 226], spiral/non-collinear spin phase [96, 203, 244], ferromagnetic phase etc.

Spin chains and ladders can also have anisotropic exchange interactions [245–249] and some spin chains can have alternate Heisenberg and Ising exchange interactions [250], whereas exchange along the leg is Ising type. The Heisenberg-Ising model has been explored by few groups [98, 250–252]. The simplest model on a ladder geometry studied by Rojas et al. [250] with alternate anisotropic Heisenberg (J_x,J_x,J_z) and Ising type (J_0) rung exchanges and intra-leg exchange interaction (J_1) gives an interesting GS phase diagram with phases like frustrated phase 1 (FRU1), antiferromagnetic phase etc in large and small ratios of Ising to Heisenberg exchange interactions (J^z/J_1) limits respectively. This model also shows interesting sharp peaks in specific heat. Verkholyak et al. [98] studied an anisotropic model with Heisenberg rung exchange interaction (J_1) and Ising-type leg exchange interaction (J_2) and diagonal exchange interaction (J_3). They showed that GS can exhibit different phases e.g. stripe leg (SL), stripe rung (SR), Néel, and quantum paramagnetic (QPM) phases, etc. in the phase diagram of J_3-J_1 plane and the field dependence behavior in this model is also studied [98]. Other studies of the Heisenberg branched chain model show interesting GS behavior and plateau phase in the presence of an external magnetic field [253].

The thermodynamical properties of the one or quasi-one-dimensional quantum spin models with alternating isotropic and anisotropic units have been studied extensively recently [250, 254, 255]. In the presence of alternate Heisenberg and Ising rung and Ising leg interaction, the two consecutive units of the Hamiltonian become commuting and in such cases, the exact thermodynamical properties of

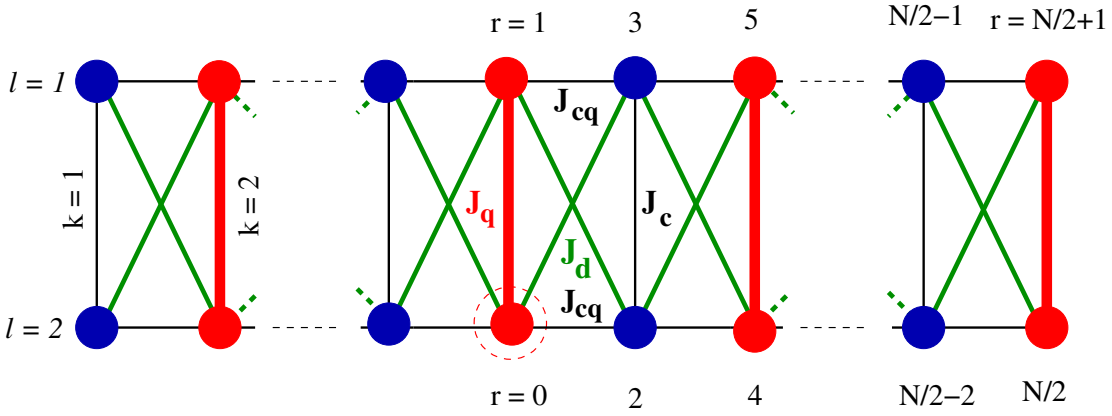

FIGURE 5.1: (Color online) Schematic model diagram for spin configurations of a 2-leg anisotropic spin ladder system with $N(=4n)$ sites is shown. The interactions along the odd and even rungs are Ising and Heisenberg types respectively. Both along the legs and diagonals, the interactions are Ising-type. The indices k $(1 \leq k \leq 2n)$ and l $(=1$ or $2)$ in the figure represent the rung and leg number; any spin in the anisotropic or isotropic rung is denoted by $\sigma_{k,l}$ or $S_{k,l}$ respectively. The variable r is the distance from the reference spin shown within a dotted circle.

these systems can be calculated using the transfer matrix method. For example, the susceptibility and other related quantities were calculated exactly for an anisotropic helical single-chain magnet Fe_2Nb using transfer matrix method [255].

In this paper, we study a general anisotropic Heisenberg-Ising model on ladder geometry with alternate Heisenberg and Ising exchange rung interactions, whereas the exchange interactions along the leg and the diagonal of the ladder are Ising type as shown in Fig. 5.1. The system exhibits anisotropic antiferromagnetic (AAFM), stripe rung ferromagnetic (SRFM), stripe rung ferromagnetic-edge (SRFM-E), and stripe leg ferromagnetic (SLFM) phases. The specific heat $C_v(T)$, magnetic susceptibility $\chi(T)$, entropy $S(T)$, and average energy $E(T)$ are studied in various phases.

This paper is divided into four sections and in section 6.2 we discuss the model Hamiltonian. In section 7.3 results are discussed and are divided into four subsections. We summarise all the results and conclude in the section 6.5.

5.2 Model Hamiltonian

We consider here a frustrated spin-1/2 ladder with alternating isotropic Heisenberg and Ising-type interactions. For convenience, the system is divided into two sublattices A and B. The A sublattice has Heisenberg rung interaction J_q while the B sublattice has Ising rung interaction J_c. The spins of two sublattices are connected by Ising-type interaction J_{cq} along the legs and also by diagonal Ising-type interaction J_d. Since for the B sublattice, only the z-component of spins appear in the Hamiltonian, we represent these spins by σ, whereas the other spins S have all three components. The schematic diagram of the spin model is shown in Fig. 5.1. The Hamiltonian for this system (having $4n$ sites) with open boundary condition (OBC) is given by $\mathbf{H} = \sum_{i=1}^{n-1} \mathbf{H_i} + \mathbf{H_e}$ where,

$$\begin{aligned}
\mathbf{H_i} &= J_q \vec{S}_{2i,1} \cdot \vec{S}_{2i,2} + \frac{J_c}{2}(\sigma_{2i-1,1}\sigma_{2i-1,2} + \sigma_{2i+1,1}\sigma_{2i+1,2}) \\
&+ J_{cq}\left\{S^z_{2i,1}(\sigma_{2i-1,1} + \sigma_{2i+1,1}) + S^z_{2i,2}(\sigma_{2i-1,2} + \sigma_{2i+1,2})\right\} \\
&+ J_d\left\{S^z_{2i,1}(\sigma_{2i-1,2} + \sigma_{2i+1,2}) + S^z_{2i,2}(\sigma_{2i-1,1} + \sigma_{2i+1,1})\right\} \\
&+ \frac{h}{2}\sum_{l=1}^{2}(2S^z_{2i,l} + \sigma_{2i-1,l} + \sigma_{2i+1,l}), \qquad (5.1) \\
\mathbf{H_e} &= \frac{J_c}{2}(\sigma_{1,1}\sigma_{1,2} + \sigma_{2n-1,1}\sigma_{2n-1,2}) + J_q \vec{S}_{2n,1} \cdot \vec{S}_{2n,2} \\
&+ J_{cq}\sum_{l=1}^{2} S^z_{2n,l}\sigma_{2n-1,l} + J_d(S^z_{2n,1}\sigma_{2n-1,2} + S^z_{2n,2}\sigma_{2n-1,1}) \\
&+ \frac{h}{2}\sum_{l=1}^{2}(2S^z_{2n,l} + \sigma_{2n-1,l} + \sigma_{1,l}). \qquad (5.2)
\end{aligned}$$

h is the applied magnetic field. Here $\mathbf{H_e}$ is the part of the Hamiltonian representing the two edges. With the periodic boundary condition (PBC), $\mathbf{H_e}$ vanishes and the total Hamiltonian becomes $\mathbf{H} = \sum_{i=1}^{n} \mathbf{H_i}$ with appropriate reduction of values of site index, e.g. $\sigma_{2n+1,1} \equiv \sigma_{1,1}$. If our system is considered to be summation over n geometrical units, then each unit is represented by the $\mathbf{H_i}$. It may be noted here that $[\mathbf{H_i}, \mathbf{H_j}] = 0$ even for $j = i + 1$.

For this work, we consider $J_c = J_{cq} = 1$. The GS phase diagram of the system

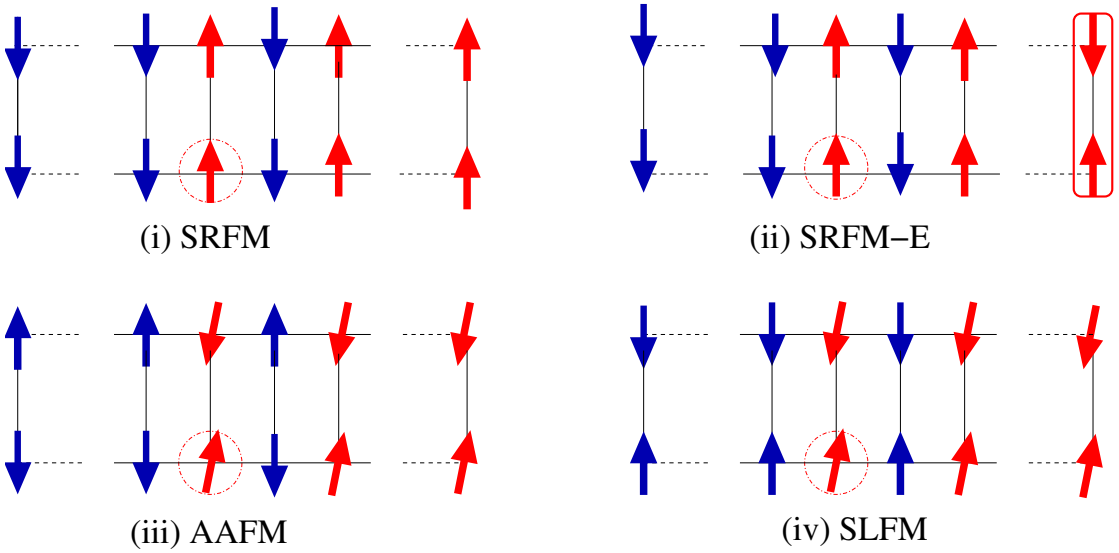

FIGURE 5.2: (Color online) Spin arrangements in (i) stripe rung ferromagnetic (SRFM), (ii) stripe rung ferromagnetic edge (SRFM-E), (iii) anisotropic antiferromagnetic (AAFM) and (iv) stripe leg ferromagnetic (SLFM) phases are shown. Arrows in the odd rungs (blue) and even rungs (red) represent σ-type and S-type spins respectively. In subfigure (ii), the uncompensated dimer is shown in the box.

is studied here with the respective to the parameters J_d and J_q (both positive). For the system with open boundary conditions the exact diagonalization (ED) method is used to calculate the GS properties like the energies and correlation functions up to 24 sites, whereas the thermodynamical properties of the system with periodic boundary conditions are studied using the transfer matrix method [256]. The total GS energy of the system can be written as the sum of the GS energies of the individual units calculated separately since the Hamiltonians of the individual units commute with each other, but we have used the ED method to calculate the correlation functions of the system as the GS wave function is not a simple product of the GS wave functions of the individual units.

5.3 Results

In this section, four phases are discussed in detail to understand and characterize the phases and determine their boundaries, we calculate various quantities like longitudinal $C^L(r) =< S_i^z S_{i+r}^z >$, transverse $C^T(r) =< (S_i^x S_{i+r}^x + S_i^y S_{i+r}^y) >$

correlations, von Neumann entropy, concurrence and energy crossovers. There are four major phases in the system: (i) stripe rung ferromagnet (SRFM) where the same type of sublattice spins (either S or σ-type spins) are aligned in the same direction, whereas other types are aligned along the opposite direction, as shown in Fig. 5.2.a. This phase is similar to the SR phase described in Ref.[98]. (ii) In stripe rung ferromagnetic-edge (SRFM-E) phase, bulk spins behave like SRFM phase, whereas the one of the edge spin pair ($S-S$) behaves like isolated singlet as shown in Fig. 5.2.b and the GS is in $S^z_{tot}=1$ sector where S^z_{tot} is the total S^z for the entire ladder. (iii) In anisotropic antiferromagnetic (AAFM) phase, both S and σ-type of spins are antiferromagnetically aligned with each other, two nearest S spins along the rung form an anisotropic singlet bond to be defined below, whereas two nearest σ spins form an Ising bond as shown in Fig. 5.2.c. This phase is similar to the Néel phase described in Ref.[98]. The anisotropy of singlet bond decreases with increasing J_q and spins are highly frustrated. (iv) In this phase, spins on each leg are ferromagnetically aligned but spins on the other leg are antiferromagnetically aligned with each other (Fig. 5.2.d) and therefore this frustrated arrangement is called stripe leg ferromagnet (SLFM). This phase is similar to the SL phase described in Ref.[98].

5.3.1 Quantum phase diagram

In Fig. 5.3 the four phases, the SRFM, the SRFM-E, the AAFM, and the SLFM are shown separated by five phase boundaries for $N=24$, and we notice that the phase boundaries weakly depend on the system size. These phase boundaries are determined based on energy crossovers and the correlation functions $C^L(r)$ and $C^T(r)$ by tuning J_d and J_q. A large fraction of the phase space is covered by the SRFM phase and the AAFM phase has the second largest contribution. It is interesting to note that the phase boundary of the AAFM and the SLFM is at $J_d/J=1$ for large J_q. Here, the bond order $< S_i \cdot S_{i+1} >$ between the two S spin along the rung form a perfect singlet dimer. The correlation length in $C^L(r)$ shrinks to one unit cell, but this phase is restricted to only this phase boundary.

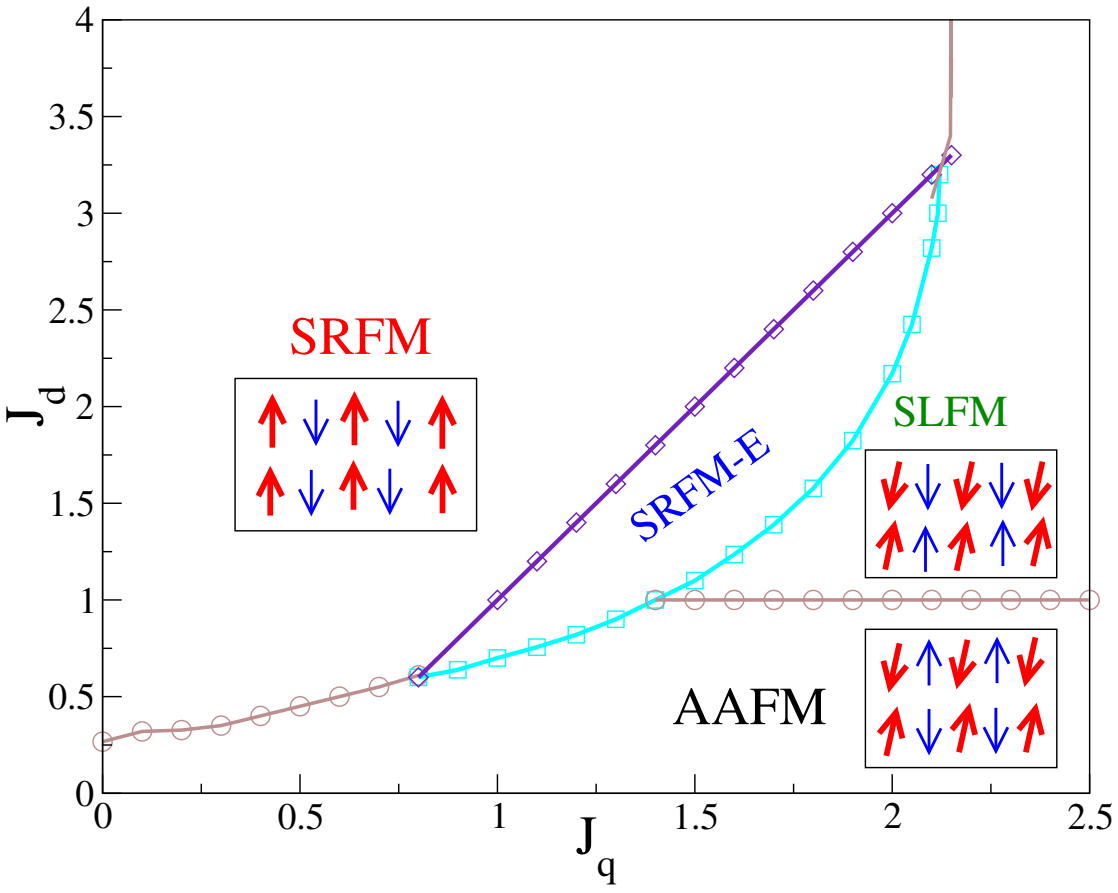

FIGURE 5.3: (Color online) Quantum phase diagram of the Ladder with open boundary condition is shown. Spin arrangements of the AAFM, the SLFM, and the SRFM phases are shown inside the boxes.

The strong singlet dimers along the rung at B type sublattice $(\sigma - \sigma)$ are formed on either side of the phase boundary.

5.3.2 Ground state energy and excitation gap

The GS energy E_{GS} of the system is doubly degenerate in the major part of the parameter space, and E_{GS} and the lowest excited state in $S^z_{tot} = 0$ and 1 sectors are analyzed as shown in Fig. 5.4. The lowest state energy in $S^z_{tot} = 0$ and 1 sectors are shown in Fig. 5.4.a for $J_q = 0.2$. The lowest energy E_{GS} in $S^z_{tot} = 0$ sector initially increases with J_d due to enhancement in the frustration induced by J_d and it starts to decrease again for $J_d > 0.33$, as the J_d becomes dominant and frustration decreases and the system goes to the SRFM phase. The peak of E_{GS} indicates the phase boundary. For small J_q the phase transition from the AAFM

to the SRFM seems to be sharp as the derivative of E_{GS} is discontinuous as shown in Fig. 5.4 a. Whereas, the change in E_{GS} is continuous for $0.5 < J_d < 1.5$ at large J_q as shown in Fig. 5.4.c. In Fig. 5.4.b the lowest excited state in $S^z_{tot} = 0$ and the lowest state in $S^z_{tot} = 1$ sector are shown with black and red color line-symbols for $J_q = 1$ respectively. The negative value of the red curve indicates the $S^z_{tot} = 1$ as GS and the state appears because of a singlet dimer pair formation between edge $S - S$ spins if the chain starts with $\sigma - \sigma$ spin pair (odd rungs) and ends with $S - S$ spin pair (even rungs) as considered in the system. In this case, a pair of uncompensated ferromagnetically aligned $\sigma - \sigma$ pairs give rise to the $S^z_{tot} = 1$ manifold. The boundaries for the SRFM-E are obtained by onset and end of the GS with $S^z_{tot} = 1$ as shown in Fig. 5.4.b.

In Fig. 5.4.c all four phases and their boundaries are shown for $J_q = 1.8$. We notice that the maxima of doubly degenerate GS is the phase boundary between the AAFM and the SLFM phase, whereas, the onset and end of GS in the $S^z_{tot} = 1$ is the phase boundary of the SRFM-E phase. In the SRFM phase, the GS is again in the $S^z_{tot} = 0$ sector. It is also evident from all three figures that E_{GS} is continuous in large J_q limit.

5.3.3 von Neumann entropy and concurrence

For a better understanding of the quantum nature of the phases and to characterize the quantum phase boundaries the von Neumann entropy S_{vN} and the concurrence C are calculated. The relevant results can be seen in Fig. 5.5. The von Neumann entropy and the concurrence are two measures of the quantum entanglement between two parts of a composite system. If ρ is the reduced density matrix of one part of a given bipartite system (in a pure state) then the von Neumann entropy is given by S_{vN}=-Tr[ρ ln(ρ)] and the concurrence is given by $C = \sqrt{2[1 - Tr(\rho^2)]}$ [257]. These two quantities are zero for separable states and non-zero for entangled states. For the calculation of these quantities, we partition the system in the middle into the left (system) and right (environment) blocks and calculate the reduced density matrix for the left (system) block. From Fiq. 5.5 we find that

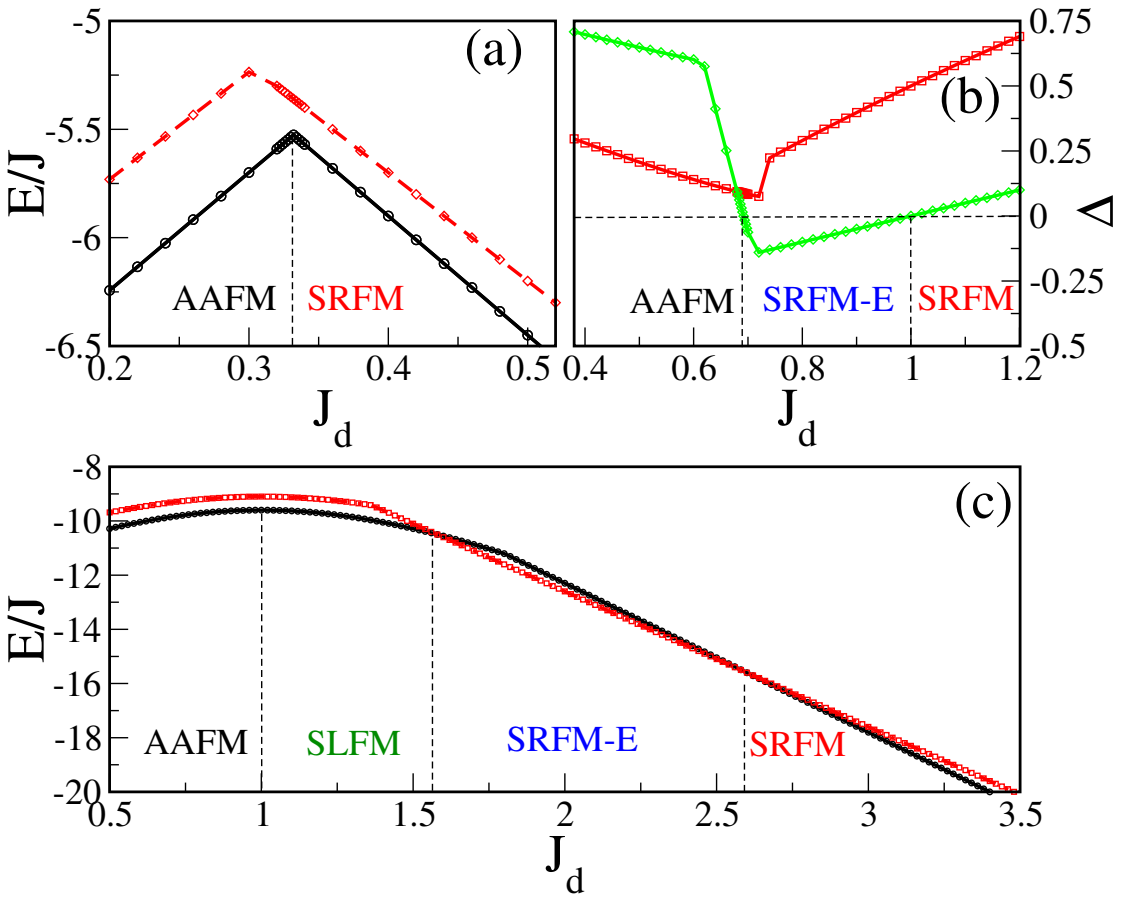

FIGURE 5.4: (Color online) (a) Black solid line and red dashed line represent the lowest energies (E/J) in two respective spin sectors: $S^z_{tot} = 0$ and $S^z_{tot} = 1$ for $J_q = 0.2$, (b) Δ is the energy gap for $J_q = 1.0$. Red solid line represents the lowest energy gap in $S^z_{tot} = 0$ sector and green solid line represents the energy gap of the lowest state in $S^z_{tot} = 1$ sector from the lowest state in $S^z_{tot} = 0$ sector. (c) The black solid line and red dashed line represent the lowest energies (E/J) in two respective spin sectors: $S^z_{tot} = 0$ and $S^z_{tot} = 1$ for $J_q = 1.8$. (E/J) and Δ in all the subfigures are shown for system size N=24.

both S_{vN} and C are zero for the SRFM and the SRFM-E phases. This is expected as for the large J_d values the GS can be represented as the product of individual spin configurations. For the AAFM and the SLFM phases, the quantities S_{vN} and C are nonzero as shown in Fig. 5.5. For $J_q = 1.8$ the GS is doubly degenerate and both the states have the same values of S_{vN} and C, but at phase boundary of the AAFM and the SLFM $J_d = 1$ the GS is N fold degenerate which leads to a sudden jump of these quantities. S_{vN} and C of the AAFM and the SRFM phase for $J_q = 0.2$ are shown in Fig. 5.5 a and sudden jump from a high value in the AAFM phase to zero in the SRFM phase characterizes the phase boundary. Similarly, the phase boundary of the SLFM and the SRFM-E phase for $J_q = 1.8$

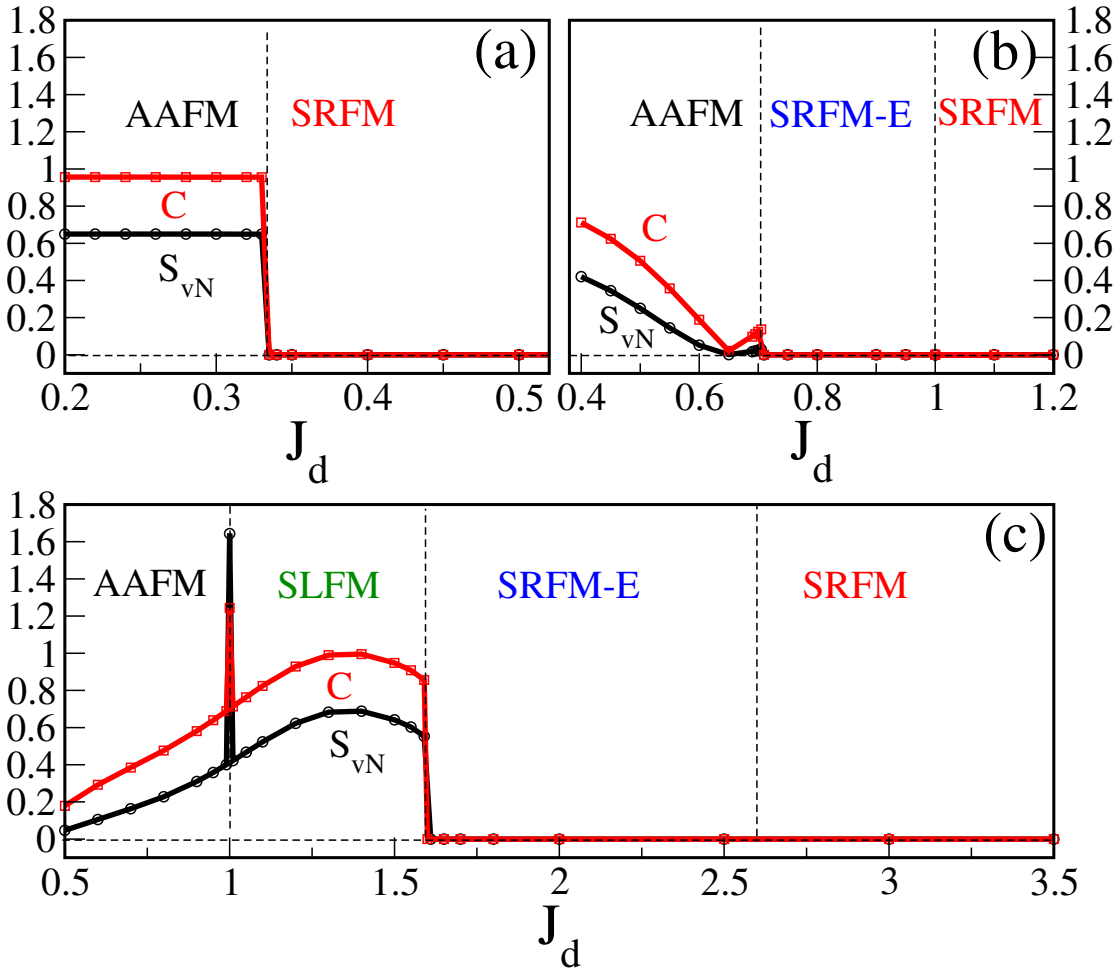

FIGURE 5.5: (Color online) Black and red lines represent respectively the von Neumann entropy (S_{vN}) and concurrence (C) for three different sets: (a) $J_q = 0.2$,(b) $J_q = 1.0$, (c) $J_q = 1.8$

.

can be characterized by the sudden jump in Fig. 5.5 c. These phase boundaries calculated from this criterion are consistent with other calculations.

5.3.4 Correlation functions

To understand the arrangement of spin in the GS, we study the two-component: longitudinal $C^L(r)$ and transverse $C^T(r)$ correlations in four different phases as shown in Fig. 5.6. The reference site is at the lower leg of sublattice A (S-type spin) at mid of the ladder and the arrangement of distance r is shown in Fig. 5.1. In the SRFM phase ($J_q = 0.2, J_d = 2.0$), the $C^L(r)$ shows long-range behavior, and the nearest neighbor along the rung is ferromagnetically aligned,

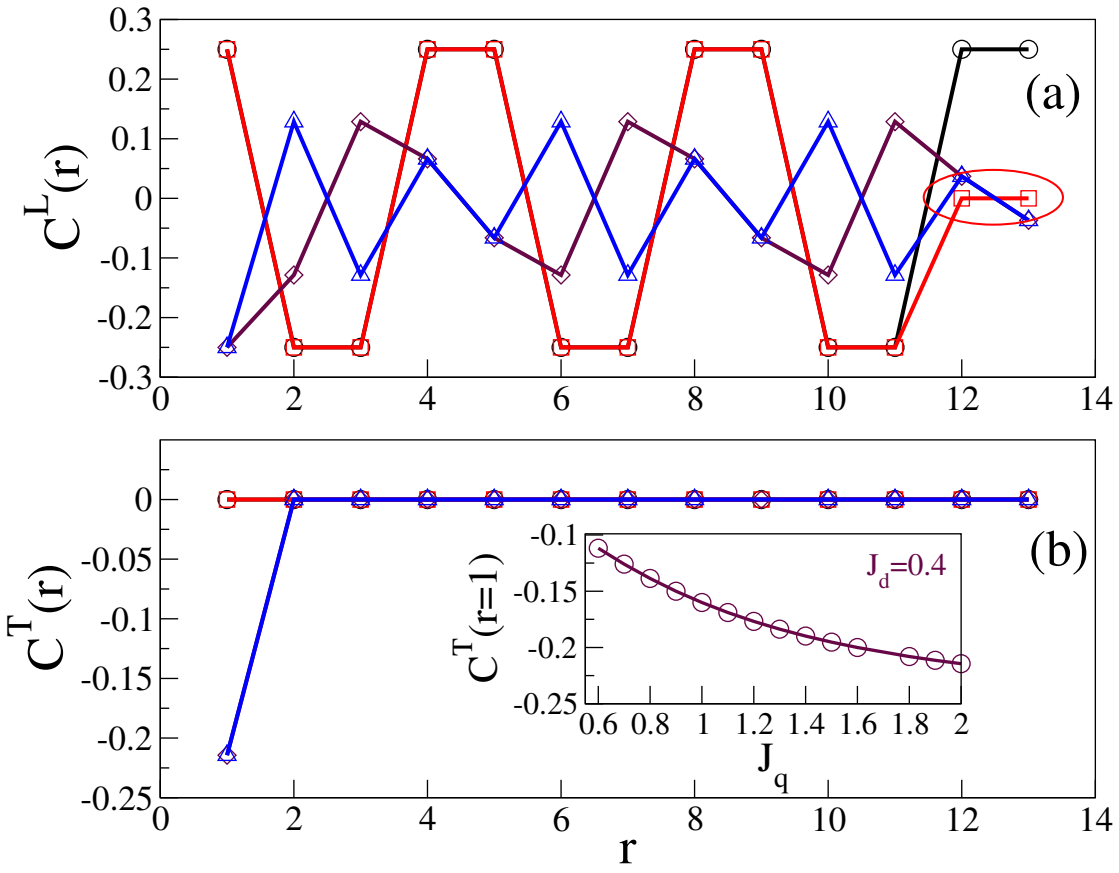

FIGURE 5.6: (Color online) (a) Longitudinal and (b) Transverse Correlation plots are shown. Black, red, maroon, and blue colors in both of the subfigures, represent four respective phases; SRFM ($J_q = 0.2$,$J_d = 2.0$), SRFM-E ($J_q = 1.6$,$J_d = 1.25$), AAFM ($J_q = 2.0$,$J_d = 0.4$) and SLFM ($J_q = 2.0$,$J_d = 1.6$). Transverse correlation $C^T(r = 1)$ as function of J_q is shown for $J_d = 0.4$ in the inset of (b).

whereas the nearest neighbor along the leg is antiferromagnetically aligned. The $C^T(r)$ is zero for spins, therefore, GS is completely Ising-like. In the SRFM-E ($J_q = 1.6, J_d = 1.25$), the correlation functions are the same as that for the SRFM except at the boundary where the $C^L(r)$ goes to zero i.e the last pair of spins is decoupled from the ladder. The $C^T(r)$ is zero for all spins with respect to reference spin, but between edge rung spin pair $S - S$ it is $-1/4$. In the SLFM phase ($J_q = 2.0, J_d = 1.6$), the nearest rung spins are antiferromagnetically aligned, whereas along the leg nearest neighbor spins are ferromagnetically aligned. The nonzero value of $C^T(r)$ is restricted to the nearest rung spin. However, in the limit $J_q = 2.0, J_d = 0.4$ (AAFM phase), the $C^L(r)$ is long-range and both the nearest spins along the rung and the leg are antiferromagnetically aligned. The $C^T(r)$ is

restricted to the only nearest rung spin and the $C^T(r=1)$ decreases with J_q as shown in the inset of Fig. 5.6.b. It is also interesting to note that the long-range behavior in the correlation $C^L(r)$ melts with increasing J_q.

The AAFM phase is interesting due to the high anisotropy correlations in the system and also the rapid variation in the correlation with J_q. To our surprise, at $J_d = 1$, two nearest spins along the rung ($S - S$ pairs) form perfect singlet dimers, and the GS of the system behaves like the product of Ising and singlet dimers. To show the GS spin arrangement, $C^L(r)$ and $C^T(r)$ for $J_d = 0.8, 1$ and 1.2 for $J_q = 2.0$ are plotted as a function of distance r in Fig. 5.7. We notice finite value of $C^L(r)$ and $C^T(r)$ are restricted to nearest rung spin, whereas, $C^L(r)$ are non-collinear in nature in the neighborhood of $J_d = 1$ for large J_q. For two values of $J_d = 0.8$ and 1.2 for $J_q = 2.0$, $C^L(r)$ shows non-collinear spin arrangement and the $C^T(r)$ is restricted to the same rung in A sublattice (S spin) as shown in Fig. 5.7.

5.3.5 Exact thermodynamical properties

The spin model Hamiltonian in Eq. 5.1 has commuting bond operators because Ising exchange interactions along the leg and diagonal of the ladder, therefore using the transfer matrix method exact solution at finite temperature can be studied. In this paper, we study the low-temperature thermodynamical properties of our model using a suitably adapted transfer matrix method. Henceforth, our transfer matrix calculations assume periodic boundary condition (PBC) and we will be using the full Hamiltonian without the edge part ($\mathbf{H_e} = 0$). The Hamiltonian for a single geometrical unit (Eq.5.1) can be reduced in the following manner:

$$\mathbf{H_i} = \frac{J_q}{2}\left(S^+_{2i,1}S^-_{2i,2} + S^+_{2i,2}S^-_{2i,1}\right) + J_q\left(S^z_{2i,1}S^z_{2i,2}\right) + aS^z_{2i,1} + bS^z_{2i,2} + c + d. \tag{5.3}$$

Here a, b, c, d can be written in terms of the parameters J_c, J_{cq}, J_d and h, and the spin operator σ (see in appendix **??**). In the equation S^+, S^- are the creation

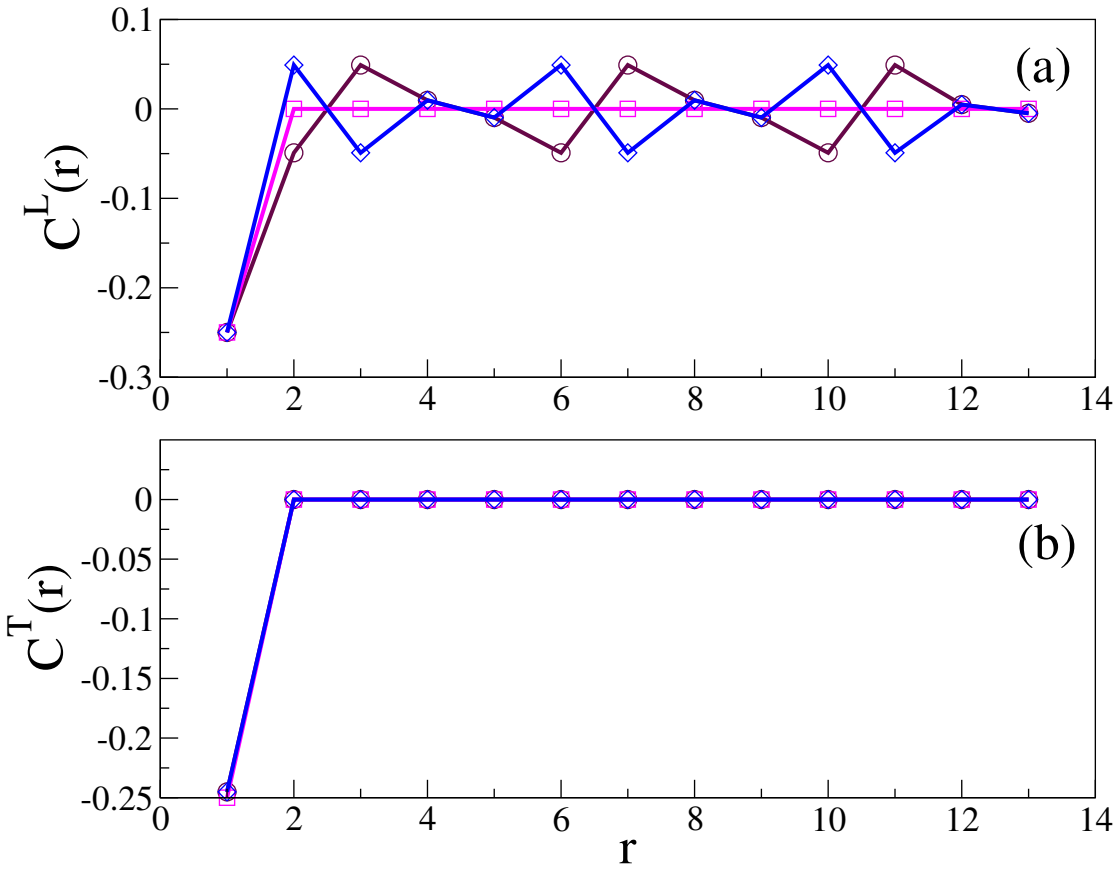

FIGURE 5.7: (Color online) (a) Longitudinal and (b) Transverse Correlations for three phases are shown. Maroon, magenta, and blue colors in both of the subfigures are for AAFM ($J_q = 2.0$, $J_d = 0.8$), Perfect Dimer ($J_q = 2.0$, $J_d = 1.0$) and SLFM ($J_q = 2.0$, $J_d = 1.2$) phases respectively.

and annihilation operators respectively for spin S.

Due to special construction of our model, we have $[\mathbf{H_i}, \mathbf{H_j}] = 0$ for any i and j. This fact helps us to write the partition function of the total system as the trace of the n-th power of a small (4×4) transfer matrix (see the details in Appendix **??**). The partition function for $N(= 4n)$ number of spins, $Q_N(\beta) = Tr(e^{-\beta \mathbf{H}})$ with β being the inverse temperature can be written as,

$$Q_N(\beta) = \lambda_1^n + \lambda_2^n + \lambda_3^n + \lambda_4^n,$$

where four λ's are the eigenvalues of the transfer matrix. If λ_1 is the largest eigenvalue then for large N, $Q_N(\beta) = {\lambda_1}^n$ (see in appendix **??**). Using the partition function $Q_4(\beta)$ $(= \lambda_1$, partition function for a geometric unit), the

thermodynamic quantities can be calculated using the following standard formulas: free energy (per geometrical unit) $F(T) = -k_B T \log Q_4(\beta)$, average energy $E(T) = k_B T^2 \frac{d}{dT} \log Q_4(\beta)$, specific heat $C_v(T) = \left(\frac{\partial E(T)}{\partial T}\right)_v$, magnetization $M(T) = -\frac{\partial F(T)}{\partial h}$, magnetic susceptibility $\chi(T) = \frac{\partial M(T)}{\partial h}$, and entropy $S(T) = -\left(\frac{\partial F(T)}{\partial T}\right)$.

In $T \to 0$ limit, the largest eigenvalue λ_1 can be written as $\lambda_1 = e^{\frac{\beta(1+J_q(1+2\Delta_2))}{4}} + e^{\frac{\beta(4J_d - J_q + 3))}{4}}$, where $\Delta_2 = \sqrt{1 + 4\frac{(1-J_d)^2}{J_q^2}}$ (see in appendix **??**). In the zero-temperature limit, the first exponential term in the expression of λ_1 dominates over the second exponential term in the regimes corresponding to the AAFM and the SLFM phases, while in the regime corresponding to the SRFM phase, the opposite happens. In this $T \to 0$ limit, the free energy takes the following forms in the regimes corresponding to the SRFM and the AAFM phases respectively: $F_{SRFM} = -\frac{4J_d - J_q + 3}{4}$ and $F_{AAFM} = F_{SLFM} = -\frac{1+J_q(1+2\Delta_2)}{4}$. In this zero temperature limit, in all three regimes, the entropy and the specific heat are found to be zero. These results match well with our numerical calculations using the full expression of λ_1 (see in appendix **??**).

To understand the thermodynamic behavior at the non-zero temperatures, we calculate four thermodynamical quantities $E(T)$, $C_v(T)$, $S(T)$ and $\chi(T)$ for three parameter regimes and are shown in Fig. 5.8. We use the full expression of the largest eigenvalue λ_1 for this numerical calculation. It may be noted that the different ground state phases of the system, which were obtained with open boundary conditions for the finite system sizes, may not have direct consequences in our low-temperature thermodynamic results as the thermodynamic calculations are done with periodic boundary conditions for thermodynamically large systems. Here, our main purpose of studying the thermodynamical quantities is to see how these quantities change across the parameter regimes of interest. The $C_v(T)$ of the three different phases show different features as shown in Fig. 5.8.a. In the AAFM region where J_d is weak and J_q is dominant, $C_v(T)$ shows a small peak near the $T \to 0$, which may be because of small gap due to small excitation gap in $S^z_{tot} = 0$ sector, and then there is broad maxima at higher temperature, which is similar to the Heisenberg spin dimer system. The weak singlet dimer is formed along the

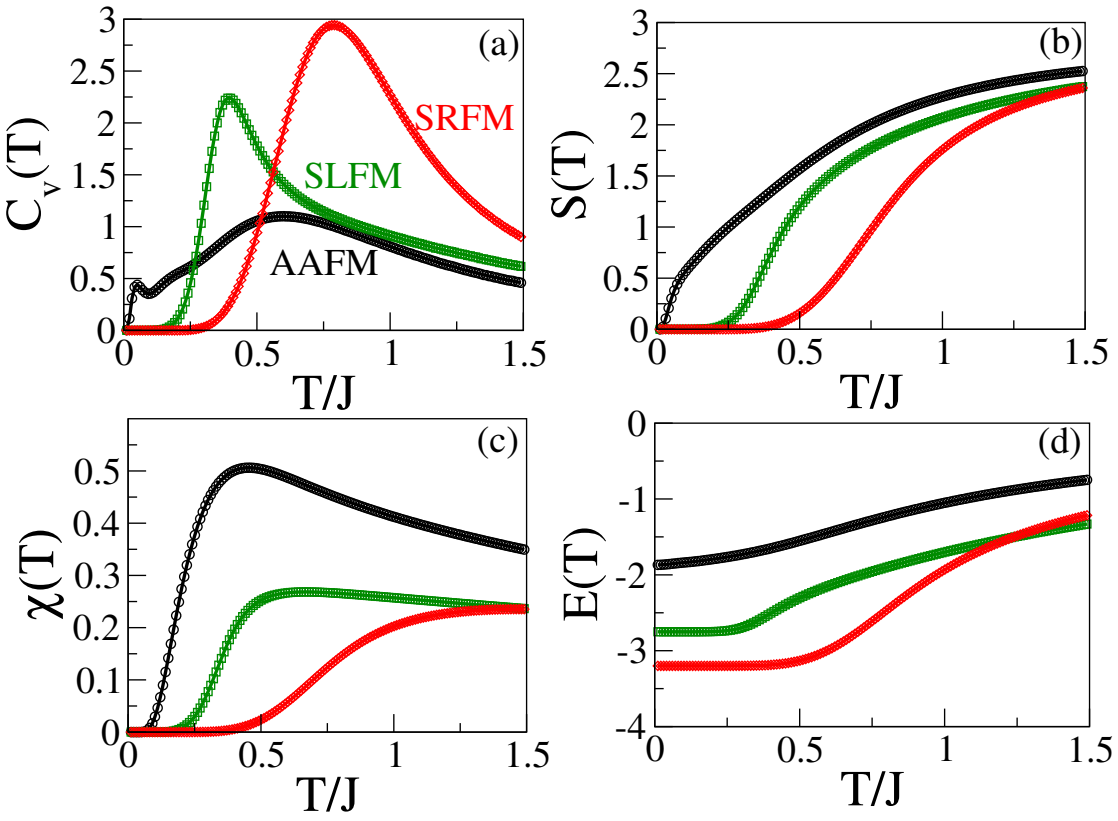

FIGURE 5.8: (Color online) (a) Specific heat ($C_v(T)$), (b) Entropy ($S(T)$), (c) Magnetic susceptibility ($\chi(T)$) and (d) Average Energy ($E(T)$) plots are shown. Black, red, and green curves in each of the subfigures, represent three phases: AAFM ($J_q = 2.0$, $J_d = 0.5$), SLFM ($J_q = 2.0$, $J_d = 2.5$) and SRFM ($J_q = 0.2$, $J_d = 2.5$) respectively.

rung of $S - S$ spins and that may give a broad peak at moderate temperature. The $C_v(T)$ in the SLFM phase shows a very sharp peak and long tail but has a vanishing small value for $T/J < 0.09$ due to a finite energy gap in the system. In the SRFM phase, this quantity is vanishingly small for $T/J < 0.35$ due to a large magnetic gap, in this case system requires a relatively larger temperature to have a significant contribution from the higher excited states or to have significant energy fluctuation. In this phase the $C_v(T)$ increases exponentially and has a relatively higher peak position at $T/J = 0.75$. The entropy $S(T)$ is a measure of randomness in the system and also indicates a contribution from various energy levels, and it is shown for three different phases of the system in Fig. 5.8.b. In the AAFM phase, there is a small gap in the $S^z_{tot} = 0$ sector. Whereas, in the other two phases $S(T)$ is vanishingly small for $T/J < 0.1$ due to the large energy gap, and thereafter it increases monotonically.

The magnetic susceptibility $\chi(T)$ in these three phases are shown in Fig. 5.8.c and all the $\chi(T)$ have small values in all three phases for $T/J < 0.1$. It has a broad maximum and small gap in the AAFM phase due to the formation of a singlet dimer, and breaking the weak singlet dimer costs finite energy, therefore, a singlet-triplet gap is finite. The $\chi(T)$ in the SRFM phase has a dominant Ising interaction, therefore, there is a finite energy gap and sharp peak similar to the 1D Ising system. In the SLFM phase, there is a large magnetic gap as it requires breaking of strong rung interaction, and this leads to small $\chi(T)$ at low temperature and an exponential increase in the $\chi(T)$. The average internal energy $E(T)$ shows a linear variation with T in the AAFM phase, but almost constant value of $E(T)$ for $T < 0.09$ indicates the gap in the SLFM phase as shown in Fig. 5.8.d. In the SRFM phase, variation of the energy is almost constant for $T/J < 0.35$ due to a large energy gap and it varies linearly with T thereafter.

5.4 Summary

In this paper, we consider a very general anisotropic Heisenberg-Ising model on a ladder geometry with alternate Heisenberg and Ising exchange rung interactions, whereas the exchange interactions along the leg and the diagonal of the ladder are Ising type. We construct a quantum phase diagram of the model, Hamiltonian in Sec.5.2, and have shown that there are four quantum phases: (i) the AAFM, (ii) the SRFM, (iii) the SRFM-E, and (iv) the SLFM which appear due to competing interactions and anisotropy in the system. The GS is doubly degenerate and has a finite magnetic gap in most of the parameter space and to our surprise, the exact dimer state along the rung in A sublattice (rungs with isotropic exchange interactions) appears for $J_d = 1$ and large J_q limit. However, a weak dimer appears along the rung of spin S near to $J_d = 1$. The von Neumann entropy and concurrence have non-zero values in the AAFM and the SLFM phases, and these quantities change sharply from one phase to other phases, therefore we can convincingly determine the phase boundaries between various phases which are consistent with the other calculations.

The thermal properties of this system are also studied analytically using the transfer matrix method. Four temperature-dependent properties like specific heat $C_v(T)$, average internal energy $E(T)$, entropy $S(T)$, and magnetic susceptibility $\chi(T)$ are studied in three different phases: the SRFM, the SLFM, and the AAFM. In large $\frac{J_q}{J_d}$ regime (AAFM phase), $C_v(T)$ shows a small peak at small T due to a small excitation gap, whereas it has vanishingly small $\chi(T)$ up to $T < 0.09$ due to the finite magnetic gap in the SLFM phase. Due to the large excitation gap in the SRFM phase, all four quantities vanish for $T < 0.35$. This model may be realized in Cu or Ni-based materials having magnetic interaction confined in ladder-like geometry and the material should also have large anisotropy to ensure the Ising exchange.

Chapter 6

Magnetic plateaus and jumps in a spin-1/2 ladder with alternate Ising-Heisenberg rungs: a field dependent study

6.1 Introduction

Frustrated low-dimensional quantum magnets exhibit a diverse range of quantum phases that generate significant interest among both theorists and experimentalists. Consequently, theoretical studies are crucial for verifying experimental results, especially due to the continuous synthesis of low-dimensional magnetic materials[53, 144, 146, 217–224, 258–261]. In the spin chains and ladder systems, the competing exchange interactions lead to many interesting quantum phases like ferromagnetic ground state (GS) [262], Néel phase [45, 46, 263], Luttinger liquid [85, 264], spiral [244], spin liquid [80, 265], dimer phase [53], etc. The antiferromagnetic isotropic Heisenberg spin-1/2 zigzag ladder or the $J_1 - J_2$ chain has a gapless spectrum in strong leg coupling limit, whereas, it has a gapped spectrum

for the moderate value of the ratio of the exchange interactions due to dimerization along the rung. [30, 66, 96, 206, 207, 216, 266].

The anisotropy in the exchange interaction significantly influences the GS properties. For example, the isotropic Heisenberg spin-1/2 $J_1 - J_2$ model in the small J_2 limit has a gapless spectrum and its GS is a spin liquid phase with quasi-long range order (QLRO)[30, 206, 207]. But, the spectrum of the XXZ Heisenberg spin-1/2 chain is gapped for a large axial anisotropy $\Delta > 1$, and in this limit, the spins behave like Ising type, whereas, the spectrum is gapless for $\Delta < 1$ and spins are aligned in XY plane [103, 209]. The GS of an isotropic Heisenberg spin-1/2 normal ladder exhibits short range order and the spin gap is finite for any non-zero value of rung exchange. On the other hand, the spectrum of the anisotropic ladder systems can be gapless [44, 97, 103, 104, 267–269]. In a spin-1/2 ladder with isotropic rung and axial anisotropic leg exchange Δ, the GS can be tuned from singlet to Néel phase by increasing Δ [104]. But, for a normal spin-1/2 ladder with anisotropy in both leg and rung exchange interactions, the GS can be XY, Néel, or rung singlet (RS) phase on tuning the rung exchange and axial anisotropy [268]. Another type of anisotropic spin-1/2 ladder is the Kitaev-Heisenberg model on a two-leg ladder where the GS has many exotic quantum phases [269].

Many spin-1/2 ladders with isotropic and anisotropic exchange interactions are reported to display magnetic plateaus and jumps in the magnetization curve by tuning the external magnetic field [51, 98, 110, 252, 254, 270–279]. Japaridze et al. studied a two-leg spin-$\frac{1}{2}$ ladder system with leg interaction $J_{\parallel}$ and alternate rung as $J_{\perp}^{+}$, $J_{\perp}^{-}$ in presence of a longitudinal field h, and show that the system have zero magnetization plateau up to h_{c1}^{-}, a plateau at half of the saturation magnetization for the magnetic field between h_{c1}^{+} and h_{c2}^{-} and fully polarized spin is achieved at h_{c2}^{+} [275]. Moradmard et al. studied a spin-1/2 ladder system with XXZ interaction and they showed different phases like x-FM, z-FM, y-Néel, and z-Néel in a magnetic phase diagram in the plane of anisotropy interaction Δ and magnetic field h [276]. Similarly, Dey et.al. carried out the magnetization study of isotropic Heisenberg spin-1/2 on a 5/7-skewed ladder and showed multiple plateau phases with field h [51]. They also note that plateau phases are the consequences

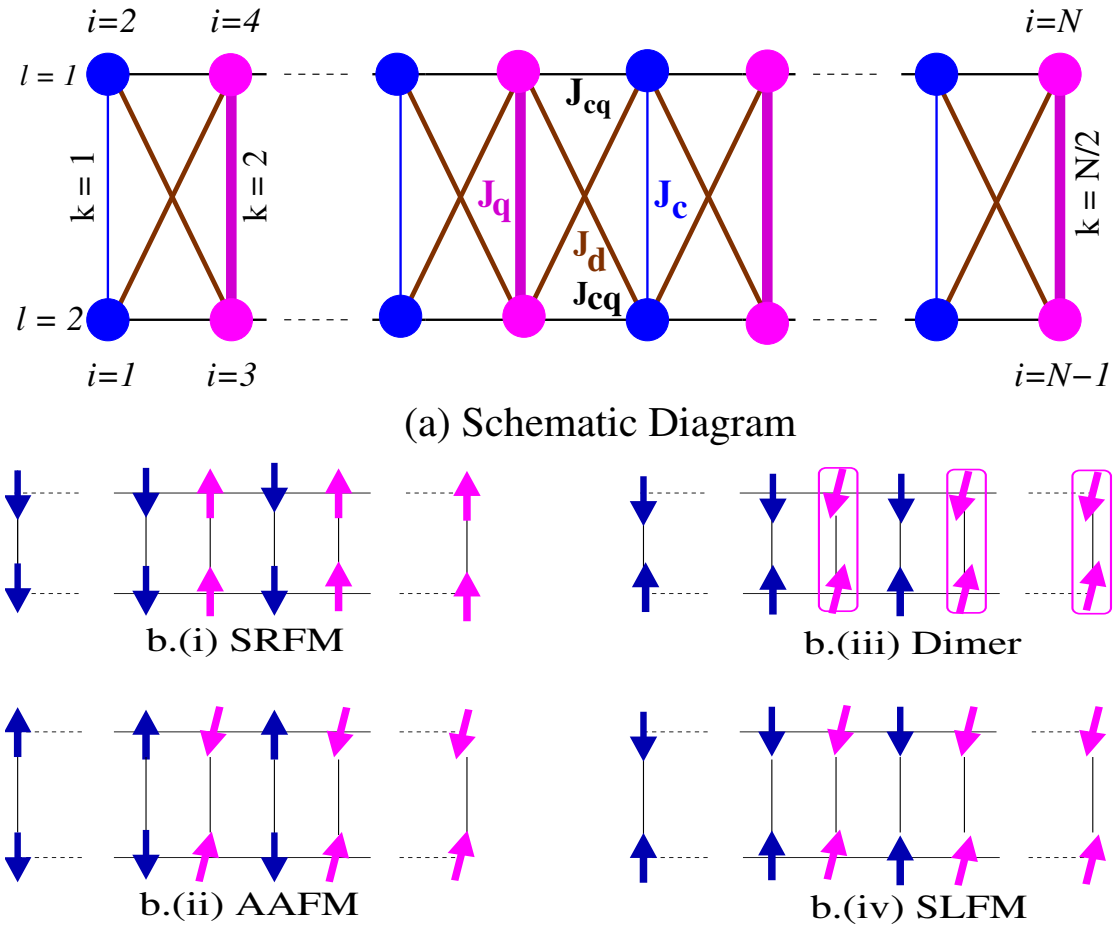

FIGURE 6.1: (color online) (a) Schematic diagram of the spin ladder with alternate Ising-Heisenberg rung interactions. J_c and J_q are the alternative Ising and Heisenberg type rung interactions respectively. J_{cq}, J_d are the Ising type leg and diagonal exchange interactions respectively. Blue and magenta color circles represent σ and S spins in Eq.6.1 respectively. l, k, and i represent leg and rung, and site indices respectively. The spin configurations of four exotic phases with $J_c = J_{cq} = 1$: b.(i) SRFM ($J_q = 0.2$, $J_d = 2.0$), b.(ii) AAFM ($J_q = 2.0$, $J_d = 0.4$), b.(iii) Dimer ($J_q = 2.0$, $J_d = 1.0$), and b.(iv) SLFM ($J_q = 2.0$, $J_d = 1.6$) are shown. Blue and magenta rung pairs are representing $\sigma - \sigma$ and $S - S$ rung pairs. The boxes shown in Subfigure b.(iii) represent perfect singlets. Quantum phases are studied earlier in Ref. [1].

of gaps in the spectrum, and these plateau phases can be explained in terms of Oshikawa, Yamanaka, and Affleck (OYA) criterion [110].

Some of the real compounds like the heterobimetallic co-ordination polymer $[(Tp)_2$-$Fe_2\,(CN)_6(OAc)(bap)\,Cu_2(CH_3OH)_2CH_3OHH_2O]$ forms an effective Ising- Heisenberg spin-1/2 branched chain model [278], whereas, $(VO)_2P_2O_7$, CaV_2O_5 and MgV_2O_5 can be modeled by using two legs spin-1/2 ladders with the Ising-Heisenberg

exchange [98]. The quantum phase diagram, magnetization curves, and concurrence of the spin-1/2 Ising Heisenberg branched chain are studied using the transfer-matrix method and they note the plateau at 1/2 of saturation magnetization [278]. For a two-leg spin-1/2 ladder with Ising exchange along the leg, diagonal, and Heisenberg exchange along the rung, Verkholayak et. al. noted that on applying a longitudinal magnetic field, the Néel phase of the GS undergoes a phase transition to a half plateau or staggered bond (SB) phase in presence of moderate field and to a fully spin-polarized state for strong field limit [98]. With few similarities to these ladder systems, we propose another type of anisotropic spin-1/2 two-leg ladder which may have various types of plateau at 0, 1/2, and full of saturation magnetization. The quantum phase transition in these systems can alternatively be determined using the concurrence [280, 281] and fidelity [282] calculations.

We consider a spin-1/2 frustrated two-leg ladder system with alternating Ising and Heisenberg type rung exchanges, where the diagonal and leg exchange are of Ising type as shown in Fig.6.1.a. In this model, J_c and J_q are the alternate Ising and Heisenberg rung exchange interactions respectively, where, J_{cq} and J_d are the leg and diagonal exchange interaction strengths of Ising type respectively. The quantum phase diagram of this model is studied earlier in parameter space of J_q and J_d (both are antiferromagnetic) by considering $J_c = J_{cq} = 1$ [1]. The system exhibits four distinct GS phases under periodic boundary condition (PBC): (i) stripe rung ferromagnet (SRFM), (ii) the anisotropic antiferromagnet (AAFM), (iii) the Dimer, and (iv) the stripe leg ferromagnet (SLFM) depending upon the values of J_q and J_d in absence of any magnetic field [1].

The GS phases are schematically represented in Fig6.1.b.[(i)-(iv)]. The SRFM phase is Ising dominated where all the spins are aligned along the z direction completely. Whereas, the [(ii)-(iv)] phases are anisotropic. Although all the rungs are anti-ferromagnetically aligned for the [(ii)-(iv)] phases, the spin arrangements along the leg are different. Along the leg, the alignment of the spins is anti-ferromagnetic for the AAFM phase and ferromagnetic for the SLFM phase. In the Dimer phase, there is no spin alignment along the leg. In this manuscript, we

study the effect of both longitudinal and transverse magnetic fields on the four GS phases with a few sets of J_q, J_d values discussed in Sec.7.3.

In this work, we observe that in all the quantum phases, the system exhibits a plateau at 0, 1/2, and 1 of saturation magnetization in the presence of an externally applied longitudinal magnetic field. The calculations are done using the exact diagonalization (ED) [283] and transfer matrix (TM) [284] methods, and results from both methods agree excellently with each other. Furthermore, we calculate the zero-temperature limit quantum fidelity, fidelity susceptibility, and quantum concurrence from the partition function of the ladder using TM, and find that these results are in accordance with the exact calculation. The study of the magnetization under a transverse field is carried out using ED only, and it is noticed that the magnetization shows a half, and full of saturation magnetization plateaus.

This paper is divided into a few sections as follows. First, the model is discussed briefly in Sec. 6.2. This is followed by a discussion on methods in Sec. 6.3. In Sec. **??**, the magnetization process is discussed in the presence of the longitudinal field. In Sec. 6.4.1.1 we discuss the zero-temperature limit quantum fidelity and bipartite concurrence for different phases. In Sec. 6.4.1.2, the quantum phase diagrams are shown for four different longitudinal fields. In Sec. 6.4.2, we discuss the magnetization process in the presence of a transverse field. In Sec. 6.5, we summarise the results and conclude the paper.

6.2 Model Hamiltonian

We construct the Hamiltonian for a spin-1/2 two-leg ladder with N number of spins periodically connected along the leg, which turns out to be comprised of $n = \frac{N}{4}$ number of unit cells. In each unit cell, one rung pair is connected through an Ising type exchange J_c, whereas, the other one is coupled with a Heisenberg type exchange J_q as shown in Fig.6.1.(a). These rungs couple each other through Ising type exchanges: J_{cq} along the leg, J_d along the diagonal. The spins with

rung coupling J_c and J_q are marked with σ and $\vec{S}$ respectively. Here onward, the Ising type and Heisenberg type rung spin pairs are to be called $\sigma-\sigma$ and $S-S$ pairs respectively. Let us now write down the Hamiltonian for the j^{th} unit cell as

$$\begin{aligned}
\mathbf{H_j} &= J_q^z S_{2j,1}^z S_{2j,2}^z + \frac{J_q^{xy}}{2}\Big[S_{2j,1}^+ S_{2j,2}^- + S_{2j,1}^- S_{2j,2}^+\Big] \\
&+ \frac{J_c}{2}\Big[\sigma_{2j-1,1}\sigma_{2j-1,2} + \sigma_{2j+1,1}\sigma_{2j+1,2}\Big] + J_{cq}\times \\
&\Big[S_{2j,1}^z(\sigma_{2j-1,1}+\sigma_{2j+1,1}) + S_{2j,2}^z(\sigma_{2j-1,2}+\sigma_{2j+1,2})\Big] \\
&+ J_d\times \\
&\Big[S_{2j,1}^z(\sigma_{2j-1,2}+\sigma_{2j+1,2}) + S_{2j,2}^z(\sigma_{2j-1,1}+\sigma_{2j+1,1})\Big] \\
&- \frac{h}{2}\sum_{l=1}^{2}(2S_{2j,l}^z + \sigma_{2j-1,l} + \sigma_{2j+1,l}) \\
&- \frac{h^x}{2}\sum_{l=1}^{2}(2S_{2j,l}^x + \sigma_{2j-1,l}^x + \sigma_{2j+1,l}^x)
\end{aligned} \tag{6.1}$$

Here, h and h^x are the longitudinal (+z direction) and transverse (+x direction) fields respectively. S^x, S^z are the spin components along +x, +z respectively of the spin $\vec{S}$, whereas, S^+, S^- are the raising and lowering operators respectively of the same. In Eq.6.1, we consider $J_c = J_{cq} = 1$ and $J_q^z = J_q^{xy} = J_q$ throughout our manuscript. The general Hamiltonian of the ladder under PBC with system size N is the summation of the n unit cells, which can be written as $\mathbf{H} = \sum_{j=1}^{n} \mathbf{H_j}$.

6.3 Methods

We employ the ED method to solve the energy eigenvalues and eigenvectors of the Hamiltonian in Eq.6.1 for the system sizes $N = 16, 20, 24$ in the presence of longitudinal and transverse fields both. Whereas, in the absence of a transverse field i.e., for $h^x = 0$, the Hamiltonian of two consecutive units commute to each other, and so we employ the TM method to calculate the magnetization, quantum fidelity, quantum concurrence from free energy, and partition function. The partition function for the entire ladder with system size N (or $n = N/4$ unit) can be

written as $Q_N(h,\beta) = Tr(e^{-\beta \mathbf{H}}) = [Q_4(h,\beta)]^n$ (see Appendix 6.6). $Q_4(h,\beta)$ is the partition function for one unit of 4 spins and β is the inverse temperature. For this model, $Q_N(h,\beta) = [\lambda_1^n + \lambda_2^n + \lambda_3^n + \lambda_4^n]$, where, $\lambda_1, \lambda_2, \lambda_3, \lambda_4$ are the eigenvalues of a 4×4 transfer matrix for one unit (see Appendix 6.6). In the limit $n \to \infty$, and with the condition $\lambda_1 \gg \lambda_2 \gg \lambda_3 \gg \lambda_4$, one can write $Q_N(h,\beta) \approx \lambda_1^n$ and $Q_4(h,\beta) \approx \lambda_1$. At zero-temperature limit i.e., for $\beta \to \infty$, after defining some of the system parameters: $\Delta_2 = \sqrt{1 + 4(\frac{1-J_d}{J_q^{xy}})^2}$, $Q = e^{\beta J_q^z/4}$, we obtain the partition function for one unit (from the Eq. 6.35 in Appendix 6.6)

$$
\begin{aligned}
& Q_4(h,\beta) = \\
& 2e^{\frac{\beta(J_c)}{4}} \times \\
& \big[2Q^{-1}Cosh[\beta h] + QCosh[\frac{\beta J_q^{xy}}{2}] + QCosh[\frac{\beta J_q^{xy}\Delta_2}{2}]\big] \\
& + 2e^{\frac{-\beta(J_c-4h)}{4}} \times \\
& \left[Q^{-1}Cosh[\beta(h-(J_{cq}+J_d))] + QCosh[\frac{\beta J_q^{xy}}{2}]\right]
\end{aligned}
\tag{6.2}
$$

For the simplicity, we rewrite the $Q_4(h,\beta)$ as a polynomial function of $e^{\beta h}$ as

$$
Q_4(h,\beta) = a_0 e^{2\beta h} + b_0 e^{\beta h} + d_0 \tag{6.3}
$$

Here, the system parameters a_0, b_0, d_0 are defined as

$$
\begin{aligned}
a_0 &= e^{-\frac{\beta}{4}(J_q^z + J_c + 4J_{cq} + 4J_d)}, \\
b_0 &= 2e^{\frac{\beta}{4}(J_q^z - J_c)} Cosh[\frac{\beta J_q^{xy}}{2}] + 4e^{-\frac{\beta}{4}(J_q^z - J_c)}, \\
d_0 &= 2e^{\frac{\beta(J_q^z + J_c)}{4}} \left[Cosh[\frac{\beta J_q^{xy}}{2}] + Cosh[\frac{\beta J_q^{xy}\Delta_2}{2}]\right] \\
&+ e^{-\frac{\beta}{4}(J_q^z + J_c - 4J_{cq} - 4J_d)}.
\end{aligned}
\tag{6.4}
$$

6.4 Results

We study the magnetization properties in the presence of a longitudinal (h) and transverse (h^x) magnetic field in Sec.6.4.1 and Sec.6.4.2 respectively. In both

of these cases, the studies are done for four sets of exchange parameters: (i) $J_q = 0.2, J_d = 2.0$ for the SRFM, (ii) $J_q = 2.0, J_d = 0.4$ for the AAFM, (iii) $J_q = 2.0, J_d = 1.0$ for the Dimer, and (iv) $J_q = 2.0, J_d = 1.6$ for the SLFM phases. It is to be mentioned that in all these cases, we consider J_c and J_{cq} to be unity.

6.4.1 Magnetization process in the presence of a longitudinal magnetic field

We obtain the per-site magnetization m for a finite system size N by calculating the spin gap i.e., the difference between the low-lying states of two different spin S^z sectors using ED. In Fig.**??**.[(i)-(iv)], we show the finite size scaling of the m-h curve for three system sizes $N = 16, 20, 24$ using ED. $m - h$ curve shows three plateau phases: $m = 0, 1/4$, and $1/2$ connected by two magnetic jumps in each of the subfigures. The first jump is at h_{c1} from $m = 0$ to $1/4$, and the other at h_{c2} from $m = 1/4$ to full saturation of magnetization ($m = 1/2$) in all four quantum phases as shown in Fig.**??**[(i)-(iv)]. The h_{c1} takes values 2.5, 0.7, 0.5, and 0.7, whereas, h_{c2} are 3.5, 3.5, 4, 4.5 for (i) the SRFM, (ii) the AAFM, (iii) the Dimer, and (iv) the SLFM phases respectively. Later on, we discuss in detail that these magnetic transitions show plateaus due to the spin gap and these jumps correspond to the overlap of the plateaus by unbinding of the rung dimers of equal energy. In all of the magnetization curves, it is noticed that there is a negligible finite-size effect. This is also noticed in the thermodynamic limit ($N \to \infty$) for the zero-temperature case ($\beta \to \infty$) using TM method.

Using the TM method, the per-site magnetization is obtained as $m = -\frac{1}{4}\frac{\partial F(h,\beta)}{\partial h}$, where $F(h, \beta)$ is the free energy for one unit and can be defined as $F(h, \beta) = -\frac{1}{\beta} ln[Q_4(h, \beta)]$. The per-site magnetization in general can be written as

$$m = \frac{1}{4} \times \frac{[2a_0 e^{2\beta h} + b_0 e^{\beta h}]}{[a_0 e^{2\beta h} + b_0 e^{\beta h} + d_0]} \tag{6.5}$$

From the above equation, it is clear that the exponential terms compete and dominate each other in different limits of fields and m can take the discrete values

$0, \frac{1}{4}, \frac{1}{2}$ (for $\beta \to \infty$). These magnetization plateaus can be connected by a few jumps which are associated with the critical fields and these critical fields are the mid-points of the jumps. At two critical fields h_{c1} and h_{c2}, m takes the values $\frac{1}{8}$ and $\frac{3}{8}$ respectively. However, the critical fields can be obtained from the Eq.6.5 as

$$h_{c1} \approx \frac{1}{\beta} ln \left[\frac{d_0}{b_0}\right], h_{c2} \approx \frac{1}{\beta} ln \left[\frac{b_0}{a_0}\right]. \tag{6.6}$$

These critical fields are found to match with the exact calculations discussed above and shown in the $m - h$ curve in Fig.**??**. Plateau width can be obtained as

$$d = |h_{c2} - h_{c1}| \approx \frac{1}{\beta} ln \left[\frac{b_0^2}{a_0 d_0}\right] \tag{6.7}$$

From the above discussion one can conclude that in $\beta \to \infty$ limit, the partition function $Q_4(h, \beta)$ of Eq.6.3 can be simplified as following

$$Q_4(h, \beta) \approx \begin{cases} d_0 & \text{if } h \leq h_{c1} \\ b_0 e^{\beta h} & \text{if } h_{c1} \leq h \leq h_{c2} \\ a_0 e^{2\beta h} & \text{if } h \geq h_{c2} \end{cases} \tag{6.8}$$

Similarly, the free energy $F(h, \beta)$ can be written for three different plateau phases

$$F(h, \beta) \approx \begin{cases} -\frac{1}{\beta} ln\big[d_0\big] & \text{if } h \leq h_{c1} \\ -\frac{1}{\beta} ln\big[b_0\big] - h & \text{if } h_{c1} \leq h \leq h_{c2} \\ -\frac{1}{\beta} ln\big[a_0\big] - 2h & \text{if } h \leq h_{c1} \end{cases} \tag{6.9}$$

From the above expressions of the free energy, it is noticed that the per-site magnetization can easily be obtained from $m = -\frac{1}{4}\frac{\partial F(h,\beta)}{\partial h}$ to be $0, 1/4, 1/2$ for the three plateau phases. All of the four nonmagnetic GS phases (i.e., $m = 0$) have a finite magnetic excitation gap and it requires a finite external magnetic field h to reach a magnetic GS. The lowest magnetic excitation is in $m = 1/4$, for which the gap from the nonmagnetic GS is closed by a finite field h_{c1}. However, the $m = 1/4$ state has also a finite magnetic excitation gap and it requires a field h_{c2} to achieve

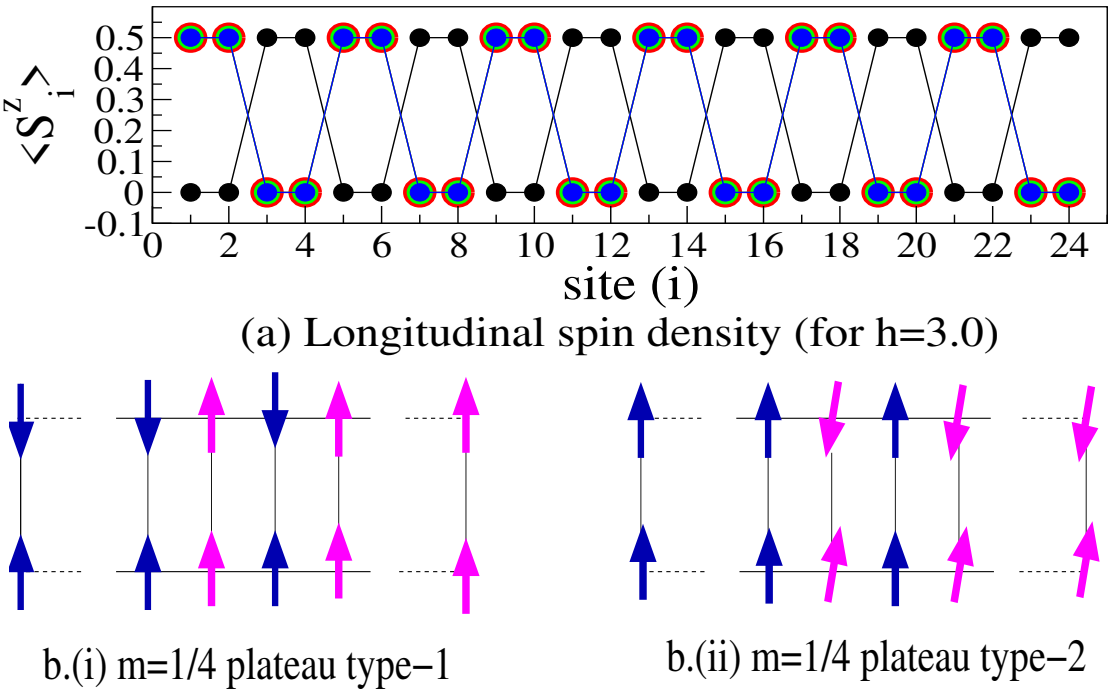

FIGURE 6.2: (a) Longitudinal spin density S_i^z is shown as a function of site index i for four GS phases: the SRFM ($J_q = 0.2$,$J_d = 2.0$), the AAFM ($J_q = 2.0$,$J_d = 0.4$), the Dimer ($J_q = 2.0$,$J_d = 1.0$), and the SLFM ($J_q = 2.0$,$J_d = 1.6$) using black, red, green, blue colors respectively. The spin configurations in b.(i) $m = 1/4$ plateau type-1, b.(ii) $m = 1/4$ plateau type-2 are shown. In $m = 1/4$ plateau type-1, all the Heisenberg rung pairs $S - S$ (magenta spins) are fully polarized, and in $m = 1/4$ plateau type-2, all the Ising rung pairs $\sigma - \sigma$ (blue spins) are fully polarized.

the higher magnetic excitation $m = 1/2$, which is a fully polarized phase (FP). All the nonmagnetic GS ($m = 0$), $m = 1/4$ magnetic GS and $m = 1/2$ magnetic GS phases can be described by the system parameters d_0, b_0, and a_0 respectively.

We obtain the per-site magnetization m for a finite system size N by calculating the spin gap i.e., the difference between the low-lying states of two different spin S^z sectors using ED. Using the TM method, the per-site magnetization for the thermodynamic limit ($N \to \infty$) is obtained as $m = -\frac{1}{4}\frac{\partial F(h,\beta)}{\partial h}$, where $F(h,\beta)$ is the free energy for one unit and can be defined as $F(h,\beta) = -\frac{1}{\beta} ln[Q_4(h,\beta)]$.

To investigate the nature of all the plateau phases, spin density $\langle S_i^z \rangle$ at site i calculated using the ED is shown in Fig.6.2. (a). The SRFM phase is stabilized in the presence of the dominant diagonal Ising exchange whereas, in the other three phases isotropic Heisenberg rung exchange is dominant. Therefore, the formation

of the $m = 1/4$ plateau from the SRFM phase (with low J_q and high J_d) is different from the other three phases. In the SRFM phase, the diagonal exchange J_d exhibits Ising characteristics and is stronger compared to the other exchanges. The formation of rung dimers and the dominant Ising exchange create a finite gap between the non-magnetic ($m = 0$) and magnetic ($m = 1/4$) phases. To close this gap and transition to the $m = 1/4$ plateau phase, a large field $h_{c1} = 2.5$ is required, as shown in Fig. **??**. (i). At this critical field, the weakly coupled Heisenberg rung dimers ($S - S$) break down and get polarized, resulting in a finite spin density of 0.5, as depicted in Fig. 6.2.(a). The ground state spin configuration for the $m = 1/4$ plateau is termed "m=1/4 plateau type-1" or "P-I" and is shown in Fig. 6.2.b.(i). With further increase of the field around $h = 3.5$, all the spin pairs are broken and the system goes to the FP phase.

The AAFM, Dimer, and SLFM phases are characterized by strong Heisenberg rung exchange J_q, leading to the formation of strong dimers on $S-S$ pairs, which are energetically more stable compared to the dimers of $\sigma - \sigma$ pairs interacting with Ising exchange. In the AAFM phase, with anisotropic antiferromagnetic spin alignment on the ladder for $J_q = 2.0$ and $J_d = 0.4$, a very small field $h_{c1} = 0.7$ is sufficient to break the $\sigma - \sigma$ pairs and reach the $m = 1/4$ plateau, as shown in Fig.**??**.(ii). In the $m = 1/4$ plateau of AAFM, the rung spins of $\sigma - \sigma$ pairs are fully polarized with a spin density of 0.5, as depicted in Fig.6.2.(a). The spin configuration of this type of magnetic phase is referred to as "m=1/4 plateau type-2" or "P-II" and is shown in Fig. 6.2.b.(ii).

In the Dimer phase, all the rung dimers are isolated, and the Ising dimers have a smaller spin gap as compared to the $S - S$ rung singlets. An external field of $h_{c1} = 0.5$ is sufficient to close the gap for a given value of $J_q = 2.0$ and $J_c = 1.0$ as shown in Fig.**??**.(iii). Due to the formation of perfect dimers through strong J_q exchange in this phase, the P-II phase exhibits a much larger gap, leading to a broader plateau width compared to the AAFM phase, as shown in Fig. **??**.(iii). In the SLFM phase, the ground state exhibits ferromagnetic spin arrangements along the leg, while spins on different legs are oppositely aligned. Fig. **??**.(iv) demonstrates that the onset of the P-II occurs at a field of $h_{c1} = 0.7$, with the

largest plateau width observed in this phase. The spin density analysis reveals that the dimers formed by $\sigma - \sigma$ pairs become polarized along the field direction in the P-II phase as shown in Fig.6.2.b.(ii). Similar to the AAFM phase, the $\sigma - \sigma$ rung dimers are weaker in this phase also, while the oppositely aligned legs enhance the stability of singlets on the Heisenberg pair $S - S$, resulting in an extended plateau width. With further increase in the applied field, the P-II plateau as shown in Fig.6.2.b.(ii) is disrupted, and a sharp jump occurs at $h_{c2} = 4.5$ and reaches the FP plateau. In all four phases, either all $S - S$ or all $\sigma - \sigma$ rung pairs are simultaneously disrupted, leading to magnetic jumps.

6.4.1.1 Quantum Fidelity and Bipartite Concurrence

The spin arrangement of the plateau phases is quite different for all four phases at $h = 0$. Therefore, we expect the wave function of the plateau phases should be different and can be understood from the perspective of quantum information theory. In this subsection, we calculate and show the zero temperature limit quantum fidelity and bipartite concurrence to analyze the plateaus, and these can be obtained from the partition function as discussed below. Quantum fidelity is the measurement of overlap between two states and can be used to characterize the phase transition on the tuning of parameters. Quan et. al. have shown that fidelity can be obtained from the partition function [282]. Similarly, we calculate the quantum fidelity for the field h with small perturbation δh as:

$$\mathcal{F}(h,\beta) = \frac{Q_4(h,\beta)}{\sqrt{Q_4(h+\delta h,\beta)Q_4(h-\delta h,\beta)}} \tag{6.10}$$

where $Q_4(h,\beta)$ is the partition function for one unit cell in this case. $\mathcal{F}(h,\beta)$ is unity when there is a unique state and discontinuous at the phase transition points. The Field fidelity susceptibility $\chi_{\mathcal{F}}(h,\beta) = \frac{\partial \mathcal{F}(h,\beta)}{\partial h}$ is zero in unique state and it diverges at the transition. $\mathcal{F}(h,\beta)$ can further be written in terms of the

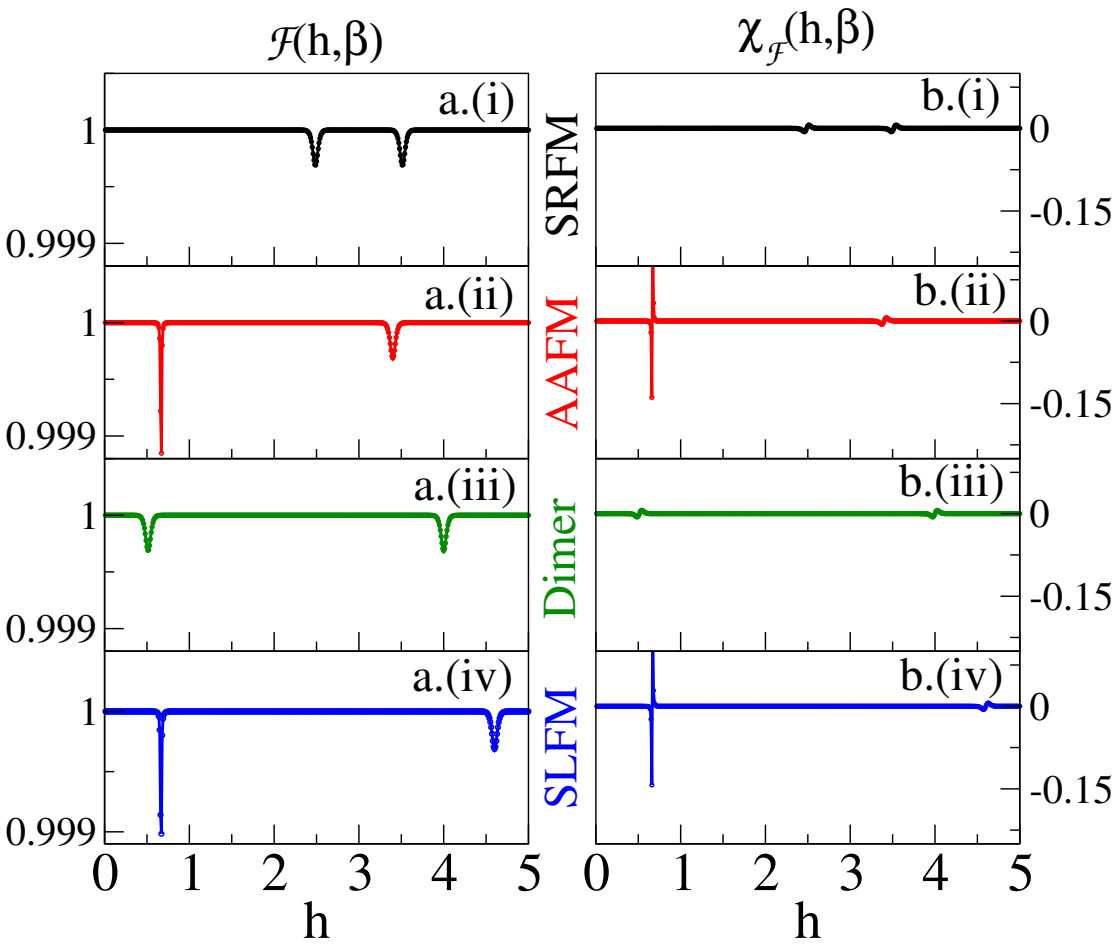

FIGURE 6.3: (a) (left column) Quantum fidelity $\mathcal{F}(h,\beta)$ and (b) (right column) fidelity susceptibility $\chi_{\mathcal{F}}(h,\beta)$ calculated using TM are shown for the thermodynamic limit ($N \to \infty$) at $T/J_c \to 0$. Black, red, green, and blue colors representing four phases: the SRFM ($J_q = 0.2$,$J_d = 2.0$), the AAFM ($J_q = 2.0$,$J_d = 0.4$), the Dimer ($J_q = 2.0$,$J_d = 1.0$), and the SLFM ($J_q = 2.0$,$J_d = 1.6$) respectively are arranged sequentially from top to bottom in both the columns.

free energy $F(h,\beta)$ and magnetic susceptibility $\chi(h,\beta)$ as

$$\begin{aligned}\mathcal{F}(h,\beta) &= e^{-\beta\left[F(h,\beta)-\frac{F(h-\delta h,\beta)+F(h+\delta h,\beta)}{2}\right]} \\ &\approx e^{-\left[\frac{(\beta\delta h)^2}{4}\chi(h,\beta)\right]}\end{aligned} \tag{6.11}$$

In the plateau phases, $\chi(h,\beta) = -\frac{\partial^2 F(h,\beta)}{\partial h^2} = \frac{\partial m}{\partial h}$ is zero and so the fidelity $\mathcal{F}(h,\beta)$ in Eq.6.11 is unity. On the other hand, at the magnetic jumps, the $\chi(h,\beta)$ diverges, and the $\mathcal{F}(h,\beta)$ decreases from unity.

Fig.6.3.a.[(i)-(iv)], and b.[(i)-(iv)] show the plot of $\mathcal{F}(h,\beta)$ (left column) and $\chi_{\mathcal{F}}(h,\beta)$ (right column) as a function of h respectively for four different phases:

(i) the SRFM, (ii) the AAFM, (iii) the Dimer, and (iv) the SLFM respectively. In each of the sub-figures of $\mathcal{F}(h,\beta)$ and $\chi(h,\beta)$, two discontinuities are noticed for all four phases. All of these discontinuities are consistent with the jumps of the $m-h$ curve in Fig.**??** and represent the magnetic phase transitions.

At the plateau phases, the partition functions are unique which results in fidelity to unity. However, at the discontinuities, the partition functions overlap and can be analyzed through the approximate expression of the fidelity as a function of the system parameters as following

$$\mathcal{F}(h,\beta) \approx \begin{cases} \frac{1}{\sqrt{\left[1+\frac{2b_0d_0e^{\beta h}\left(Cosh\left[\beta\delta h\right]-1\right)}{\left(b_0e^{\beta h}+d_0\right)^2}\right]}} & \text{for } h \approx h_{c1} \\ \frac{1}{\sqrt{\left[1+\frac{2a_0b_0e^{\beta h}\left(Cosh\left[\beta\delta h\right]-1\right)}{\left(a_0e^{\beta h}+b_0\right)^2}\right]}} & \text{for } h \approx h_{c2} \end{cases} \tag{6.12}$$

From the above expressions, it is clear that $Cosh\big[\beta\delta h\big] > 1$ and so the $\mathcal{F}(h,\beta) < 1$ at the transition points h_{c1} and h_{c2}.

We also calculate the bond order to understand the configurational change and bipartite concurrence to measure the quantum nature of the $S-S$ pair which is connected through a Heisenberg rung exchange J_q. If the concurrence has some finite value, the wavefunction is in a mixed or entangled state, otherwise, it is in a pure state if the concurrence is zero. Wooters et.al. and Karlova et. al. in their study calculate concurrence for a spin pair connected by Heisenberg interaction in terms of the local pair magnetization and spatial correlations: longitudinal, transverse to detect phase transitions at a finite temperature [280, 281]. In our study, we calculate the bipartite concurrence $\mathcal{C}(J_q,h)$ for the Heisenberg rung pair connected by exchange interaction J_q=(J_q^z, J_q^{xy}) in presence of the longitudinal field as

$$\mathcal{C}(J_q,h) = max\Big\{0, 4|c^T(J_q,h)| - 2\sqrt{[\frac{1}{4}+c^L(J_q,h)]^2 - \big[m'(J_q,h)\big]^2}\Big\} \tag{6.13}$$

Where, $m'(J_q,h)$, $c^L(J_q,h)$ and $c^T(J_q,h)$ are the pair magnetization, the longitudinal and transverse component of bond order respectively, and these can be defined as:

$$m'(J_q,h) = \frac{1}{2}\langle S^z_{2j,1} + S^z_{2j,2}\rangle = -\frac{1}{2}\frac{\partial F_1(h,h',\beta)}{\partial h'}, \tag{6.14}$$

$$c^L(J_q,h) = \langle S^z_{2j,1}S^z_{2j,2}\rangle = -\frac{1}{\beta}\frac{\partial[\ln Q_4(h,\beta)]}{\partial J^z_q}, \tag{6.15}$$

$$c^T(J_q,h) = \langle S^x_{2j,1}S^x_{2j,2}\rangle = -\frac{1}{2\beta}\frac{\partial[\ln Q_4(h,\beta)]}{\partial J^{xy}_q.} \tag{6.16}$$

Where, $F_1(h,h',\beta)$ is the free energy of one unit for which h,h' are the applied magnetic fields on the σ, S spins respectively. For the case, $h^{'} = h$, $F(h,\beta) = F_1(h,h',\beta)$. For a better understanding of the spin arrangement of the σ spins within the unit, we calculate the longitudinal bond order $c^L(J_c,h)$ for the $\sigma-\sigma$ and $c^L(J_d,h)$ for the diagonal $\sigma - S$ spin pairs as:

$$c^L(J_c,h) = \langle \sigma_{2j+1,1}\sigma_{2j+1,2}\rangle = -\frac{1}{\beta}\frac{\partial[\ln Q_4(h,\beta)]}{\partial J_c} \tag{6.17}$$

$$c^L(J_d,h) = \langle \sigma_{2j+1,1}S^z_{2j+1,2}\rangle = -\frac{1}{4\beta}\frac{\partial[\ln Q_4(h,\beta)]}{\partial J_d} \tag{6.18}$$

However, the $c^L(J_q,h)$, $c^T(J_q,h)$, and the $\mathcal{C}(J_q,h)$ are shown in Fig.6.4. (a), (b) and (c) respectively for all four phases (i) the SRFM, (ii) the AAFM, (iii) the Dimer, and (iv) the SLFM. Fig.6.4 can be analyzed separately for different GS phases by approximating the partition function $Q_4(h,\beta)$ of Eq.6.3, as we mentioned earlier in Sec.**??** that d_0, b_0, and a_0 can describe the $m = 0, 1/4$, and $1/2$ plateau phases respectively for different limits of exchange parameters J_q, J_d, and field h.

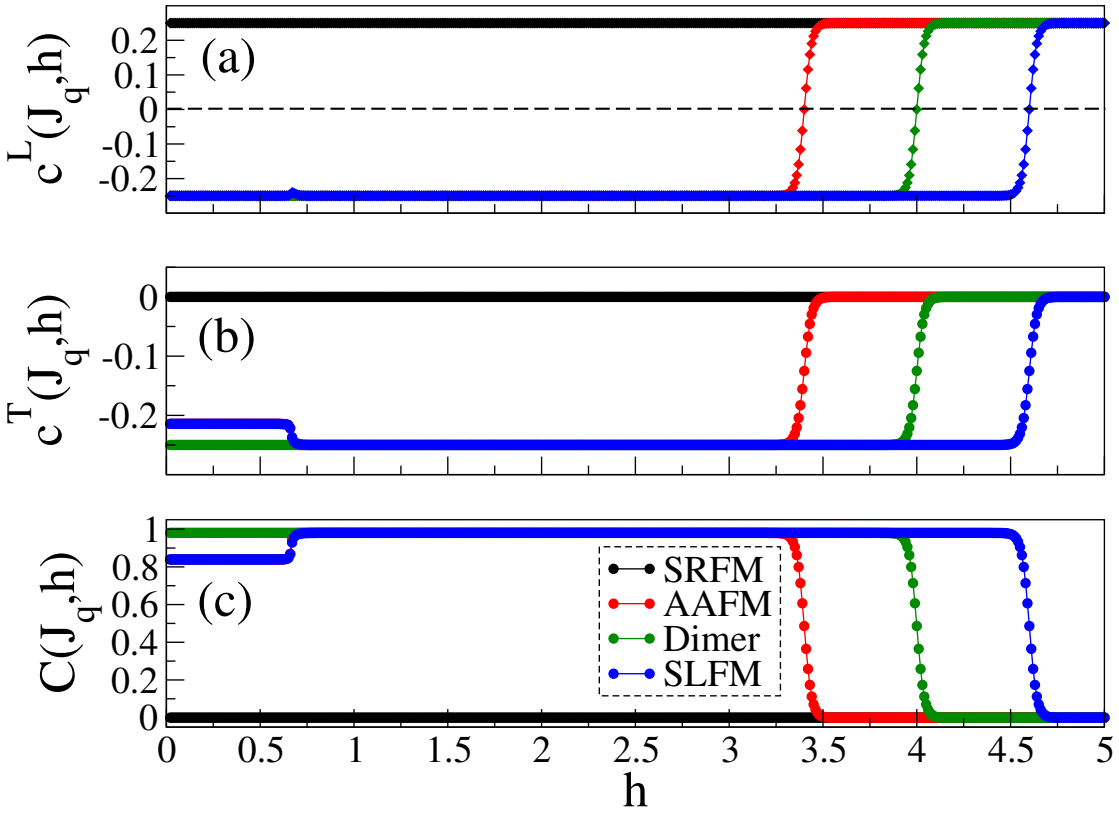

FIGURE 6.4: (a) Longitudinal bond order $c^L(J_q,h)$, (b) transverse bond order $c^T(J_q,h)$, (c) Quantum concurrence $\mathcal{C}(J_q,h)$ for the Heisenberg spin pair $S-S$ connected by rung strength J_q are shown as a function h. Black, red, green, and blue colors represent four phases: the SRFM ($J_q = 0.2$,$J_d = 2.0$), the AAFM ($J_q = 2.0$,$J_d = 0.4$), the Dimer ($J_q = 2.0$,$J_d = 1.0$), and the SLFM ($J_q = 2.0$,$J_d = 1.6$) respectively at $T/J_c = 0.02$.

The partition function for the SRFM phase having lower J_q and higher J_d can be written for three plateau phases: $m = 0, 1/4, 1/2$ as below-

$$Q_4(h,\beta) \approx \begin{cases} e^{-\frac{\beta}{4}(J_q^z + J_c - 4J_{cq} - 4J_d)} & \text{for } m = 0 \\ 4e^{-\frac{\beta}{4}(J_q^z - J_c - 4h)} & \text{for } m = 1/4 \\ e^{-\frac{\beta}{4}(J_q^z + J_c + 4J_{cq} + 4J_d - 8h)} & \text{for } m = 1/2 \end{cases} \tag{6.19}$$

In all of the plateaus, $c^L(J_q,h) = \frac{1}{4}$ and $c^T(J_q,h) = 0$ emphasizes the Ising dominance with the ferromagnetic alignment of the spins along the Heisenberg rung as shown in Fig.6.4.(a), and (b) respectively. The ferromagnetic alignment suggests $m^{'}(J_q,h) = \pm 1/2$ and so the Eq.6.13 demands the $\mathcal{C}(J_q,h)$ to be always zero, which in other words can be thought of as there is no quantum concurrence

or no quantum entanglement between the two S spins as shown in Fig.6.4. (c). It is to be noticed that $m^{'}(J_q, h) = \pm 1/2$ represents the P-I phase as shown in Fig.6.2.b.(i). It can now be stated that the P-I phase is a pure state.

For the other three phases: the AAFM, the Dimer, and the SLFM with sufficiently larger J_q, the magnetization can be analyzed from the $Q_4(h, \beta)$ for various limits of the system parameter Δ_2. We discuss the quantum concurrence for the plateau phases by writing down the partition functions separately.

(i) $m = 0$ plateau:

The partition function in this phase can be written as

$$Q_4(h, \beta) \approx$$
$$2e^{\frac{\beta(J_q^z + J_c)}{4}} \left[Cosh[\frac{\beta J_q^{xy}}{2}] + Cosh[\frac{\beta J_q^{xy} \Delta_2}{2}] \right] \tag{6.20}$$

The longitudinal bond order $c^L(J_q, h)$ in this case is $-1/4$ as shown in Fig.6.4.(a) whereas, the transverse bond order $c^T(J_q, h)$ is controlled by the interplay of the two terms in the partition function. For the Dimer phase ($\Delta_2 = 1$), the $c^T(J_q, h) = -1/4$, whereas, for the AAFM and SLFM phases ($\Delta_2 > 1$), $c^T(J_q, h)$ is less in magnitude as compared to the Dimer phase as shown in Fig.6.4. (b). The large transverse correlation along the Heisenberg spin pairs results in large $\mathcal{C}(J_q, h)$ close to unity for the AAFM and SLFM phases and it is maximum (unity) for the Dimer phase as shown in Fig.6.4.(c).

(ii) $m = 1/4$ plateau

The approximated partition function in this magnetic phase is

$$Q_4(h, \beta) \approx 2e^{\frac{\beta}{4}(J_q^z - J_c + 4h)} Cosh[\frac{\beta J_q^{xy}}{2}] \tag{6.21}$$

From the above partition function, one can obtain $c^L(J_c, h) = 1/4$, which implies the polarization of the σ spin pairs along the longitudinal field and it represents the P-II phase. In this plateau phase, the Heisenberg spin pairs have the longitudinal $c^L(J_q, h)$ and the transverse bond order $c^T(J_q, h)$ both as $-1/4$ and it is shown in Fig.6.4. (a), and (b). The maximum value of $c^T(J_q, h)$ in this phase results in

giving the maximum concurrence $\mathcal{C}(J_q, h)$ equal to unity for all the phases: (i) the AAFM, (ii) the Dimer, and (iii) the SLFM as shown in Fig.6.4. (c). The Eq.6.21 has no J_d dependence implying the Ising and HB rungs are isolated. From these results, one can remark that the P-II is maximally entangled due to the strong singlet formation along the HB rung.

(iii) $m = 1/2$ plateau

In this plateau phase, the partition function can be written as

$$Q_4(h, \beta) \approx e^{-\frac{\beta}{4}(J_q^z + J_c + 4J_{cq} + 4J_d - 8h)}, \tag{6.22}$$

which is the same as discussed before for the SRFM phase. The exponent of the partition function suggests that all the longitudinal bond orders $c^L(J_q, h), c^L(J_c, h)$, and $c^L(J_d, h)$ are $1/4$ and it is the signature of the FP phase with vanishing transverse bond order along the Heisenberg exchange J_q. The maximum longitudinal bond order and vanishing transverse bond order in the FP phase ensure that it is a pure state.

6.4.1.2 Quantum phase diagrams

In this section, we analyze the quantum phases as a function of J_d and J_q at different longitudinal magnetic fields $h = 0, 1, 2$, and 3. For the sake of completeness, we show the $h = 0$ quantum phases (i.e., the zero field GS phases), which are studied earlier in [1]. To characterize the quantum phases uniquely, we define the quantum phase index (QPI) which is a function of three different bond orders within the unit cell of the lattice and can be written as

$$\begin{aligned} &QPI = \\ &2Sign[c^L(J_q, h)] + Sign[c^L(J_d, h)] + Sign[c^L(J_c, h)] \end{aligned} \tag{6.23}$$

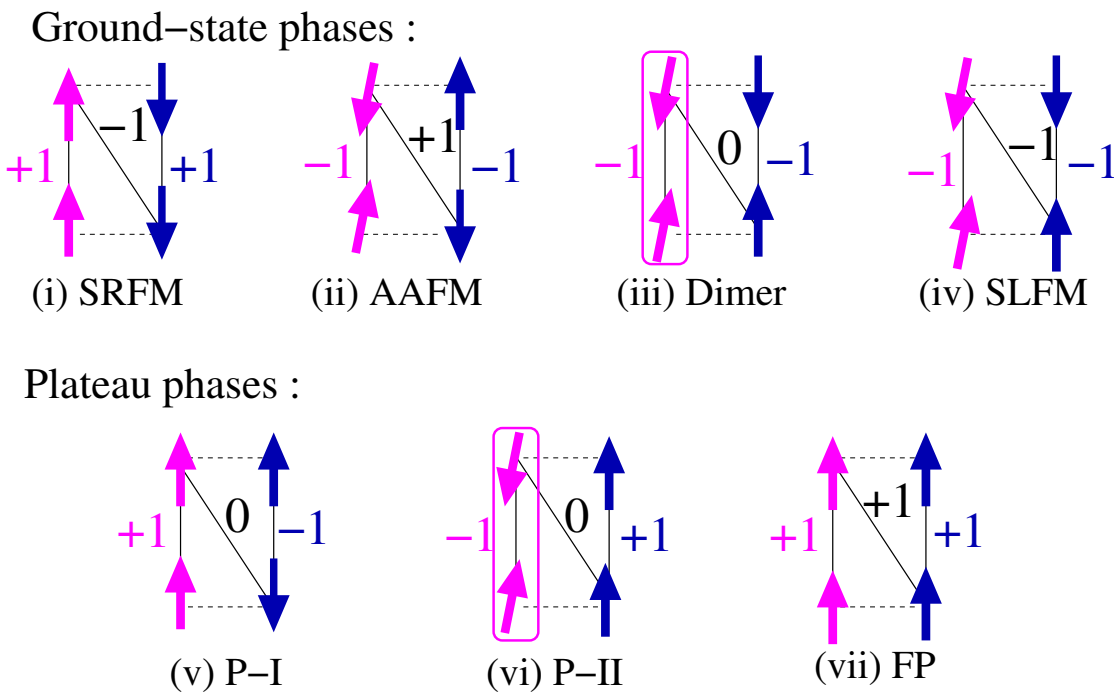

FIGURE 6.5: Schematics of the GS and the plateau phases are shown. Sign of the bond orders with exchange interactions J_q,J_d, and J_c are shown in magenta, black, and blue colors respectively. Boxes represent the perfect singlet Dimer formation.

Where $Sign[x]$ is the signum function and can be defined as

$$Sign[x] = \begin{cases} 1 & \text{for } x > 0 \\ 0 & \text{for } x = 0 \\ -1 & \text{for } x < 0 \end{cases} \tag{6.24}$$

The spin arrangements and the signum values of the longitudinal bond orders along Heisenberg rung $c^L(J_q, h)$, diagonal spin pair $c^L(J_d, h)$, and Ising rung $c^L(J_c, h)$ are shown for the quantum phases in Fig.6.5. The signum value of the bond orders and the corresponding unique QPI for different quantum phases are tabulated in Table.6.1.

We analyze different plateau phases in the plane of $J_q - J_d$ for different values of h as shown in Fig.6.6.(i)-(iv). As it is seen in Fig.6.6.(i), $h = 0$ phase diagram represents four GS phases: (i) the SRFM, (ii) the AAFM, (iii) the Dimer, and (iv)the SLFM with the four distinct QPI values as 2,-2,-3, and -4 respectively. Fig.

TABLE 6.1: Quantum Phase Index (QPI) for different phases.

Phases	$Sign$ $[c^L(J_q,h)]$	$Sign$ $[c^L(J_d,h)]$	$Sign$ $[c^L(J_c,h)]$	QPI
(i) SRFM	+1	-1	+1	2
(ii) AAFM	-1	+1	-1	-2
(iii) Dimer	-1	0	-1	-3
(iv) SLFM	-1	-1	-1	-4
(v) P-I	+1	0	-1	1
(vi) P-II	-1	0	+1	-1
(vii) FP	+1	+1	+1	4

6.6(ii) shows a few plateau phases along with the non-magnetic GS phases for the field $h = 1.0$. In this phase diagram, the P-I and P-II phases are shown with QPI numbers 1, and -1 respectively. With the low J_q value, the SRFM phase transit to P-I, whereas, in the vicinity of the SRFM-SLFM phase boundary, the regime with comparable J_q and J_d transit to P-II phase which is interesting and can be analyzed by writing down the critical fields for different limits of J_q. The spin gap or the critical field h_{c1} for the SRFM phase in different J_q limits can be obtained as

$$h_{c1} \approx \begin{cases} (J_d + 1/2) & \text{for } J_q < J_c \\ (1 + J_d - \frac{J_q^z}{2} - \frac{J_q^{xy}}{2}) & \text{for } J_q > J_c \end{cases} \tag{6.25}$$

From the above equation, by considering $h_{c1} = 1$, the phase boundaries between the SRFM-P-I and the SRFM-P-II phases can be obtained as $J_d = 0.5$ and $J_d \approx J_q$ respectively and these boundaries are noticed in Fig.6.6. (ii).

Similarly, the spin gap h_{c1} for the AAFM, the Dimer, and the SLFM phases can be written as a function of J_q and Δ in the following manner

$$h_{c1} \approx \frac{1}{2} + \frac{1}{\beta} ln\big[1 + \frac{Cosh[\frac{\beta J_q^{xy} \Delta_2}{2}]}{Cosh[\frac{\beta J_q^{xy}}{2}]}\big] \tag{6.26}$$

The critical fields h_{c1} in Fig.**??**. (ii)-(iv) for the AAFM (0.7), the Dimer (0.5), and the SLFM (0.7) phases agree well with the above equation. Also, from the Eq.6.26, one can determine the phase boundaries between the AAFM-P-II, and the SLFM-P-II as a function of system parameters J_q, J_d or Δ_2. However, the

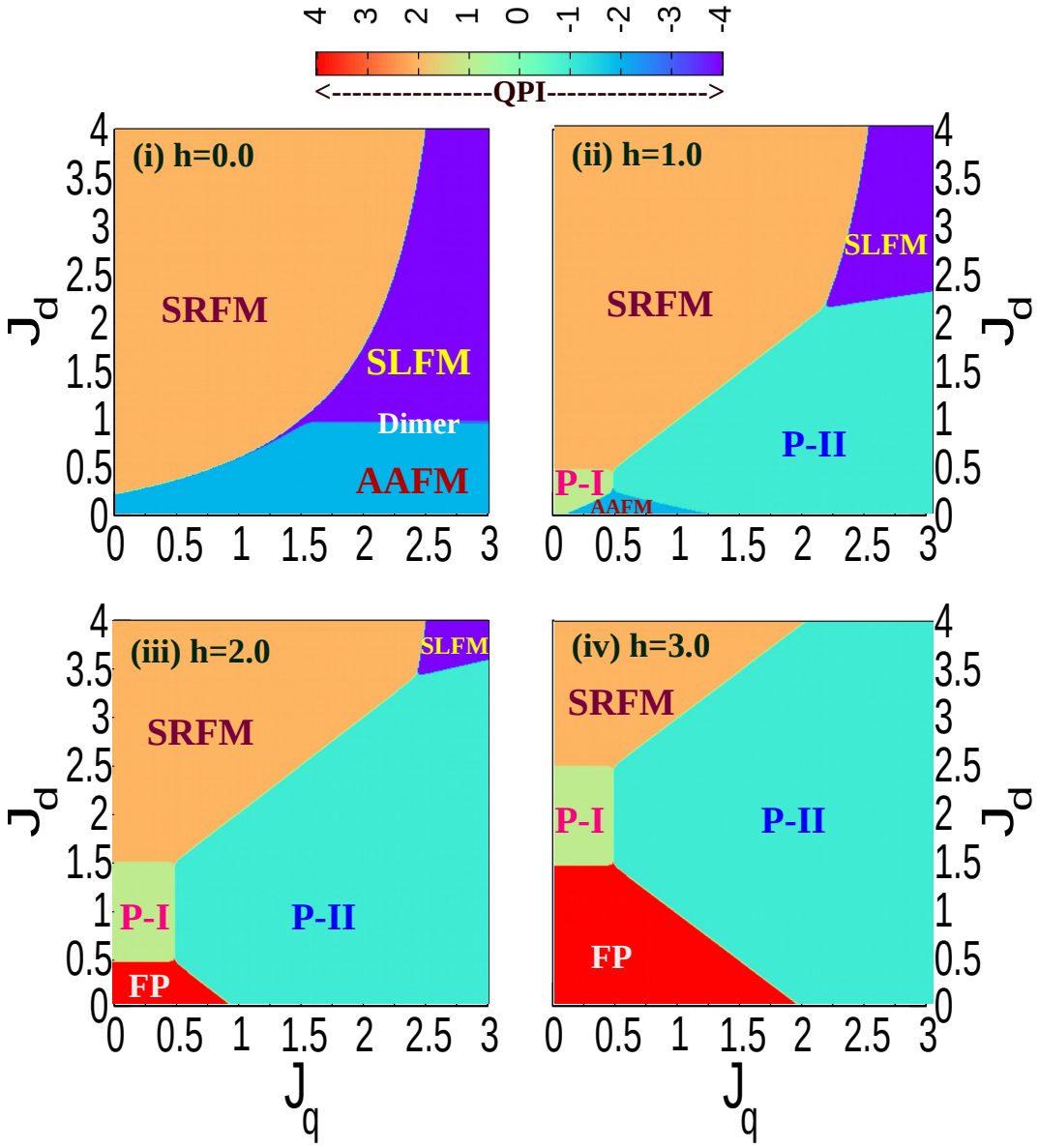

FIGURE 6.6: Quantum Phase Index (QPI) is shown for five longitudinal fields $h = 0, 1, 2, 3$ from (i)-(iv) in sequence. The color bar shows the QPI as defined in Eq.6.23. The QPI values $2, -2, -3, -4, 1, -1, 4$ represent quantum phases: the SRFM, the AAFM, the Dimer, the SLFM, the P-I, the P-II, and the FP phases respectively.

major part of the parameter space in Fig.6.6. (iii) is occupied by P-II due to the low spin gap in the AAFM, the Dimer, and the SLFM phases. In Fig. 6.6(iii), the P-II occupies the largest area and replaces the AAFM phase completely for the field $h = 2$. A small area of the FP phase emerges in this case for very small values of J_q and J_d in Fig.6.6.(iii).

The FP phase appears either from the P-I or P-II phase on the application of the critical field h_{c2}. This critical field can be written as a function of the system parameters in the following way

$$h_{c2} \approx \begin{cases} (J_d + 3/2) & \text{for P-I phase} \\ \frac{(J_q^z + 2J_d + 2)}{2} + \frac{1}{\beta} ln\big[Cosh[\frac{\beta J_q^{xy}}{2}]\big] & \text{for P-II phase} \end{cases} \tag{6.27}$$

From the above equation, by taking $h_{c2} = 2$, one can determine the phase boundary between the P-I-FP phase as $J_d = 1/2$. Similarly, the P-II-FP phase boundary can also be obtained from the above equation. For $h = 3$ in 6.6. (iv), the SLFM phase is replaced by P-II, whereas, for the large J_d value, the SRFM phase still exists in the magnetic phase diagram due to the largest spin gap $h_{c2} = (J_d + 3/2)$ as in Eq.6.27. With an even larger field value, all other phases vanish and the FP phase occupies the phase diagram completely.

6.4.2 Magnetization process in the presence of a transverse field

Using many experimental techniques in general, this kind of system is synthesized in powder form or single crystal form and so to understand the directional dependence of the field on the magnetization, we study the effect of the transverse field h^x in our model [259, 260]. In the presence of h^x, the Hamiltonian of different units do not commute to each other, and therefore, the TM method never works, we use the ED method to show the finite size scaling of magnetization for three system sizes and then analyze the spin density for $N = 24$.

6.4.2.1 Transverse component of magnetization

It is to be mentioned that all four GS phases are in the $S^z = 0$ sector, and so it does not change the longitudinal but rather the transverse component of magnetization on the application of an external transverse field h^x. We calculate the transverse

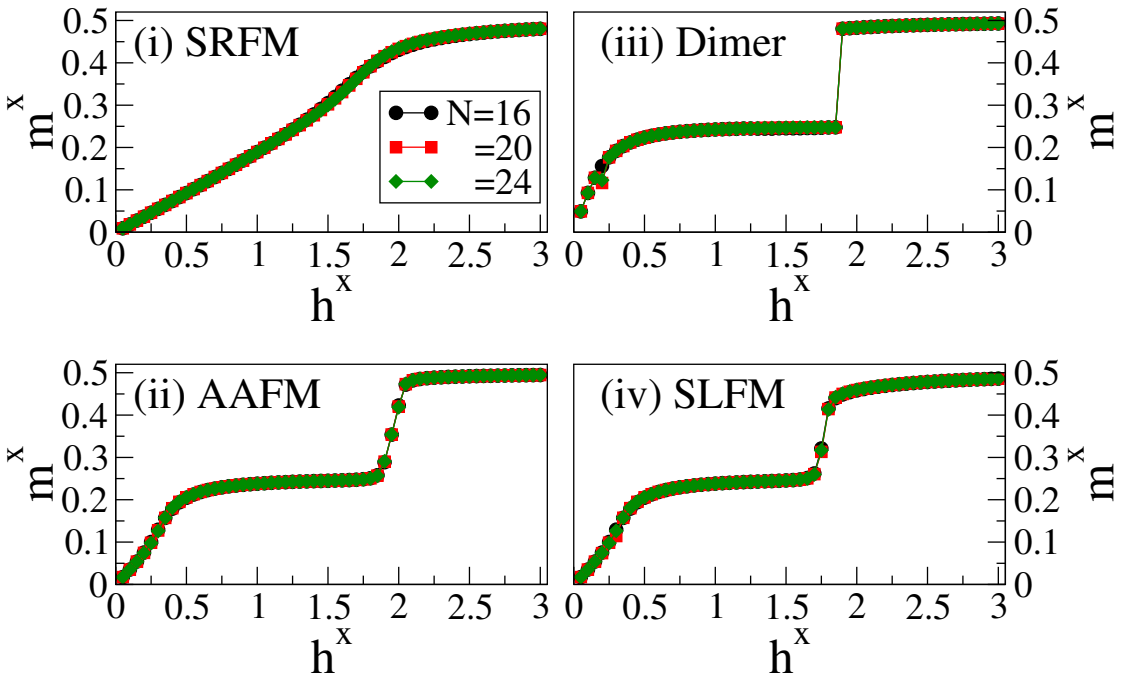

FIGURE 6.7: Transverse magnetization m^x is shown as a function of the transverse field h^x for four phases: (i) SRFM ($J_q = 0.2$, $J_d = 2.0$), (ii) AAFM ($J_q = 2.0$, $J_d = 0.4$) (iii) Dimer ($J_q = 2.0$, $J_d = 1.0$), and (iv) SLFM ($J_q = 2.0$, $J_d = 1.6$). Black, red, and green colors represent the system sizes $N = 16, 20,$ and 24 respectively.

magnetization m^x in terms of spin density $\langle S_i^x \rangle$ at each site i as-

$$m^x = \frac{1}{N} \sum_{i=1}^{N} \langle S_i^x \rangle \tag{6.28}$$

In Fig.6.7[(i)-(iv)], we show the transverse (along $+x$ direction) magnetization for all four phases: (i) the SRFM, (ii) the AAFM, (iii) the Dimer, and (iv) the SLFM with the corresponding set of chosen J_q, J_d values as in section **??** for the system sizes $N = 16, 20,$ and 24. In the SRFM phase, the m^x shows continuous variation with the field h^x up to saturation value. In this phase, the GS has Ising bond dominance for all the spins, and therefore the spins along the x-direction get smoothly oriented along the field. In the AAFM phase, the curve increases smoothly and then it shows a $m^x \approx 1/4$ plateau-like behavior in the range $0.45 < h^x < 1.75$, and afterward it jumps to full saturation. A similar behavior is noticed in the Dimer phase as well in which the plateau onsets at a field $h^x = 0.4$. In this case, the jump from the $m^x = 1/4$ plateau to saturation is much faster than

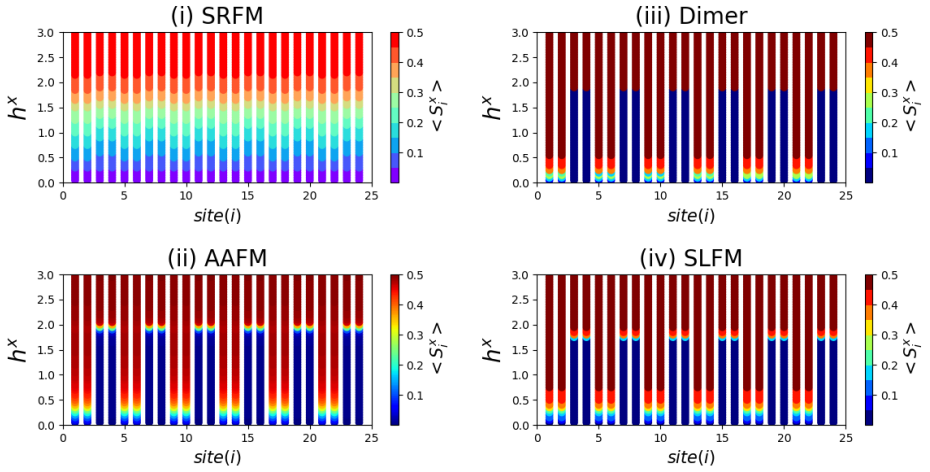

FIGURE 6.8: Transverse component of spin density $\langle S_i^x \rangle$ at each site i for for four phases: (i) SRFM ($J_q = 0.2$, $J_d = 2.0$), (ii) AAFM ($J_q = 2.0$, $J_d = 0.4$) (iii) Dimer ($J_q = 2.0$, $J_d = 1.0$), and (iv) SLFM ($J_q = 2.0$, $J_d = 1.6$) are shown for system size $N = 24$. Along the horizontal axis, the site index i for each spin is shown. Along the vertical axis, the transverse field h^x is varied. The color bar shown in all subfigures represents the amplitude of $\langle S_i^x \rangle$ and it varies from 0 to 0.5 for spin-1/2 systems.

in the case of the AAFM phase. In the SLFM phase for $h^x < 0.7$, m^x increases smoothly, and then it forms the plateau-like structure for $0.7 < h^x < 1.7$. It shows a sudden jump almost around $h^x = 1.75$ and slowly reaches saturation magnetization for higher h^x. From all the subfigures, it is noticed that there is a negligibly small finite-size effect. In the next subsection, we analyze the $m^x = 1/4$ plateau mechanism for all the phases based on the spin density.

6.4.2.2 Transverse component of spin density

For a more detailed understanding, we show the color map of the spin density $\langle S_i^x \rangle$ in all four phases for $N = 24$. It is to be mentioned that the $\sigma - \sigma$ and $S - S$ pairs alternate with site index i. To be more specific, $\sigma - \sigma$ pairs take the site indices [1,2,5,6,....] whereas, $S - S$ pairs take the indices [3,4,7,8....] as shown in all subfigures of Fig.6.8. In Fig.6.8.(i), $\langle S_i^x \rangle$ varies continuously as h^x increases for all the sites. As the GS of the SRFM has only Ising interactions dominance and there is no transverse spin correlation, all the spins continuously get oriented along h^x in this phase. In the AAFM phase, the $S - S$ pair has a

strong transverse spin correlation whereas, the $\sigma - \sigma$ rung pairs are weak and are aligned continuously with an increase in h^x as shown in the color map Fig.6.8. (ii). Saturation is attained by an even further increase of field when it breaks the strong $S - S$ pair at $h^x = 1.75$. As shown in Fig.6.8. (iii) for the Dimer phase, the continuous increase of m^x is similar to the AAFM phase but a sudden jump at $h^x = 1.7$ is noticed because of unbinding of the perfect $S - S$ singlet pairs. Fig.6.8.(iv) shows $\langle S_i^x \rangle$ for the SLFM phase. As in the GS of this phase, both the Ising pairs and Heisenberg pairs are aligned parallel but spins of opposite legs are aligned oppositely, with the increase in h^x, it is noticed that all the Ising dimer pairs are continuously broken until the magnetization reaches to 1/4. An even further increase in h^x does not easily close the spin gap and results in a large $m^x = 1/4$ plateau until a field $h^x = 1.75$ is applied to break the Heisenberg rung $S - S$ pairs.

6.5 Summary

In this paper, we study the effect of external magnetic field on the GS phases of Hamiltonian in Eq.6.1 of a frustrated spin-$\frac{1}{2}$ two-leg ladder with alternate Ising and Heisenberg type of rung and Ising type of interaction in the leg and diagonal. This model has a few similarities to one of the earlier studied models where leg and diagonal exchanges are Ising type but all the rung exchanges are Heisenberg type in which on applying the magnetic field, a magnetic phase SB appears [98]. In our model, alternate rungs are Ising-Heisenberg type due to which the zero field GS phases and the plateau phases depend upon the competing Ising and Heisenberg rung exchanges as well. Tuning of the exchange parameters in the model Hamiltonian can give rise to four GS phases: (i) the SRFM, (ii) the AAFM, (iii) the Dimer, and (iv) the SLFM, whose spin arrangements are schematically represented in Fig.6.1.b. [(i)-(iv)]. We analyzed the magnetization behavior in the presence of external magnetic fields: longitudinal and transverse.

In the presence of the longitudinal magnetic field h, the GS shows three magnetic plateaus: the first one is due to the finite spin gap, the second plateau at $m = 1/4$ is formed due to the polarization of either Ising or Heisenberg type of rung spin dimers along the field. This can be of two types as shown in Fig.6.2.b. In the SRFM phase, the Heisenberg rung spin pairs $S - S$ are polarized giving rise to "$m = 1/4$ plateau type-1" or "P-I" phase as shown in Fig.6.2.b.(i). But for the other three zero field GS phases: the AAFM, the Dimer, and the SLFM, the $\sigma - \sigma$ spins are polarized at $m = 1/4$ and give rise to "$m = 1/4$ plateau type-2" or "P-II" phase as shown in Fig.6.2.b.(ii). In the presence of a large external field in all phases, all of the spins are completely polarized along the field and form the third plateau at the saturation magnetization $m = 1/2$ which is named FP. The $m = 1/4$ plateau width is sensitive to the parameter values as obtained in Eq.6.7. We also notice that two plateaus are connected by jumps in the magnetization curve and this is because of the unpairing of either all $S - S$ (for P-I) or all $\sigma - \sigma$ (for P-II) rung dimers.

To understand the quantum nature of the wave function of the GS, we calculate the quantum fidelity and quantum concurrence in the presence of a longitudinal field. In all four phases, fidelity shows deviation from unity at the critical fields of magnetic phase transitions as shown in Fig.6.3. We note that the discontinuities in fidelity represent the overlap of the plateau phases. The quantum concurrence shown in Fig.6.4.c measures the entanglement between two spins at the Heisenberg rung. The concurrence is always zero as a function of the field for the SRFM phase, and it means that the SRFM phase is a pure state. Whereas, in other phases: the AAFM, the Dimer, and the SLFM, the concurrence has a finite value both at $m = 0$. In the $m = 0$ plateau phase, the concurrence is a function of the exchange interactions for the AAFM, and the SLFM phases and it is maximum for the Dimer phase. The concurrence is zero for the P-I phase and FP phase. Whereas it is maximum for the P-II phase as it forms the isolated singlet Dimers along the Heisenberg rung. So, one can state that the P-II phase is maximally entangled, whereas, P-I and FP phases are the pure states. However, all of the jumps in the

magnetization can be indirectly predicted based on the jumps in concurrence as shown in Fig.6.4.c.

We define QPI to uniquely identify the quantum phases in the exchange parameter J_q-J_d plane for a finite longitudinal field h. The unique QPI values for different quantum phases are tabulated in Table.6.1. The effect of the longitudinal magnetic field on the GS phases is shown in Fig.6.6.[(i)-(iv)]. For a sufficiently larger longitudinal field $h = 1.0$, the Dimer phase disappears, and two types of $m = 1/4$ plateaus: P-I, P-II appear. At a very large field $h = 3.0$, it is noticed that the P-I, P-II, and FP phases dominate in the phase diagram. The phase boundaries among the quantum phases can easily be obtained from the analytical expression of the critical fields of phase transitions.

In the SRFM phase, spin alignments are along the z direction and there is weak exchange interaction along the +x direction in the Heisenberg rung dimers, therefore, magnetization m^x shows a continuous variation till saturation on the application of a transverse field. In other phases: the AAFM, the Dimer, and the SLFM, the magnetization process can be understood in terms of two sublattice behaviors. The sublattice with $\sigma - \sigma$ dimer is paramagnetic along x, whereas, in the other sublattice, the Heisenberg spin pair $S - S$ dimer has a strong transverse exchange component which induces a finite spin gap in the system. As a consequence, at a lower value of the transverse field, the system shows a continuous behavior in the magnetization curve due to gradual change of m^x of $\sigma - \sigma$ spins up to $m^x = 1/4$ with an increase in h^x as shown using spin density in Fig.6.8.[(ii)-(iv)]. With further increase in field, at a critical value, the magnetization curve shows a sudden jump from $m^x \approx 1/4$ to $1/2$ for the three phases: the AAFM, the Dimer, and the SLFM, and this phase transition seems to be of the first order. The plateau width is sensitive to the set of parameters or the set of exchange interactions J_q and J_d in the presence of a transverse field also.

In conclusion, this model system is unique because of the alternate Ising-Heisenberg rung exchange and gives many insightful mechanisms of the plateau and jumps

both in the presence of longitudinal and transverse fields. The magnetic properties of such systems can be utilized in designing quantum switches, magnetic memories, and other similar devices. Also, these systems might have tremendous applications in quantum information processing and quantum computation because of the entangled states.

6.6 Appendix 1

The partition function in presence of a longitudinal field h for N sites, $Q_N(h,\beta)$ with Hamiltonian H can be written as-

$$Q_N(h,\beta) = Tr\left(e^{-\beta \mathbf{H}}\right) \tag{6.29}$$

where, Tr means trace of the matrix, $\beta = 1/\left(k_B T\right)$ and k_B is the Boltzmann constant. Using explicit configuration basis for the system, Eq. 6.29 is rewritten in the following form,

$$Q_N(h,\beta) = \sum_{\{\sigma,S\}} < \cdots, \sigma_{2j-1,1}, \sigma_{2j-1,2}, S_{2j,1}, S_{2j,2}, \cdots | \\ e^{-\beta \mathbf{H}} \mid \cdots, \sigma_{2j-1,1}, \sigma_{2j-1,2}, S_{2j,1}, S_{2j,2}, \cdots >$$

Here the summation is over all possible configurations $\{\sigma, S\}$ of the system. For a given configuration, $|\cdots, \sigma_{2j-1,1}, \sigma_{2j-1,2}, S_{2j,1}, S_{2j,2}, \cdots >$ represents a basis state. In our case, the system is composed of $n = N/4$ units, and for each unit, the Hamiltonian is written in Eq.6.1. The partition function of the entire ladder can be written as:

$$Q_N(h,\beta) = \sum_{\sigma} < \cdots, \sigma_{2j-1,1}, \sigma_{2j-1,2}, \cdots | \prod_{j=1}^{n} \mathbf{T}_j \mid \cdots, \sigma_{2j-1,1}, \sigma_{2j-1,2}, \cdots >$$

where $T_i = \sum_{\{S\}_i} < S_{2i,1}, S_{2i,2} \mid e^{-\beta \mathbf{H_i}(\sigma,S)} \mid S_{2i,1}, S_{2i,2} >$ is well-known transfer matrix operator for each unit. Here the summation is over $\{S\}_i$ which represents all possible configurations of spins $S_{2i,1}$ and $S_{2i,2}$ (from the i^{th} unit). It may be noted that T_i does not contain the components of spin S operators and it has only σ variables, namely, $\sigma_{2i-1,1}, \sigma_{2i-1,2}, \sigma_{2i+1,1}$ and $\sigma_{2i+1,2}$. Since, the Hamiltonians of each unit commute to each other, introducing identity operators $I = \sum_{\{\sigma\}_i} |\sigma_{2i-1,1}, \sigma_{2i-1,2} >< \sigma_{2i-1,1}, \sigma_{2i-1,2}|$ between successive $\mathbf{T}$ operators, we can finally write the partition function as the trace of the n-th power of a small (4×4) transfer matrix $\mathbf{P}$. We have,

$$Q_N(h, \beta) = Tr(\mathbf{P}^n),$$

The elements of the transfer matrix are given by

$$P_{(\sigma_{2i-1,1},\sigma_{2i-1,2}),(\sigma_{2i+1,1},\sigma_{2i+1,2})} =< \sigma_{2i-1,1}, \sigma_{2i-1,2} \mid \mathbf{T}_i \mid \sigma_{2i+1,1}, \sigma_{2i+1,2} > \quad (6.30)$$

Before we construct and diagonalize the $\mathbf{P}$ matrix, we first need to carry out the trace over the configurations $\{S\}_i$ to find out the form of $\mathbf{T}_i$. Since $\mathbf{T}_i = \sum_{\{S\}_i} < S_{2i,1}, S_{2i,2} \mid e^{-\beta \mathbf{H_i}(\sigma,S)} \mid S_{2i,1}, S_{2i,2} >$, if we take the eigenstate basis of $\mathbf{H}_i$, we will get $\mathbf{T}_i$ as the summation over exponential of eigenvalues of $-\beta \mathbf{H}_i$. Next, we calculate the eigenvalues of $\mathbf{H}_i$ operator.

By considering,

$a = J_d \left(\sigma^z_{2j-1,2} + \sigma^z_{2j+1,2}\right) + J_{cq} \left(\sigma^z_{2j-1,1} + \sigma^z_{2j+1,1}\right) + h$

$b = J_d \left(\sigma^z_{2j-1,1} + \sigma^z_{2j+1,1}\right) + J_{cq} \left(\sigma^z_{2j-1,2} + \sigma^z_{2j+1,2}\right) + h$

$c = \frac{J_c}{2} \left(\sigma^z_{2j-1,1}\sigma^z_{2j-1,2} + \sigma^z_{2j+1,1}\sigma^z_{2j+1,2}\right)$

$d = \frac{h}{2} \left(\sigma^z_{2j-1,1} + \sigma^z_{2j-1,2} + \sigma^z_{2j+1,1} + \sigma^z_{2j+1,2}\right),$

$f = c + d$

Hamiltonian (Eq. 6.1) for the j^{th} geometrical unit can be written as-

$$\mathbf{H_j} = \frac{J^{xy}_q}{2} \left(S^+_{2j,1}S^-_{2j,2} + S^-_{2j,1}S^+_{2j,2}\right) + J^z_q \left(S^z_{2j,1}S^z_{2j,2}\right) + aS^z_{2j,1} + bS^z_{2j,2} + f$$

We can write down the following Hamiltonian matrix in the eigenstate basis of

$S^z_{2j,1}S^z_{2j,2}$ operator,

$$H_j = \begin{bmatrix} \frac{J^z_q}{4} + \frac{(a+b)}{2} + f & 0 & 0 & 0 \\ 0 & \frac{-J^z_q}{4} + \frac{(a-b)}{2} + f & \frac{J^{xy}_q}{2} & 0 \\ 0 & \frac{J^{xy}_q}{2} & \frac{-J^z_q}{4} - \frac{(a-b)}{2} + f & 0 \\ 0 & 0 & 0 & \frac{J^z_q}{4} - \frac{(a+b)}{2} + f \end{bmatrix}.$$

The Hamiltonian matrix comes up with its four eigenvalues from three S^z_{SS} sectors based on S-S pairs-

(i) From $S^z_{SS} = 1$ sector (formed by S-S pair)

$\theta_1 = (f + \frac{J^z_q}{4}) + \frac{(a+b)}{2}$

(ii) From $S^z_{SS} = -1$ sector (formed by S-S pair)

$\theta_2 = (f + \frac{J^z_q}{4}) - \frac{(a+b)}{2}$

(iii) From $S^z_{SS} = 0$ sector (formed by S-S pair)

$\theta_3 = (f - \frac{J^z_q}{4}) + \frac{\sqrt{(J^{xy}_q)^2+(a-b)^2}}{2}$

$\theta_4 = (f - \frac{J^z_q}{4}) - \frac{\sqrt{(J^{xy}_q)^2+(a-b)^2}}{2}$.

We note that the eigenvalues ($\theta_{k'}$) are functions of σ variables, namely $\sigma_{2j-1,1}$, $\sigma_{2j-1,2}$, $\sigma_{2j+1,1}$ and $\sigma_{2j+1,2}$. Using these eigenvalues, we rewrite $\mathbf{T}_j$ as,

$$\begin{aligned} \mathbf{T}_j &= \sum_{\{S\}_j} < S_{2j,1}, S_{2j,2} \mid e^{-\beta \mathbf{H_j}(\sigma,S)} \mid S_{2j,1}, S_{2j,2} > \\ &= \sum_{k'=1}^{4} e^{-\beta\theta'_k}. \end{aligned}$$

$$= 2e^{-\beta f}\Bigg[e^{-\frac{\beta J_q^z}{4}} Cosh\Big(\frac{\beta(a+b)}{2}\Big) + e^{\frac{\beta J_q^z}{4}} Cosh\Big(\frac{\beta J_q^{xy}}{2}\sqrt{1+\frac{(a-b)^2}{(J_q^{xy})^2}}\Big)\Bigg]$$

Further, we consider- $e^{\frac{\beta J_q^z}{4}} = Q$, $e^{\frac{\beta J_c}{4}} = C$,
$e^{\frac{\beta h}{4}} = H$, $\frac{(J_{cq}+J_d)}{2} = X$, $\frac{(J_{cq}-J_d)^2}{(J_q^{xy})^2} = Y$,
and also, $\Delta_1 = \sqrt{1+Y}$, $\Delta_2 = \sqrt{1+4Y}$.
The Transfer matrix for one unit becomes -

$$\mathbf{P} = \begin{bmatrix} p & q & q & r \\ q & s & u & v \\ q & u & s & v \\ r & v & v & w \end{bmatrix}.$$

Where,

$$p = 2e^{-\beta(J_c/4+h)} \times \Big[Q^{-1}Cosh\big(\beta(2X+h)\big) + QCosh\big(\frac{\beta J_q^{xy}}{2}\big)\Big]$$

$$q = 2e^{-\beta(h/2)} \times \Big[Q^{-1}Cosh\big(\beta(X+h)\big) + QCosh\big(\frac{\beta J_q^{xy}\Delta_1}{2}\big)\Big]$$

$$r = 2e^{-\beta(J_c/4)} \times \Big[Q^{-1}Cosh\big(\beta h\big) + QCosh\big(\frac{\beta J_q^{xy}}{2}\big)\Big]$$

$$s = 2e^{\beta(J_c/4)} \times \Big[Q^{-1}Cosh\big(\beta h\big) + QCosh\big(\frac{\beta J_q^{xy}\Delta_2}{2}\big)\Big]$$

$$u = 2e^{\beta(J_c/4)} \times \Big[Q^{-1}Cosh\big(\beta h\big) + QCosh\big(\frac{\beta J_q^{xy}}{2}\big)\Big]$$

$$v = 2e^{\beta(h/2)} \times \Big[Q^{-1}Cosh\big(\beta(-X+h)\big) + QCosh\big(\frac{\beta J_q^{xy}\Delta_1}{2}\big)\Big]$$

$$w = 2e^{-\beta(J_c/4-h)} \times \Big[Q^{-1}Cosh\big(\beta(-2X+h)\big) + QCosh\big(\frac{\beta J_q^{xy}}{2}\big)\Big]$$

From $|P - \lambda I_4| = 0$, we get the eigenvalues in the form of

$$\boxed{\lambda_4 = (s-u)}$$
$$\boxed{\lambda^3 - B_0\lambda^2 - C_0\lambda + D_0 = 0} \tag{6.31}$$

Here, λ_4 is one of the eigenvalues, whereas, the other three come from Eq.6.31. The coefficients of the equation are defined as:

$$B_0 = (s+u+w)$$
$$C_0 = [2(q^2+v^2-\frac{r^2}{2}) - pw + (p-w)(s+u)]$$
$$D_0 = [4qrv - 2pv^2 - 2q^2w + pw^2 - (s+u)(r^2+pw)]$$

For the polynomial equation 6.31, the eigenvalues λ_i satisfy the relations-

$$\sum_{i=1}^{3}\lambda_i = B_0, \sum_{i=1}^{3}\lambda_i\lambda_{i+1} = -C_0 \tag{6.32}$$

Now, let us make a very reasonable assumption to make the calculation easy. We assume, $\lambda_1 \gg \lambda_2 \gg \lambda_3$ are in descending order and λ_3 has the least contribution in the partition function so that Eq.6.32 can approximately be written as:

$$\lambda_1 + \lambda_2 = B_0, \lambda_1\lambda_2 = -C_0 \tag{6.33}$$

The Eq. 6.33 leads us to getting other two eigenvalues:

$$\begin{aligned} &\lambda_{1,2}^2 - B_0\lambda_{1,2} - C_0 = 0 \\ &\boxed{\implies \lambda_{1,2} = \frac{B_0 \pm \sqrt{B_0^2+4C_0}}{2}} \end{aligned} \tag{6.34}$$

We find Eq. 6.34 becomes much more simpler with further approximation in $\beta \to \infty$ limit as-

$$\begin{aligned} \lambda_1 &= (w + s + u) \\ &= 2e^{\frac{-\beta(J_c-4h)}{4}}\left[Q^{-1}Cosh[\beta(h-2X)] + QCosh[\frac{\beta J_q^{xy}}{2}]\right] \\ &+ \left[2Q^{-1}Cosh[\beta h] + QCosh[\frac{\beta J_q^{xy}}{2}] + QCosh[\frac{\beta J_q^{xy}\Delta_2}{2}]\right] \\ &\times 2e^{\frac{\beta(J_c)}{4}} \end{aligned} \tag{6.35}$$

$Q_N(h,\beta)$ takes the form as

$Q_N(h,\beta) = [\lambda_1 + \lambda_2 + \lambda_3 + \lambda_4]^n$

For $n \to \infty$, and λ_1 being the largest, the partition function for the entire system and one unit become $Q_N(h,\beta) \approx \lambda_1^n$ and $Q_4(h,\beta) \approx \lambda_1$ respectively.

Chapter 7

Symmetry broken phases and probable quantum spin liquid in a pyrochlore ladder

7.1 Introduction

In condensed matter physics, the pyrochlore lattice refers to a specific arrangement of atoms or ions in a crystal structure and this lattice structure is commonly found in certain materials, particularly in certain rare-earth and transition-metal compounds [285–287]. The pyrochlore lattice is characterized by a network of interconnected tetrahedrons. There are five major key features in the pyrochlore lattice. First, it generally exists on a tetrahedral geometry where the crystal structure consists of a corner-sharing tetrahedron, and each vertex of the tetrahedron is typically occupied by an atom or ion as shown in Figure xx. Second these systems are frustrated due to the geometric arrangement of the localized spin and the geometric frustration in the spins arises when interactions between neighboring particles cannot be simultaneously satisfied. This frustration can lead to a complex and interesting ground-state magnetic phase. In many cases, these systems are often studied in the context of quantum spin systems and their topological nature

of the ground state phases. The spin-ice arrangement of spin in the ground state is one of the key features of various materials like $Ho_2Ti_2O_7$ and $Dy_2Ti_2O_7$ which are rare-earth pyrochlores are classic examples of spin ice materials [287, 288]. The magnetic ions (holmium or dysprosium) on the pyrochlore lattice behave like magnetic monopoles and exhibit interesting magnetic properties [289]. $Yb_2Ti_2O_7$ has been studied for its potential to host a quantum spin liquid state on the pyrochlore lattice [290, 291] and $Cd_2Os_2O_7$ compound is known for its topological properties on the pyrochlore lattice [292, 293]. It exhibits a novel electronic state with protected surface states, making it a topological insulator. $Eu_2Ir_2O_7$ compound is an example of a material where the pyrochlore lattice leads to frustrated magnetic interactions, resulting in exotic magnetic states and potential applications in spintronics [294]. $Pr_2Ir_2O_7$ compound is a heavy fermion material with a pyrochlore lattice [295]. It exhibits unconventional electronic behavior and is of interest in the study of strongly correlated electron systems.

The above examples of real systems show that these systems have a diverse range of physical phenomena that can emerge in materials with pyrochlore lattice structures. Researchers investigate these materials to understand fundamental aspects of quantum magnetism, topological phases, and other condensed matter physics phenomena. The unique geometric frustration in the pyrochlore lattice often leads to unconventional and intriguing properties, making these materials fascinating subjects of study in the field of condensed matter physics.

Significant attention has been devoted to the examination of spin-1/2 systems with antiferromagnetic couplings on the pyrochlore lattice. Classical investigations have elucidated a noteworthy phenomenon, revealing that the arms of each tetrahedron contribute to geometrical frustration. This frustration proves to be a pivotal factor in disrupting the anticipated magnetic ordering within the system, ultimately leading it into a disordered magnetic phase [296].

Despite the prevailing disorder, the authentic ground state of the classical system has been identified as a spin-ice state. This distinctive state adheres to the 2-in

and 2-out rule [297], showcasing a remarkable manifestation of magnetic behavior. In contrast, the exploration of three-dimensional pyrochlore lattices featuring isotropic Heisenberg exchange interactions introduces a formidable modeling challenge. This system's intricate nature has sparked prolonged and unresolved debates surrounding its elusive ground state, adding a layer of complexity and interest to the overall understanding of such spin systems on pyrochlore lattices.

In this chapter, we study the quantum phase transitions of a Heisenberg antiferromagnetic spin-1/2 on pyrochlore ladder geometry with periodic boundary conditions along the width, and a cartoon of the structure is shown in Fig. 7.1. The main goal of this work is to find the true ground state of a 2-layer ladder-like spin-1/2 pyrochlore structure by tunning the exchange parameters J_l, J_r, J_u and J_d which are the leg, rung, vertical up and down antiferromagnetic exchange interactions shown in Fig. xx.

7.2 Many-body Hamiltonian for the Pyrochlore ladder

The ladder-like pyrochlore structure with a system size of 32 is shown in the schematic. 7.1, and this system can be thought of as three different layers. In the top and bottom layers, it forms a kagome ladder, whereas, the middle layer forms a square ladder. The lattice indices on the top layer are $1, 3, 5, 9, 11, 13..$ and $2, 4, 6, 10, 12, 14..$ as shown in Fig.7.1. The lattice indices for the square ladder are $7, 8, 15, 16, ..$ etc. However, collectively all of these lattice points are arranged in such a way that the smallest unit of this kind of ladder forms a tetrahedron. Further, someone can notice carefully and find that all of these tetrahedrons are connected to four other tetrahedrons at their four vertices. The entire pyrochlore ladder consists of 16 pyrochlore units, however, this system size can be nevertheless infinitely large, and due to the short-range nature of the ground state, we believe that the ground state phase of this system survives even the thermodynamic limit.

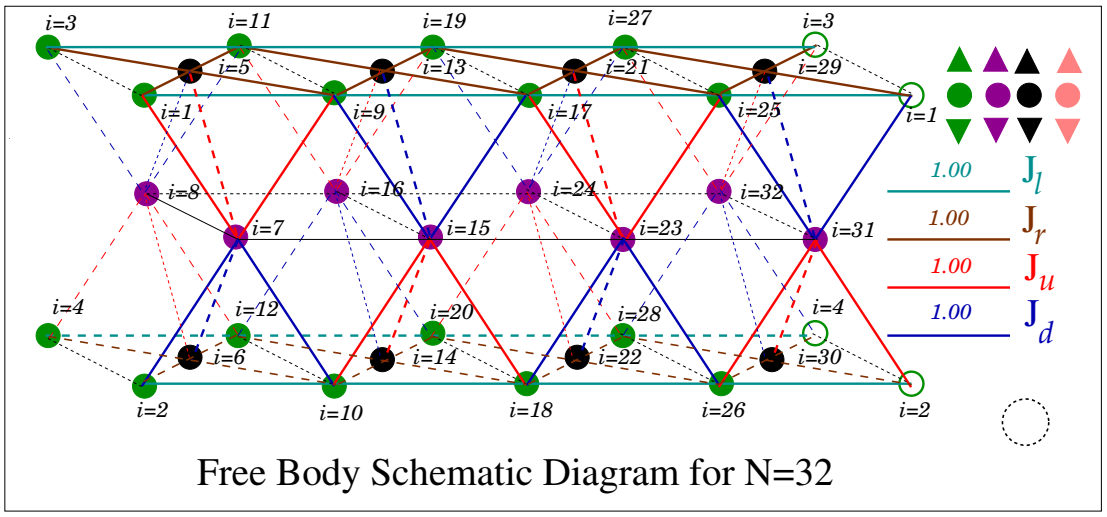

FIGURE 7.1: (color online) Schematic of a 3-layer pyrochlore ladder. The leg J_l, rung J_r, vertically up J_u, and vertically down J_d exchange interaction are shown in cyan, brown, red, and blue colors respectively. Black red, and indigo colors represent each site. All the spins at the legs of the top and bottom layers are shown in green color. The spins situated at the middle of the top and bottom layers are shown in black color. All the spins in the middle layer are shown in indigo colors. These spins are disconnected in the same layer and connected to the top and bottom layers via J_u and J_d.

The model Hamiltonian of each of the tetrahedrons can be written as follows

$$H_i = \sum_{k,i\neq j} J_x S_i S_j \tag{7.1}$$

Where J_k is the exchange interaction between two sites i and j. There are two kinds of exchanges in the top and bottom layers. The exchange interactions of the kagome ladder along the rung or zig-zag direction (shown in brown color) is J_r, whereas along the leg J_l. There is no exchange interaction among the spins in the middle layer but these spins are connected to the top and bottom layers through exchange interactions J_u or J_d. The alternative spins in the middle layer are connected through J_u,J_d to the top layer and J_d,J_u to the bottom layer. The Hamiltonian of this model is solved using the iterative variational method (IVM) which is discussed in Chapter 2.

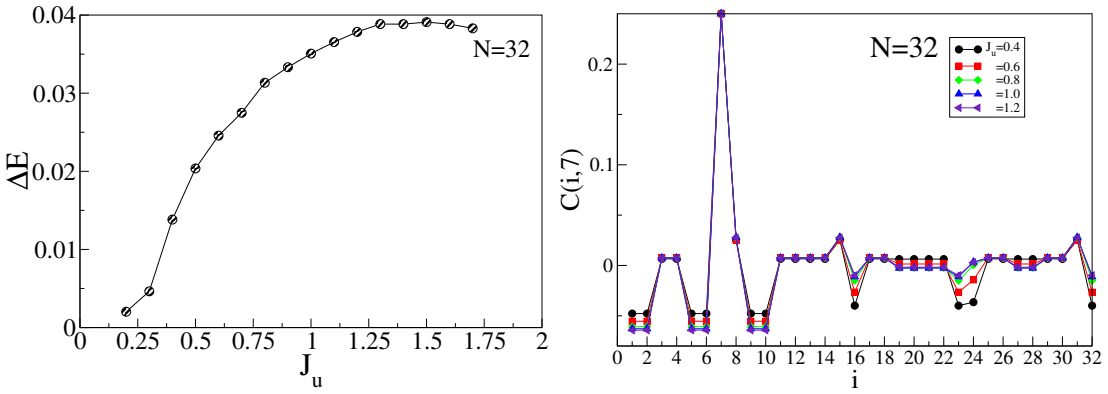

FIGURE 7.2: (color online) (a) Energy gap (ΔE) shown as a function J_u for the system size $N = 32$. (b) Spin-spin correlation at site i concerning $i = 7$ is shown as a function of the site index i. The black, red, green, blue, and violet colors represent the exchange parameter values $J_r = 0.4, 0.6, 0.8, 1.0, 1.2$ respectively.

7.3 Results

Throughout our calculation, we assume that $J_l = 1$ and $J_u = J_d$, and all the results are presented as a function of J_r and J_u. By varying two of these parameters we characterize various quantum phases based upon the low-lying energy gap and spin-spin correlation. The low-lying energy gap can be defined as the following

$$\Delta E = E_1(S^z = 0) - E_0(S^z = 0) \tag{7.2}$$

Here, $E_n(S^z = 0)$ is the n^{th} level energy eigenvalue for the z-component of spin sector $S^z = 0$. We focus only on the two lowest-lying states to study the energy crossover as a function of tuning parameters. $n = 0, 1$ represents the ground state, and the first excited state respectively. The z-component of the spin-spin correlation $C(i, k)$ between any two spins i and k can be calculated for the ground-state wavefunction as following

$$C(i, k) = \langle S_i^z S_k^z \rangle \tag{7.3}$$

The $\langle\rangle$ represents the expectation value of $S_i^z S_k^z$ of a state.

7.3.1 Energy gap and spin-spin correlation by tunning J_u

We first study the energy crossover in the system by tuning J_u and keeping J_r fixed to unity. In Fig.7.2, the excitation gap ΔE is shown. ΔE increases with increasing J_u in the scale of 10^{-2} which is very tiny for $N = 32$ and it will vanish in the thermodynamic limit. The vanishingly small ΔE in the finite system indicates at least a doubly degenerate ground state in the system which can be understood intuitively from the following discussion. The top and bottom layers of the pyrochlore ladder in Fig.7.1 are individual kagome layers. With the leg and rung exchange interactions being equal to $J_l = J_r = 1$, each of the decoupled kagome layers has a doubly degenerate ground state. There are exponentially increasing singlet excitations below the first triplet for a kagome lattice and this is why the pyrochlore ladder also has many low-lying singlet excitations. The lowest excitation gap for the pyrochlore ladder is found to be very tiny as shown in Fig.7.2. (a). As a consequence, the correlation function in the system is highly localized as described below.

The spin-spin correlation function $C(i, 7)$ for any site i from a reference site 7 is shown in Fig.7.2. The reference site 7 is situated in the middle layer of the system which is connected through exchange J_u. It is noticed that the $C(i, 7)$ shows a short-range correlation which is restricted to the vertices of tetrahedrons $i = 1, 2, 5, 6, 9, 10$ connected to the site 7. The small value of J_u is in the critical limit where the wavefunctions are degenerate and so at further distances such as $i = 16, 23, 24, 32$, the correlation is found to be small but finite. With the increase in J_u, it is noticed that the correlation at the vertices $i = 1, 2, 5, 6, 9, 10$ increases and decreases at $i = 16, 23, 24, 32$. The exponential decay in correlation and increasing energy gap support the existence of a non-degenerate ground state.

7.3.2 Energy gap and spin-spin correlation by tuning J_r

We now turn our focus to analyzing the effect of J_r by keeping J_u. The energy gap and spin-spin correlation are calculated for various J_r by setting J_u to unity.

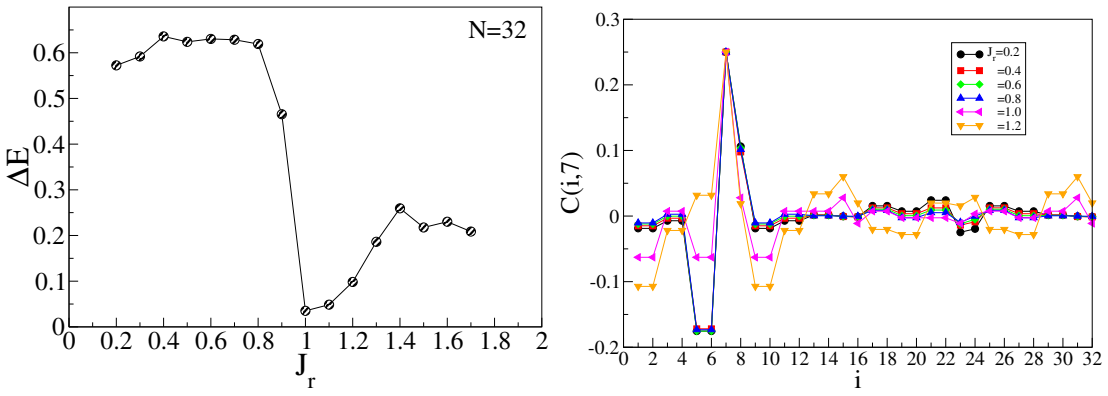

FIGURE 7.3: (color online) (a) Energy gap (ΔE) shown as a function J_r for the system size $N = 32$. (b) Spin-spin correlation at site i concerning $i = 7$ is shown as a function of the site index i. The black, red, green, blue, magenta and yellow colors represent the exchange parameter values $J_r = 0.2, 0.4, 0.6, 0.8, 1.0, 1.2$ respectively.

Fig.7.3 shows the energy gap ΔE as a function of the exchange parameter J_r. With increasing J_r, the finite gap ΔE is almost a constant around 0.6 and then it suddenly jumps at $J_r = 1$ to almost zero, and on further increase in J_r opens up the gap again above $J_r = 1$. The finite non-vanishing ΔE at every value of J_r except $J_r = 1$ represents the ground states to be always nondegenerate. The vanishingly small value of the gap on the other hand indicates a spontaneous symmetry-broken phase transition. The non-vanishing gap is unusual from the previous case as described in .7.3.1 because of the unequal exchange interactions in the top and bottom layers. The finite exchange J_u connects both of top and bottom layers which as a result gives the non-degenerate ground state for any value of the rung exchange except $J_r = 1$. J_r is the special case that mimics the previous scenario and it results in having the ground state of the top and bottom layers degenerate. Even having sufficient exchange interaction strength of J_u because each of the top and bottom layers isolated gives rise to a degenerate ground state, the spectrum of the entire system also has a vanishingly small gap.

In Fig.7.3, the spin-spin correlation $C(i, 7)$ of the system is shown as a function of the site indices i from the reference site at $i = 7$. $C(i, 7)$ is shown for various J_r values in the spacing of 0.2. It is noticed that the $C(i, 7)$ falls off rapidly as distance from the reference site 7, and it implies the short-range correlation nature of the ground state in the system. The large finite values of correlation $C(i, 7)$

at $i = 1, 2, 5, 6, 9, 10$ are noticed for the vertices of the tetrahedrons connected to reference site $i = 7$. It is also noticed that for $J_r \langle 1$, the reference site $i = 7$ is strongly connected antiferromagnetically to the sites $i = 5, 6$ at the top and bottom layers respectively. Above $J_r = 1$, the site 7 is strongly aligned opposite to the other vertices $i = 1, 2, 9, 10$ of the tetrahedrons as compared to $i = 5, 6$. These two scenarios are for two competing limits of J_r and J_u. However, in these two competing limits, all of the spins at the vertices of the mentioned tetrahedrons change sign concerning the reference site $i = 7$. The change in sign of the spin-spin correlation is consistent with the energy gap as discussed above and both of these two results are signatures of a symmetry-broken phase transition.

7.4 Summary

We study a three-layer ladder-like pyrochlore lattice structure of system size $N = 32$ using IVM. The energy gap between the ground state and the first excited states ΔE and spin-spin correlation for the ground state wavefunction is studied by tuning two of the exchange parameters J_u and J_r separately while the other is kept fixed to unity. We notice that the system has a tiny gap which is a consequence of the degenerate states of each kagome ladder a the top and bottom layers, and a further increase in J_u does not enhance the gap or show any kind of energy crossover, therefore, we do not expect any sharp change in ground state phase. By tuning the exchange parameter J_r, it is noticed that the system shows a finite and large gap below and above $J_r = 1$ which in turn implies the existence of the non-degenerate ground state phases. We notice a quantum critical point at $J_r = 1$ about which the energy gap and the correlation function seem to be non-trivial. The finite size effect in this system is quite dominant and so the finite size scaling is needed to confirm all the conclusions.

Chapter 8

Conclusion

In this chapter, we summarize all the thesis works.

In Chapter 3, the spin-1/2 chain with nearest neighbor antiferromagnetic J_1 and next nearest neighbor antiferromagnetic J_2 model is extensively studied earlier as well which shows various quantum phase transitions. The characterization of the quantum phase transitions is done earlier by calculating the singlet-triplet gap and the nature of the quantum phases is well understood by the spin-spin correlation function. In this thesis, we propose an iterative variational method (IVM) to produce the most probable spin configurations (MPSC) for the same model. The use of these MPSCs for the ground state (GS) and first excited state (FES) as an input to Principal component analysis (PCA) successfully characterizes the phase boundaries and identifies the nature of the quantum phases in terms of principal components. The principal components for the GS wavefunction identify the Majumder-Ghosh point $\frac{J_2}{J_1} = 0.5$. The gapless quasi-long-range ordered (QLRO) spin liquid-gapped dimer phase boundary is characterized using the principal components of the FES.

In Chapter 4, the first principal component characterizes the first-order quantum phase transition from the ferromagnetic to XY phase for the spin-1/2 XXZ model at $\frac{\Delta}{J} = -1$. The finite-size scaling of the second principal component successfully detects the infinite order Kosterlitz-Thouless (KT) phase transition point at $\frac{\Delta}{J} = 1$.

In Chapter 5, a spin-1/2 two-leg ladder with alternate Ising J_c Heisenberg J_q rung, Ising type leg interaction J_{cq} and Ising type diagonal interaction J_d is considered. The quantum phase transition is studied in the parameter plane of $J_q - J_d$ by keeping other exchange parameters to unity. Under the periodic boundary condition, the ground state energy, and singlet-triplet energy gap calculation characterize four quantum GS phases: stripe rung ferromagnet (SRFM), Dimer, anisotropic antiferromagnet (AAFM), stripe leg ferromagnet (SLFM). The spin-spin correlation studies give the spin ordering in these GS phases. The jumps in the von Neumann entropy, concurrence are consistent with the characterized phase boundaries. Further, the effect of thermal fluctuation is studied in brief for finite temperature calculation by using the transfer matrix method.

In Chapter 6, the effect of the magnetic field on the quantum phases of the same two-leg ladder with alternate Ising-Heisenberg rung interactions is studied. The magnetization process is studied with the same set of exchange parameters in the presence of the longitudinal and transverse magnetic fields separately. In the presence of the longitudinal magnetic field, the quantum phases exhibit four types of magnetic plateau phases: 0 plateau, 1/2 saturation type-1 plateau, 1/2 saturation type-2 plateau, and full saturation plateau. For five sets of the longitudinal field, the phase boundaries are characterized by defining a quantum phase index.

In Chapter 7, a ladder system of the pyrochlore lattice of system size $N = 32$ is considered to study the quantum phase transitions. The energy crossover and spin-spin correlation characterize the quantum phase boundary between two ordered phases for the system size $N = 32$ when all the exchange bonds are equal. Because of the high frustration and finite size effect, the ground state phases are yet inconclusive for the thermodynamic limit.

Bibliography

[1] S. S. Rahaman, S. Sahoo, and M. Kumar, Journal of Physics: Condensed Matter **33**, 265801 (2021).

[2] M. T. Vlaardingerbroek and J. A. Boer, *Magnetic resonance imaging: theory and practice* (Springer Science & Business Media, 2013).

[3] Y. Zhang and J.-F. Lin, Science **375**, 146 (2022).

[4] B. Gozick, K. P. Subbu, R. Dantu, and T. Maeshiro, IEEE Transactions on Instrumentation and Measurement **60**, 3883 (2011).

[5] V. Kasavajhala, Proc. Dell Tech. White Paper , 8 (2011).

[6] P. Mohn, *Magnetism in the solid state: an introduction*, Vol. 134 (Springer Science & Business Media, 2002).

[7] P. Fazekas, *Lecture notes on electron correlation and magnetism*, Vol. 5 (World scientific, 1999).

[8] N. Menyuk, t. K. Dwight, t. R. Arnott, and A. Wold, Journal of Applied Physics **37**, 1387 (1966).

[9] B. Matthias, R. Bozorth, and J. Van Vleck, Physical Review Letters **7**, 160 (1961).

[10] H. Bohn, W. Zinn, B. Dorner, and A. Kollmar, Physical Review B **22**, 5447 (1980).

[11] I. Yamada, Journal of the Physical Society of Japan **28**, 1585 (1970).

[12] E. Janke, M. Hutchings, P. Day, and P. Walker, Journal of Physics C: Solid State Physics **16**, 5959 (1983).

[13] M. Lines and E. Jones, Physical Review **139**, A1313 (1965).

[14] D. T. Teaney, M. J. Freiser, and R. Stevenson, Physical Review Letters **9**, 212 (1962).

[15] M. Hagiwara, K. Katsumata, and J. Tuchendler, Journal of Physics: Condensed Matter **6**, 545 (1994).

[16] T. Komaru, T. Hihara, and Y. Koi, Journal of the Physical Society of Japan **31**, 1391 (1971).

[17] L. Pauling, Journal of the American Chemical Society **53**, 1367 (1931).

[18] M. Born, Ann. Phys **84**, 457 (1927).

[19] Y. Mo and S. D. Peyerimhoff, The Journal of chemical physics **109**, 1687 (1998).

[20] R. Micnas, J. Ranninger, and S. Robaszkiewicz, Reviews of Modern Physics **62**, 113 (1990).

[21] E. Dagotto, Reviews of Modern Physics **66**, 763 (1994).

[22] N. Mott, Pure and Applied Chemistry VI **52**, 65 (1980).

[23] N. Mott, *Metal-insulator transitions* (CRC Press, 2004).

[24] J. Kanamori, Progress of Theoretical Physics **30**, 275 (1963).

[25] M. C. Gutzwiller, Physical Review Letters **10**, 159 (1963).

[26] J. Hubbard, Proceedings of the Royal Society of London. Series A. Mathematical and Physical Sciences **277**, 237 (1964).

[27] T. S. Venkatakrishnan, S. Sahoo, N. Bréfuel, C. Duhayon, C. Paulsen, A.-L. Barra, S. Ramasesha, and J.-P. Sutter, Journal of the American Chemical Society **132**, 6047 (2010).

[28] T. Moriya, Physical review **120**, 91 (1960).

[29] M. E. Fisher, American Journal of Physics **32**, 343 (1964).

[30] H. Bethe, Zeitschrift für Physik **71**, 205 (1931).

[31] A. W. Sandvik, in *AIP Conference Proceedings*, Vol. 1297 (American Institute of Physics, 2010) pp. 135–338.

[32] S. Sachdev, Physics world **12**, 33 (1999).

[33] I. Affleck and F. Haldane, Physical Review B **36**, 5291 (1987).

[34] J. C. Bonner and M. E. Fisher, Physical Review **135**, A640 (1964).

[35] R. Orbach, Physical Review **112**, 309 (1958).

[36] L. Walker, Physical Review **116**, 1089 (1959).

[37] J. Des Cloizeaux and M. Gaudin, Journal of Mathematical Physics **7**, 1384 (1966).

[38] A. Y. Kitaev, Physics-uspekhi **44**, 131 (2001).

[39] C. K. Majumdar and D. K. Ghosh, Journal of Mathematical Physics **10**, 1388 (1969).

[40] J. Sirker, Z. Weihong, O. Sushkov, and J. Oitmaa, Physical Review B **73**, 184420 (2006).

[41] R. Chitra, S. Pati, H. Krishnamurthy, D. Sen, and S. Ramasesha, Physical Review B **52**, 6581 (1995).

[42] S. R. White and I. Affleck, Physical Review B **54**, 9862 (1996).

[43] E. Sørensen, I. Affleck, D. Augier, and D. Poilblanc, Physical Review B **58**, R14701 (1998).

[44] S. Wessel, B. Normand, F. Mila, and A. Honecker, SciPost Physics **3**, 005 (2017).

[45] T. Ogino, R. Kaneko, S. Morita, S. Furukawa, and N. Kawashima, Physical Review B **103**, 085117 (2021).

[46] T. Ogino, R. Kaneko, S. Morita, and S. Furukawa, Physical Review B **106**, 155106 (2022).

[47] D. Maiti and M. Kumar, Journal of Magnetism and Magnetic Materials **486**, 165266 (2019).

[48] K. Morita, T. Sugimoto, S. Sota, and T. Tohyama, Physical Review B **97**, 014412 (2018).

[49] S. Acevedo, C. A. Lamas, M. Arlego, and P. Pujol, Physical Review B **100**, 195145 (2019).

[50] S. Das, D. Dey, S. Ramasesha, and M. Kumar, The European Physical Journal B **95**, 147 (2022).

[51] D. Dey, S. Das, M. Kumar, and S. Ramasesha, Physical Review B **101**, 195110 (2020).

[52] E. S. Sørensen and H.-Y. Kee, npj Quantum Materials **9**, 10 (2024).

[53] E. Dagotto and T. M. Rice, Science **271**, 618 (1996), https://science.sciencemag.org/content/271/5249/618.full.pdf .

[54] D. C. Johnston, Phys. Rev. B **54**, 13009 (1996).

[55] T. Barnes, E. Dagotto, J. Riera, and E. S. Swanson, Phys. Rev. B **47**, 3196 (1993).

[56] I. Heilmann, G. Shirane, Y. Endoh, R. Birgeneau, and S. Holt, Physical Review B **18**, 3530 (1978).

[57] I. Umegaki, H. Tanaka, N. Kurita, T. Ono, M. Laver, C. Niedermayer, C. Rüegg, S. Ohira-Kawamura, K. Nakajima, and K. Kakurai, Physical Review B **92**, 174412 (2015).

[58] M. Hutchings, J. Milne, and H. Ikeda, Journal of Physics C: Solid State Physics **12**, L739 (1979).

[59] S. Dutton, M. Kumar, M. Mourigal, Z. G. Soos, J.-J. Wen, C. L. Broholm, N. H. Andersen, Q. Huang, M. Zbiri, R. Toft-Petersen, *et al.*, Physical review letters **108**, 187206 (2012).

[60] M. Mourigal, M. Enderle, B. Fåk, R. Kremer, J. Law, A. Schneidewind, A. Hiess, and A. Prokofiev, Physical review letters **109**, 027203 (2012).

[61] S. Park, Y. Choi, C. Zhang, and S.-W. Cheong, Physical review letters **98**, 057601 (2007).

[62] S.-L. Drechsler, O. Volkova, A. Vasiliev, N. Tristan, J. Richter, M. Schmitt, H. Rosner, J. Málek, R. Klingeler, A. Zvyagin, *et al.*, Physical review letters **98**, 077202 (2007).

[63] A. W. Sandvik, E. Dagotto, and D. J. Scalapino, Physical Review B **53**, R2934 (1996).

[64] E. Dagotto and T. Rice, Science **271**, 618 (1996).

[65] D. Johnston, Physical Review B **54**, 13009 (1996).

[66] T. Barnes, E. Dagotto, J. Riera, and E. Swanson, Physical Review B **47**, 3196 (1993).

[67] S. Dutton, M. Kumar, Z. Soos, C. Broholm, and R. Cava, Journal of Physics: Condensed Matter **24**, 166001 (2012).

[68] M. Kumar, S. Dutton, R. Cava, and Z. Soos, Journal of Physics: Condensed Matter **25**, 136004 (2013).

[69] R. Coldea, D. Tennant, R. Cowley, D. McMorrow, B. Dorner, and Z. Tylczynski, Physical review letters **79**, 151 (1997).

[70] W. Shiramura, K.-i. Takatsu, H. Tanaka, K. Kamishima, M. Takahashi, H. Mitamura, and T. Goto, Journal of the Physical Society of Japan **66**, 1900 (1997).

[71] W. Shiramura, K.-i. Takatsu, B. Kurniawan, H. Tanaka, H. Uekusa, Y. Ohashi, K. Takizawa, H. Mitamura, and T. Goto, Journal of the Physical Society of Japan **67**, 1548 (1998).

[72] E. Manousakis, Reviews of Modern Physics **63**, 1 (1991).

[73] Y. Kitaoka, T. Kobayashi, A. Kōda, H. Wakabayashi, Y. Niino, H. Yamakage, S. Taguchi, K. Amaya, K. Yamaura, M. Takano, *et al.*, journal of the physical society of japan **67**, 3703 (1998).

[74] R. Coldea, D. Tennant, K. Habicht, P. Smeibidl, C. Wolters, and Z. Tylczynski, Physical review letters **88**, 137203 (2002).

[75] Y. Shimizu, K. Miyagawa, K. Kanoda, M. Maesato, and G. Saito, Physical review letters **91**, 107001 (2003).

[76] Y. Singh and P. Gegenwart, Physical Review B **82**, 064412 (2010).

[77] Y. Singh, S. Manni, J. Reuther, T. Berlijn, R. Thomale, W. Ku, S. Trebst, and P. Gegenwart, Physical review letters **108**, 127203 (2012).

[78] M. Korotin, I. Elfimov, V. Anisimov, M. Troyer, and D. Khomskii, Physical review letters **83**, 1387 (1999).

[79] N. D. Mermin and H. Wagner, Physical Review Letters **17**, 1133 (1966).

[80] L. Balents, Nature **464**, 199 (2010).

[81] L. Néel, in *Annales de physique*, Vol. 12 (1948) pp. 137–198.

[82] L. D. Landau, Phys. Z. Sowjet **4**, 675 (1933).

[83] M. Kumar, A. Parvej, and Z. G. Soos, Journal of Physics: Condensed Matter **27**, 316001 (2015).

[84] S. White, R. Noack, and D. Scalapino, Physical review letters **73**, 886 (1994).

[85] J. Luttinger, Journal of mathematical physics **4**, 1154 (1963).

[86] D. C. Mattis and E. H. Lieb, Condensed Matter Physics and Exactly Soluble Models: Selecta of Elliott H. Lieb , 645 (2004).

[87] P. W. Anderson, Materials Research Bulletin **8**, 153 (1973).

[88] L. Savary and L. Balents, Reports on Progress in Physics **80**, 016502 (2016).

[89] A. Honecker, F. Mila, and M. Troyer, The European Physical Journal B-Condensed Matter and Complex Systems **15**, 227 (2000).

[90] P. Jordan and E. P. Wigner, *Über das paulische äquivalenzverbot* (Springer, 1993).

[91] E. Lieb, T. Schultz, and D. Mattis, Annals of Physics **16**, 407 (1961).

[92] B. M. McCoy, Physical Review **173**, 531 (1968).

[93] Y. Li, H. Liao, Z. Zhang, S. Li, F. Jin, L. Ling, L. Zhang, Y. Zou, L. Pi, Z. Yang, *et al.*, Scientific reports **5**, 16419 (2015).

[94] H. Bu, M. Ashtar, T. Shiroka, H. C. Walker, Z. Fu, J. Zhao, J. S. Gardner, G. Chen, Z. Tian, and H. Guo, Physical Review B **106**, 134428 (2022).

[95] S. R. White, R. M. Noack, and D. J. Scalapino, Phys. Rev. Lett. **73**, 886 (1994).

[96] M. Kumar, A. Parvej, and Z. G. Soos, Journal of Physics: Condensed Matter **27**, 316001 (2015).

[97] S. Morita, R. Kaneko, and M. Imada, Journal of the Physical Society of Japan **84**, 024720 (2015).

[98] T. Verkholyak and J. Strečka, Journal of Physics A: Mathematical and Theoretical **45**, 305001 (2012).

[99] K. Okamoto and K. Nomura, Physics Letters A **169**, 433 (1992).

[100] J. Kosterlitz, Journal of physics. Condensed matter: an Institute of Physics journal **28**, 481001 (2016).

[101] J. M. Kosterlitz and D. J. Thouless, Journal of Physics C: Solid State Physics **6**, 1181 (1973).

[102] M. V. Rakov, M. Weyrauch, and B. Braiorr-Orrs, Physical Review B **93**, 054417 (2016).

[103] H.-J. Mikeska and A. K. Kolezhuk, Quantum magnetism , 1 (2004).

[104] K. Hijii, A. Kitazawa, and K. Nomura, Physical Review B **72**, 014449 (2005).

[105] M. A. Nielsen and I. L. Chuang, *Quantum computation and quantum information* (Cambridge university press, 2010).

[106] M. A. Nielsen, arXiv preprint quant-ph/9606012 (1996).

[107] L. Vidmar and M. Rigol, Physical review letters **119**, 220603 (2017).

[108] R. Jozsa and J. Schlienz, Physical Review A **62**, 012301 (2000).

[109] S.-J. Gu, H.-Q. Lin, and Y.-Q. Li, Physical Review A **68**, 042330 (2003).

[110] M. Oshikawa, M. Yamanaka, and I. Affleck, Phys. Rev. Lett. **78**, 1984 (1997).

[111] J. Carrasquilla and R. G. Melko, Nature Physics **13**, 431 (2017).

[112] N. C. Costa, W. Hu, Z. Bai, R. T. Scalettar, and R. R. Singh, Physical Review B **96**, 195138 (2017).

[113] W. Hu, R. R. Singh, and R. T. Scalettar, Physical Review E **95**, 062122 (2017).

[114] L. Wang, Physical Review B **94**, 195105 (2016).

[115] C. M. Bender and T. T. Wu, Physical Review D **7**, 1620 (1973).

[116] P. M. Chaikin, T. C. Lubensky, and T. A. Witten, *Principles of condensed matter physics*, Vol. 10 (Cambridge university press Cambridge, 1995).

[117] A. Auerbach, *Interacting electrons and quantum magnetism* (Springer Science & Business Media, 2012).

[118] K. G. Wilson, Reviews of modern physics **47**, 773 (1975).

[119] K. G. Wilson, Reviews of Modern Physics **55**, 583 (1983).

[120] D. Sénéchal, in *Theoretical Methods for Strongly Correlated Electrons* (Springer, 2004) pp. 139–186.

[121] S. Rettrup, Journal of Computational Physics **45**, 100 (1982).

[122] C. Lanczos, (1950).

[123] E. R. Davidson, Journal of Computational Physics **17**, 87 (1975).

[124] S. R. White, Physical review letters **69**, 2863 (1992).

[125] S. R. White, Physical review b **48**, 10345 (1993).

[126] M. Suzuki, *Quantum Monte Carlo methods in condensed matter physics* (World scientific, 1993).

[127] S. R. White and D. A. Huse, Physical Review B **48**, 3844 (1993).

[128] J. Biamonte and V. Bergholm, arXiv preprint arXiv:1708.00006 (2017).

[129] U. Schollwöck, Annals of physics **326**, 96 (2011).

[130] C. Lanczos, J. Res. Nat. Bur. Standards **49**, 33 (1952).

[131] R. Riedinger and M. Benard, The Journal of chemical physics **94**, 1222 (1991).

[132] C. Davidson, Journal of Computational Physics **17**, 87 (1975).

[133] E. R. Davidson and W. J. Thompson, Computers in Physics **7**, 519 (1993).

[134] A. Parvej, .

[135] S. Sachdev, *Quantum phase transitions* (Cambridge university press, 2011).

[136] S. Sachdev, Nature Physics **4**, 173 (2008).

[137] G. D. Mahan, *Many-Particle Physics*, 3rd ed. (Springer US, 2000).

[138] A. L. Fetter and J. D. Walecka, *Quantum theory of many-particle systems* (Courier Corporation, 2012).

[139] Q. Si and F. Steglich, Science **329**, 1161 (2010).

[140] L. Carr, *Understanding quantum phase transitions* (CRC press, 2010).

[141] J. Ren, W.-L. You, and A. M. Oleś, Phys. Rev. B **102**, 024425 (2020).

[142] C. K. Majumdar and D. K. Ghosh, Journal of Mathematical Physics **10**, 1388 (1969), https://doi.org/10.1063/1.1664978 .

[143] D. J. Thouless, *The quantum mechanics of many-body systems* (Courier Corporation, 2014).

[144] S. E. Dutton, M. Kumar, M. Mourigal, Z. G. Soos, J.-J. Wen, C. L. Broholm, N. H. Andersen, Q. Huang, M. Zbiri, R. Toft-Petersen, and R. J. Cava, Phys. Rev. Lett. **108**, 187206 (2012).

[145] M. E. Zhitomirsky and H. Tsunetsugu, EPL (Europhysics Letters) **92**, 37001 (2010).

[146] A. V. Chubukov, Phys. Rev. B **44**, 4693 (1991).

[147] S. Furukawa, M. Sato, S. Onoda, and A. Furusaki, Phys. Rev. B **86**, 094417 (2012).

[148] A. Parvej and M. Kumar, Phys. Rev. B **96**, 054413 (2017).

[149] S. K. Saha, M. S. Roy, M. Kumar, and Z. G. Soos, Phys. Rev. B **101**, 054411 (2020).

[150] D. Maiti and M. Kumar, Phys. Rev. B **100**, 245118 (2019).

[151] F. D. M. Haldane, Phys. Rev. Lett. **45**, 1358 (1980).

[152] M. Takahashi, Prog. Theoretical Physics **42**, 1098 (1969).

[153] H. Shiba, Phys. Rev. B **6**, 930 (1972).

[154] I. Affleck and J. B. Marston, Phys. Rev. B **37**, 3774 (1988).

[155] J. B. Marston and I. Affleck, Phys. Rev. B **39**, 11538 (1989).

[156] T. Giamarchi, *Quantum physics in one dimension*, Vol. 121 (Clarendon press, 2003).

[157] R. Shankar, Rev. Mod. Phys. **66**, 129 (1994).

[158] Z. G. Soos and S. Ramasesha, Phys. Rev. B **29**, 5410 (1984).

[159] Z. G. Soos and S. Ramasesha, Phys. Rev. Lett. **51**, 2374 (1983).

[160] S. R. White, Phys. Rev. Lett. **69**, 2863 (1992).

[161] S. R. White, Phys. Rev. B **48**, 10345 (1993).

[162] U. Schollwöck, Rev. Mod. Phys. **77**, 259 (2005).

[163] K. A. Hallberg, Adv. Phys. **55**, 477 (2006).

[164] A. W. Sandvik, AIP Conf. Proc. **1297**, 135 (2010).

[165] A. W. Sandvik and J. Kurkijärvi, Phys. Rev. B **43**, 5950 (1991).

[166] P. Henelius and A. W. Sandvik, Phys. Rev. B **62**, 1102 (2000).

[167] J. Carrasquilla and R. Melko, Nature Physics **13** (2017), 10.1038/nphys4035.

[168] G. Torlai and R. G. Melko, Phys. Rev. B **94**, 165134 (2016).

[169] M. J. S. Beach, A. Golubeva, and R. G. Melko, Phys. Rev. B **97**, 045207 (2018).

[170] P. Broecker, J. Carrasquilla, R. G. Melko, and S. Trebst, Scientific reports **7**, 1 (2017).

[171] J. Shlens, "A tutorial on principal component analysis," (2014), arXiv:arXiv.1404.1100 [cs.LG] .

[172] J. F. Rodriguez-Nieva and M. S. Scheurer, Nature Physics **15**, 790 (2019).

[173] B. S. Rem, N. Käming, M. Tarnowski, L. Asteria, N. Fläschner, C. Becker, K. Sengstock, and C. Weitenberg, Nature Physics **15**, 917 (2019).

[174] N. C. Costa, W. Hu, Z. J. Bai, R. T. Scalettar, and R. R. P. Singh, Phys. Rev. B **96**, 195138 (2017).

[175] E. Rosten and T. Drummond, in *Computer Vision – ECCV 2006*, edited by A. Leonardis, H. Bischof, and A. Pinz (Springer Berlin Heidelberg, Berlin, Heidelberg, 2006) pp. 430–443.

[176] B. Zoph, V. Vasudevan, J. Shlens, and Q. V. Le, "Learning transferable architectures for scalable image recognition," (2018).

[177] C. M. Bishop, "Pattern recognition," (2006).

[178] D. Liben-Nowell and J. Kleinberg, J. American. Society. Info. Sci. Tech. **58**, 1019–1031 (2007).

[179] M. R. Islam, M. A. Kabir, A. Ahmed, A. R. M. Kamal, H. Wang, and A. Ulhaq, Health info. science and systems **6**, 1 (2018).

[180] P. Galán-García, J. G. d. l. Puerta, C. L. Gómez, I. Santos, and P. G. Bringas, Logic J. IGPL **24**, 42 (2015).

[181] J.-A. Choi and K. Lim, ICT Express **6**, 175 (2020).

[182] I. Bose and R. K. Mahapatra, Information & Management **39**, 211 (2001).

[183] A. Rajkomar, J. Dean, and I. Kohane, New England J. Medicine **380**, 1347 (2019).

[184] V. M. Eskov, V. F. Pyatin, V. Eskov, and L. Ilyashenko, Biophysics **64**, 293 (2019).

[185] M. Q. Ding, L. Chen, G. F. Cooper, J. D. Young, and X. Lu, Molecular Cancer Research **16**, 269 (2018).

[186] K. Albertsson, P. Altoe, D. Anderson, M. Andrews, and et. al., J. Phys.: Conf. Series **1085**, 022008 (2018).

[187] P. Baldi, P. Sadowski, and D. Whiteson, Nature communications **5**, 1 (2014).

[188] P. Huembeli, A. Dauphin, and P. Wittek, Physical Review B **97**, 134109 (2018).

[189] A. Tirelli and N. C. Costa, Physical Review B **104**, 235146 (2021).

[190] Y. Yang, Z.-Z. Sun, S.-J. Ran, and G. Su, Physical Review B **103**, 075106 (2021).

[191] Y. Guo, Y. Liu, A. Oerlemans, S. Lao, S. Wu, and M. S. Lew, Neurocomputing **187**, 27 (2016).

[192] Y. LeCun, Y. Bengio, and G. Hinton, Nature **521**, 436 (2015).

[193] E. Greplova, A. Valenti, G. Boschung, F. Schäfer, N. Lörch, and S. D. Huber, New Journal of Physics **22**, 045003 (2020).

[194] I. T. Jolliffe, Principal component analysis , 167 (2002).

[195] I. T. Jolliffe and J. Cadima, Phil. Trans. Royal Society A: Math, Phys. and Eng. Sciences **374**, 20150202 (2016).

[196] R. M. Woloshyn, (2019), arXiv:1905.08220 [cond-mat.stat-mech] .

[197] W. Hu, R. R. P. Singh, and R. T. Scalettar, Phys. Rev. E **95**, 062122 (2017).

[198] L. Wang, Phys. Rev. B **94**, 195105 (2016).

[199] C. Wang and H. Zhai, Phys. Rev. B **96**, 144432 (2017).

[200] Y. Che, C. Gneiting, T. Liu, and F. Nori, Phys. Rev. B **102**, 134213 (2020).

[201] E. P. Van Nieuwenburg, Y.-H. Liu, and S. D. Huber, Nature Physics **13**, 435 (2017).

[202] K. Ch'ng, N. Vazquez, and E. Khatami, Physical Review E **97**, 013306 (2018).

[203] Z. G. Soos, A. Parvej, and M. Kumar, Journal of Physics: Condensed Matter **28**, 175603 (2016).

[204] J. Sirker, V. Y. Krivnov, D. V. Dmitriev, A. Herzog, O. Janson, S. Nishimoto, S.-L. Drechsler, and J. Richter, Phys. Rev. B **84**, 144403 (2011).

[205] M. Kumar, S. Ramasesha, and Z. G. Soos, Croatica Chemica Acta **86**, 407 (2013).

[206] S. R. White and I. Affleck, Phys. Rev. B **54**, 9862 (1996).

[207] R. Chitra, S. Pati, H. R. Krishnamurthy, D. Sen, and S. Ramasesha, Phys. Rev. B **52**, 6581 (1995).

[208] M. Kumar, S. Ramasesha, and Z. G. Soos, Phys. Rev. B **81**, 054413 (2010).

[209] M. V. Rakov, M. Weyrauch, and B. Braiorr-Orrs, Phys. Rev. B **93**, 054417 (2016).

[210] H. E. Stanley, Physical Review Letters **20**, 589 (1968).

[211] L. Lima, Solid State Communications **309**, 113836 (2020).

[212] L. Justino and T. R. de Oliveira, Physical Review A **85**, 052128 (2012).

[213] J. Kosterlitz and D. Thouless, Rev. B **19**, 1855 (1979).

[214] J. Hutchinson, J. Keating, F. Mezzadri, *et al.*, Advances in Mathematical Physics **2015** (2015).

[215] D. Dmitriev and V. Y. Krivnov, Physical Review B **70**, 144414 (2004).

[216] S. S. Rahaman, S. Haldar, and M. Kumar, Journal of Physics: Condensed Matter (2023).

[217] A. W. Sandvik, E. Dagotto, and D. J. Scalapino, Phys. Rev. B **53**, R2934 (1996).

[218] N. Maeshima, M. Hagiwara, Y. Narumi, K. Kindo, T. C. Kobayashi, and K. Okunishi, Journal of Physics: Condensed Matter **15**, 3607 (2003).

[219] D. C. Johnston, J. W. Johnson, D. P. Goshorn, and A. J. Jacobson, Phys. Rev. B **35**, 219 (1987).

[220] M. J. M. Hutchings M T, Ikeda H, Journal of Physics C, Solid State Physics **18**, L739 (1979).

[221] S. Park, Y. J. Choi, C. L. Zhang, and S.-W. Cheong, Phys. Rev. Lett. **98**, 057601 (2007).

[222] M. Mourigal, M. Enderle, B. Fåk, R. K. Kremer, J. M. Law, A. Schneidewind, A. Hiess, and A. Prokofiev, Phys. Rev. Lett. **109**, 027203 (2012).

[223] S.-L. Drechsler, O. Volkova, A. N. Vasiliev, N. Tristan, J. Richter, M. Schmitt, H. Rosner, J. Málek, R. Klingeler, A. A. Zvyagin, and B. Büchner, Phys. Rev. Lett. **98**, 077202 (2007).

[224] S. E. Dutton, M. Kumar, Z. G. Soos, C. L. Broholm, and R. J. Cava, Journal of Physics: Condensed Matter **24**, 166001 (2012).

[225] B. S. Shastry and B. Sutherland, Phys. Rev. Lett. **47**, 964 (1981).

[226] F. D. M. Haldane, Phys. Rev. B **25**, 4925 (1982).

[227] I. U. Heilmann, G. Shirane, Y. Endoh, R. J. Birgeneau, and S. L. Holt, Phys. Rev. B **18**, 3530 (1978).

[228] I. Umegaki, H. Tanaka, N. Kurita, T. Ono, M. Laver, C. Niedermayer, C. Rüegg, S. Ohira-Kawamura, K. Nakajima, and K. Kakurai, Phys. Rev. B **92**, 174412 (2015).

[229] E. Manousakis, Rev. Mod. Phys. **63**, 1 (1991).

[230] Y. Singh and P. Gegenwart, Phys. Rev. B **82**, 064412 (2010).

[231] M. Mourigal, M. Enderle, R. K. Kremer, J. M. Law, and B. Fåk, Phys. Rev. B **83**, 100409 (2011).

[232] M. Enderle, B. Fåk, H.-J. Mikeska, R. K. Kremer, A. Prokofiev, and W. Assmus, Phys. Rev. Lett. **104**, 237207 (2010).

[233] Z. Seidov, T. P. Gavrilova, R. M. Eremina, L. E. Svistov, A. A. Bush, A. Loidl, and H.-A. Krug von Nidda, Phys. Rev. B **95**, 224411 (2017).

[234] C. R. Kumar M, Dutton SE and S. ZG, J Phys Condens Matter **25**, 136004 (2013).

[235] J. Sirker, Phys. Rev. B **81**, 014419 (2010).

[236] T. Hamada, J.-i. Kane, S.-i. Nakagawa, and Y. Natsume, Journal of the Physical Society of Japan **57**, 1891 (1988), https://doi.org/10.1143/JPSJ.57.1891 .

[237] P. Anderson, Materials Research Bulletin **8**, 153 (1973).

[238] P. Fazekas and P. W. Anderson, The Philosophical Magazine: A Journal of Theoretical Experimental and Applied Physics **30**, 423 (1974), https://doi.org/10.1080/14786439808206568 .

[239] S. Eggert, Phys. Rev. B **54**, R9612 (1996).

[240] T. Tonegawa and I. Harada, Journal of the Physical Society of Japan **56**, 2153 (1987), https://doi.org/10.1143/JPSJ.56.2153 .

[241] M. A. Korotin, I. S. Elfimov, V. I. Anisimov, M. Troyer, and D. I. Khomskii, Phys. Rev. Lett. **83**, 1387 (1999).

[242] M. A. Korotin, V. I. Anisimov, T. Saha-Dasgupta, and I. Dasgupta, Journal of Physics: Condensed Matter **12**, 113 (1999).

[243] L. Savary and L. Balents, Reports on Progress in Physics **80**, 016502 (2016).

[244] D. Maiti and M. Kumar, Phys. Rev. B **100**, 245118 (2019).

[245] J. Curély, R. Georges, and M. Drillon, Phys. Rev. B **33**, 6243 (1986).

[246] J. Strecka and M. Jascur, Journal of Physics: Condensed Matter **15**, 4519 (2003).

[247] H. Rezania, Journal of Magnetism and Magnetic Materials **388**, 68 (2015).

[248] E. Čižmár, M. Ozerov, J. Wosnitza, B. Thielemann, K. W. Krämer, C. Rüegg, O. Piovesana, M. Klanjšek, M. Horvatić, C. Berthier, and S. A. Zvyagin, Phys. Rev. B **82**, 054431 (2010).

[249] B. Thielemann, C. Rüegg, H. M. Rønnow, A. M. Läuchli, J.-S. Caux, B. Normand, D. Biner, K. W. Krämer, H.-U. Güdel, J. Stahn, K. Habicht, K. Kiefer, M. Boehm, D. F. McMorrow, and J. Mesot, Phys. Rev. Lett. **102**, 107204 (2009).

[250] O. Rojas, J. Strečka, and S. M. de Souza, Solid State Communications **246**, 68 (2016), arXiv:1607.00889 [cond-mat.stat-mech] .

[251] Brzezicki, W. and Ole´s, A. M., Eur. Phys. J. B **66**, 361 (2008).

[252] Verkholyak and Strecka, Condensed Matter Physics **16**, 13601 (2013).

[253] K. Karl'ová, J. Strečka, and M. L. Lyra, Phys. Rev. E **100**, 042127 (2019).

[254] J. Strečka, O. Rojas, T. Verkholyak, and M. L. Lyra, Phys. Rev. E **89**, 022143 (2014).

[255] R. S. Sahoo Shaon, Sutter Jean-Pascal, Journal of Statistical Physics **147**, 181 (2012).

[256] K. Huang, *Statistical Mechanics*, Vol. 978 (Wiley, 2008).

[257] P. Rungta, V. Bužek, C. M. Caves, M. Hillery, and G. J. Milburn, Phys. Rev. A **64**, 042315 (2001).

[258] T. Nakamura and K. Okamoto, Physical Review B **58**, 2411 (1998).

[259] S. Guo, R. Zhong, K. Górnicka, T. Klimczuk, and R. J. Cava, Chemistry of Materials **32**, 10670 (2020).

[260] D. C. Kakarla, Z. Yang, H. Wu, T. Kuo, A. Tiwari, W.-H. Li, C. Lee, Y.-Y. Wang, J.-Y. Lin, C. Chang, *et al.*, Materials Advances **2**, 7939 (2021).

[261] A. V. Chubukov, S. Sachdev, and J. Ye, Physical Review B **49**, 11919 (1994).

[262] T. Vekua, G. Japaridze, and H.-J. Mikeska, Physical Review B **67**, 064419 (2003).

[263] J. Richter, J. Schulenberg, and A. Honecher, "Quantum magnetism in two dimensions: From semi-classical néel order to magnetic disorder in quantum magnetism, ed. u. schollwöck, j. richter, djj farnell and rf bishop," (2004).

[264] T. Sakai, R. Nakanishi, T. Yamada, R. Furuchi, H. Nakano, H. Kaneyasu, K. Okamoto, and T. Tonegawa, Physical Review B **106**, 064433 (2022).

[265] H.-J. Liao, Z.-Y. Xie, J. Chen, Z.-Y. Liu, H.-D. Xie, R.-Z. Huang, B. Normand, and T. Xiang, Physical review letters **118**, 137202 (2017).

[266] D. Johnston, R. McQueeney, B. Lake, A. Honecker, M. Zhitomirsky, R. Nath, Y. Furukawa, V. Antropov, and Y. Singh, Physical Review B **84**, 094445 (2011).

[267] W.-Y. Liu, S.-S. Gong, Y.-B. Li, D. Poilblanc, W.-Q. Chen, and Z.-C. Gu, Science bulletin **67**, 1034 (2022).

[268] S.-H. Li, Q.-Q. Shi, M. T. Batchelor, and H.-Q. Zhou, New Journal of Physics **19**, 113027 (2017).

[269] C. E. Agrapidis, J. van den Brink, and S. Nishimoto, Phys. Rev. B **99**, 224418 (2019).

[270] N. Ivanov, arXiv preprint arXiv:0909.2182 (2009).

[271] T. Sakai and S. Yamamoto, Physical Review B **60**, 4053 (1999).

[272] T. Sakai and N. Okazaki, Journal of Applied Physics **87**, 5893 (2000).

[273] M. S. Naseri and S. Mahdavifar, Physica A: Statistical Mechanics and its Applications **474**, 107 (2017).

[274] H. A. Zad and N. Ananikian, Journal of Physics: Condensed Matter **30**, 165403 (2018).

[275] G. I. Japaridze and E. Pogosyan, Journal of Physics: Condensed Matter **18**, 9297 (2006).

[276] H. Moradmard, M. Shahri Naseri, and S. Mahdavifar, Journal of Superconductivity and Novel Magnetism **27**, 1265 (2014).

[277] J. Strecka and M. Jascur, Journal of Physics: Condensed Matter **15**, 4519 (2003).

[278] K. Karl'ová, J. Strečka, and M. L. Lyra, Physical Review E **100**, 042127 (2019).

[279] J. Strečka, O. Rojas, T. Verkholyak, and M. L. Lyra, Physical Review E **89**, 022143 (2014).

[280] W. K. Wootters, Phys. Rev. Lett. **80**, 2245 (1998).

[281] K. Karľová and J. Strecka, Acta Physica Polonica A **137**, 595 (2020).

[282] H. T. Quan and F. M. Cucchietti, Phys. Rev. E **79**, 031101 (2009).

[283] D. ER, Journal of Computational Physics **17**, 87 (1975).

[284] M. Suzuki, Physical Review B **31**, 2957 (1985).

[285] K. Matsuhira, M. Wakeshima, R. Nakanishi, T. Yamada, A. Nakamura, W. Kawano, S. Takagi, and Y. Hinatsu, Journal of the Physical Society of Japan **76**, 043706 (2007).

[286] K. Matsuhira, M. Wakeshima, Y. Hinatsu, and S. Takagi, Journal of the Physical Society of Japan **80**, 094701 (2011).

[287] J. E. Greedan, Journal of Alloys and Compounds **408**, 444 (2006).

[288] T. Sakakibara, T. Tayama, Z. Hiroi, K. Matsuhira, and S. Takagi, Physical review letters **90**, 207205 (2003).

[289] A. B. Eyvazov, R. Dusad, T. J. Munsie, H. A. Dabkowska, G. M. Luke, E. R. Kassner, J. S. Davis, and A. Eyal, Physical Review B **98**, 214430 (2018).

[290] K. Ross, T. Proffen, H. Dabkowska, J. Quilliam, L. Yaraskavitch, J. Kycia, and B. Gaulin, Physical Review B **86**, 174424 (2012).

[291] H. Yan, O. Benton, L. Jaubert, and N. Shannon, Physical Review B **95**, 094422 (2017).

[292] D. Mandrus, J. Thompson, R. Gaal, L. Forro, J. Bryan, B. Chakoumakos, L. Woods, B. Sales, R. Fishman, and V. Keppens, Physical Review B **63**, 195104 (2001).

[293] D. J. Singh, P. Blaha, K. Schwarz, and J. O. Sofo, Physical Review B **65**, 155109 (2002).

[294] K. MISHRA, *Investigation of Physical Properties of Pyrochlore Iridates*, Ph.D. thesis (2015).

[295] S. Nakatsuji, Y. Machida, Y. Maeno, T. Tayama, T. Sakakibara, J. Van Duijn, L. Balicas, J. Millican, R. Macaluso, and J. Y. Chan, Physical review letters **96**, 087204 (2006).

[296] L. Minervini, R. W. Grimes, and K. E. Sickafus, Journal of the American Ceramic Society **83**, 1873 (2000).

[297] J. D. Bernal and R. H. Fowler, The Journal of Chemical Physics **1**, 515 (1933).